JYU DISSERTATIONS 688

Tero Harjupatana

Monitoring Water Transport and Deformation in Swelling Materials Using X-Ray Imaging and Tomography

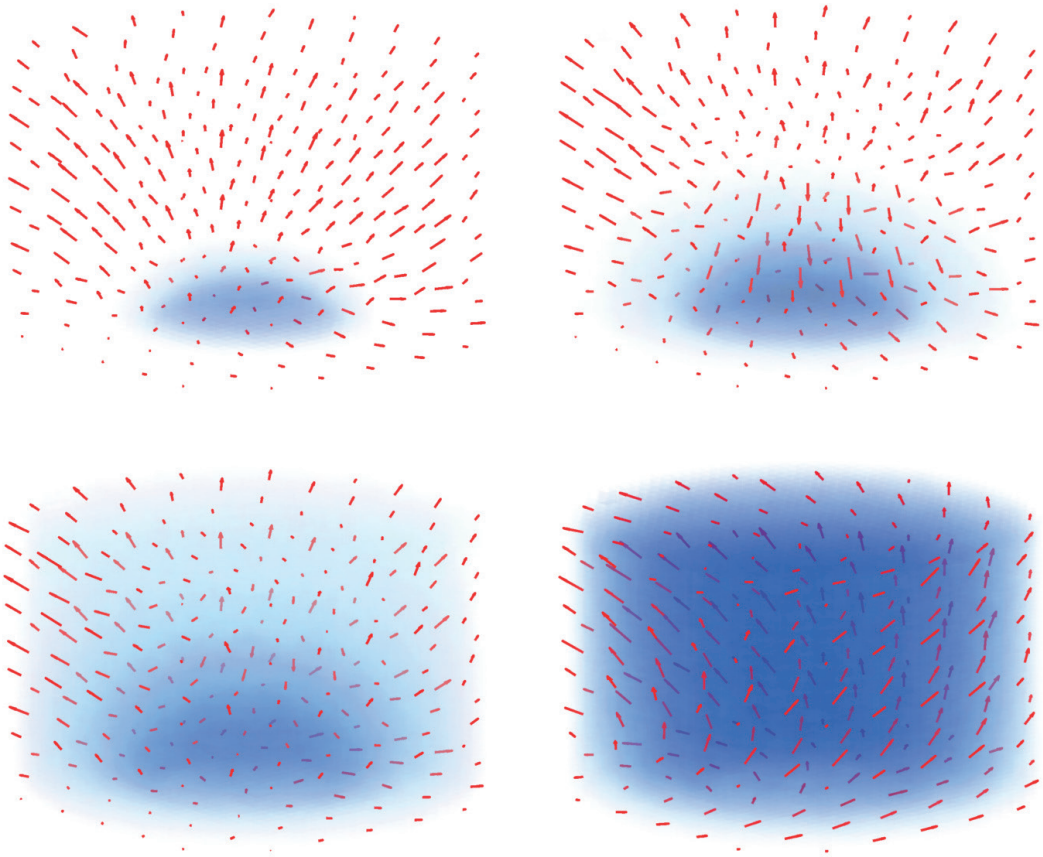

UNIVERSITY OF JYVÄSKYLÄ
FACULTY OF MATHEMATICS
AND SCIENCE

JYU DISSERTATIONS 688

Tero Harjupatana

Monitoring Water Transport and Deformation in Swelling Materials Using X-Ray Imaging and Tomography

Esitetään Jyväskylän yliopiston matemaattis-luonnontieteellisen tiedekunnan suostumuksella
julkisesti tarkastettavaksi yliopiston Ylistönrinteen salissa FYS1
syyskuun 8. päivänä 2023 kello 12.

Academic dissertation to be publicly discussed, by permission of
the Faculty of Mathematics and Science of the University of Jyväskylä,
in Ylistönrinne, auditorium FYS1, on September 8, 2023 at 12 o'clock noon.

JYVÄSKYLÄN YLIOPISTO
UNIVERSITY OF JYVÄSKYLÄ

JYVÄSKYLÄ 2023

Editors
Ilari Maasilta
Department of Physics, University of Jyväskylä
Ville Korkiakangas
Open Science Centre, University of Jyväskylä

Cover image by Tero Harjupatana.

ISBN 978-951-39-9718-2 (PDF)
URN:ISBN:978-951-39-9718-2
ISSN 2489-9003

Permanent link to this publication: http://urn.fi/URN:ISBN:978-951-39-9718-2

ABSTRACT

Water transport in porous materials is an important phenomenon in many practical applications. Modeling of water transport is often used to evaluate the performance of such applications in real conditions. The modeling can be, however, very challenging since many materials have a complex structure and water can be transported by several different mechanisms in different parts of the material. Many materials also deform and change their structure due to changes in water content. Model development thus requires detailed experimental data on water content distribution and possibly also on deformation in the material at different points in time. However, there are not many methods available for producing such data, especially for swelling materials.

In this thesis, a non-destructive method based on 3D (2D + time) X-ray imaging or 4D (3D + time) X-ray tomography to monitor water transport and deformation in swelling materials is introduced. The method comprises taking of multiple images of a sample at suitable intervals during a wetting or drying process. After correcting for several types of image artifacts, the images are used to calculate the attenuation coefficient distribution and to measure the deformation of the sample at different times. These results together with careful calibration are used to calculate the final results, the partial density distributions of solid and water in the sample as a function of time. The accuracy of the method is limited by remaining image artifacts and errors in deformation measurement.

The method was successfully applied to bentonite and biocomposite samples. Bentonite is a swelling clay material, which is used in many nuclear waste disposal concepts as a buffer material between waste canisters and the bedrock. Mechanical behavior of bentonite and water transport mechanisms in bentonite are still not fully understood, and hence detailed experimental data can help to develop better models for more reliable safety assessments of disposal concepts. Biocomposite consists of natural fibers as reinforcement in a polymer matrix, which can also be made from renewable resources. Properties of natural fibers and biocomposites may, however, degrade when exposed to water, and hence studying water transport can help to develop more durable materials.

Keywords: Bentonite, biocomposite, X-ray imaging, X-ray tomography, water transport, deformation, image correlation

TIIVISTELMÄ (FINNISH ABSTRACT)

Veden kulkeutuminen huokoisissa materiaaleissa on tärkeä ilmiö monissa käytännön sovelluksissa. Veden kulkeutumisen mallintamista käytetään usein arvioimaan sovelluksien toimivuutta oikeissa toimintaympäristöissä. Mallintaminen voi kuitenkin olla hyvin haastavaa, sillä monet materiaalit ovat monimutkaisia rakenteeltaan ja vesi voi kulkeutua useiden eri mekanismien avulla materiaalin eri osissa. Monet materiaalit myös muuttavat muotoaan ja rakennetta vesipitoisuuden muuttuessa. Mallien kehittämistä varten tarvitaan siten yksityiskohtaista kokeellista tietoa materiaalin vesipitoisuusjakaumasta ja mahdollisesti myös muodonmuutoksesta eri ajanhetkinä. Tällaisen tiedon tuottamiseen, erityisesti paisuville materiaaleille, ei kuitenkaan ole juuri menetelmiä olemassa.

Tässä tutkielmassa esitellään 3D (2D + aika) röntgenkuvaukseen tai 4D (3D + aika) röntgentomografiaan perustuva näytettä rikkomaton menetelmä, jolla veden kulkeutumista voidaan seurata paisuvissa materiaaleissa. Menetelmässä näytteestä otetaan useita kuvia sopivin väliajoin kastumisen tai kuivumisen aikana. Useiden erityyppisten kuvavirheiden korjausten jälkeen kuvista lasketaan näytteen vaimennuskerroinjakauma ja mitataan näytteen muodonmuutos eri ajanhetkinä. Näiden tulosten ja huolellisen kalibroinnin avulla voidaan laskea lopullisina tuloksina kiintoaineen ja veden osatiheysjakaumat ajan funktiona. Menetelmän tarkkuutta rajoittavat jäljelle jääneet kuvavirheet ja virheet muodonmuutoksen mittauksessa.

Menetelmää sovellettiin onnistuneesti bentoniitti- ja biokomposiittinäytteisiin. Bentoniitti on paisuvaa savimateriaalia, jota käytetään ydinjätteen loppusijoituksessa ydinjätekanisterien ja kallioperän välisenä puskurimateriaalina monissa loppusijoituskonsepteissa. Bentoniitin mekaanista käyttäytymistä ja veden kulkeutumista bentoniitissa ei kuitenkaan täysin tunneta, ja siksi yksityiskohtainen kokeellinen tieto voi auttaa kehittämään parempia malleja loppusijoituskonseptien luotettavampia turvallisuusarvioita varten. Biokomposiitissa on vahvikkeena luonnonkuituja polymeerimatriisissa, joka voi myös olla valmistettu uusiutuvista luonnonvaroista. Luonnonkuitujen ja biokomposiittien ominaisuudet voivat kuitenkin heiketä veden vaikutuksesta, ja siksi veden kulkeutumisen tutkiminen voi auttaa kehittämään kestävämpiä materiaaleja.

Keywords: Bentoniitti, biokomposiitti, röntgenkuvaus, röntgentomografia, veden kulkeutuminen, muodonmuutos, kuvakorrelaatio

Author

Tero Harjupatana
Department of Physics
University of Jyväskylä
Finland

Supervisors

Dr. Arttu Miettinen
Department of Physics
University of Jyväskylä
Finland

Prof. Emeritus Markku Kataja
Department of Physics
University of Jyväskylä
Finland

Reviewers

Dr. Klaus-Peter Kröhn
Gesellschaft für Anlagen- und Reaktorsicherheit (GRS) gGmbH
Germany

Dr. Pierre Bésuelle
Laboratoire 3SR
Université Grenoble Alpes, CNRS, Grenoble INP
France

Opponent

Prof. Peter Moonen
DMEX Centre for X-ray Imaging
Université de Pau et des Pays de l'Adour (UPPA)
France

ACKNOWLEDGMENTS

The research included in this thesis was funded by the Finnish Research Programme on Nuclear Waste Management through bentonite research projects BOA (2011–2014) and THEBES (2015–2018), and by the European commission through bentonite research project BELBaR (2012–2016).

I would like to thank my supervisor Prof. Markku Kataja for giving me the opportunity to work in the tomo group and for guiding my research through many years. I would also like to thank Dr. Arttu Miettinen, who has helped me in many situations and has also been my supervisor in the recent years. Many thanks go to MSc Jarno Alaraudanjoki and MSc Joni Parkkonen for technical guidance. Long-time collaboration with VTT's nuclear waste management people, especially Prof. Markus Olin and Dr. Veli-Matti Pulkkanen, has been very valuable.

I thank the Faculty of Mathematics and Science and the Department of Physics of the University of Jyväskylä, where the staff has always been very kind and helpful. Special thanks go to the mechanical workshop of the department, where many parts of the test equipment were made.

I also thank all the friends and colleagues who have helped and supported me in many ways through my long journey. Finally, I would like to thank my family members for patience and support.

Jyväskylä, August 2023

Tero Harjupatana

LIST OF INCLUDED PUBLICATIONS

P1 Harjupatana T., Alaraudanjoki J., and Kataja M.. X-ray tomographic method for measuring three-dimensional deformation and water content distribution in swelling clays. *Applied Clay Science*, 114:386–394, 2015.

P2 Miettinen A, Harjupatana T, Kataja M., Fortino S., and Immonen K.. Time-resolved X-ray microtomographic measurement of water transport in wood-fibre reinforced composite material. *IOP Conference Series: Materials Science and Engineering*, 139:012037, 2016.

P3 Harjupatana T., Miettinen A., and Kataja M.. A method for measuring wetting and swelling of bentonite using X-ray imaging. *Applied Clay Science*, 221:106485, 2022.

AUTHOR'S CONTRIBUTION

The author developed the methods used in Publications P1–P3. He also carried out the main experimental work and data analysis, and wrote the initial drafts of Publications P1 and P3. The author also helped in experiments, data analysis and writing the initial draft of Publication P2.

CONTENTS

1 INTRODUCTION

As water is the most abundant liquid on Earth, its presence and transport in different materials are of great interest in many fields. Water is an essential substance in living organisms, different tissues contain and transport water in animals, plants and fungi. Deeper understanding of transport processes may help, e.g., to develop better treatments for illnesses in humans and to breed resource-efficient plants for food production [1, 2]. Groundwater movements in soils provide water for humans, animals and plants but may also transport pollutants [3]. Such movements also affect the strength of soil, which is an important consideration in civil engineering [4, 5]. Proper moisture transport through building materials prevents molding, decay and corrosion [6]. In clothes, sufficient moisture transport through textiles guarantees wear comfort and prevents bacterial growth [7, 8]. There are numerous similar examples of practical applications where water transport plays an important role.

Many porous materials have a complex heterogeneous structure, where solid-water interactions can also be complex. Hence, water can be transported by different mechanisms in such materials, e.g., by flow in porous media, diffusion in solid matrix or on its surfaces and vapor diffusion in pore space. As many materials swell when absorbing water and shrink when drying, mechanical behavior and water transport may be strongly coupled. Water transport may also depend on wetting-drying history due to irreversible deformations and other hysteresis effects. To develop and validate water transport models for such complex materials, detailed experimental data on spatial and temporal evolution of water content during wetting or drying process are needed. Simultaneous deformation measurement would also be useful, especially if the transport modeling is coupled with the mechanical modeling.

The average water content of a sample can be measured gravimetrically, by weighing the sample before and after oven drying. By cutting the sample into smaller pieces, a rough estimate of the water content distribution can be obtained. As this

method is destructive, it can be applied to the same sample only at one point in time. The method may also be difficult to apply to small samples. However, there are several non-destructive imaging methods that have been used to measure water content distributions in different materials. The most relevant to mention here are magnetic resonance imaging (MRI) [9–12], neutron imaging and tomography [13,14], and X-ray imaging and tomography [15,16]. All of those produce high-resolution 2D or 3D images of samples, in which water content changes are readily visible. MRI and neutron imaging are very sensitive to water, but unfortunately MRI has challenges to detect water in some soil materials [17] and neutron imaging facilities are sparse, and thus not so readily available for an average user [18]. X-rays are not quite as sensitive to water as magnetic resonance and neutrons are, but on the other hand the sensitivity to many solid materials may be higher. This is important because in order to determine the gravimetric water content (see Equation 2.1), the density distributions of both water and solid material are needed. Moreover, the good availability of X-ray imaging and tomography devices makes X-ray based imaging techniques an attractive option for routine measurements.

There are different approaches to quantify the amount of water in porous samples using X-ray imaging and tomography. Liquid pore water can be directly segmented from the images, provided that the image resolution and the contrasts between the air, water and solid are high enough [19,20]. This method, however, fails if a significant portion of the total water is in small pores below the image resolution. In another approach, a dry state image is subtracted from a wet state image, resulting a difference image where the pixel values are proportional to the volumetric water content values (see Equation 2.2) as the contribution of (inert) solid material cancels out. By using the known average water content or separate calibration measurements, the difference image can easily be calibrated to give the volumetric water content distribution. However, this method as such is not suitable for deformable materials, because then the contribution of solid material does not cancel out and the result will be erroneous. There have been some studies where X-ray tomography is used to measure water transport in wood samples and the deformation is taken into account [21–23]. However, the analyses in those studies are two-dimensional (applied to wood cross-sections and the deformation in the axial direction is neglected) and the mass attenuation coefficients of wood and water are assumed to be the same (they approximately are). These assumptions may be valid for wood and water, but not for many other materials. Hence, there is need for a similar but a more general method to monitor water transport and deformation in various kinds of swelling materials.

In this thesis, a method based on X-ray imaging or tomography for monitoring the water content distribution in swelling materials is introduced. Samples are sequentially imaged during a wetting or drying process. Changes in pixel values are related to the total density changes, which are now considered to be caused by both solid material deformations and water content changes. By measuring the deformation of the solid material, the contributions of solid and water can be

separated. After several image correction methods and careful calibration, needed for quantitative image analysis, the method yields spatial and temporal evolution of the displacement field, the partial density distributions of solid and water and the water content distribution. A modification of the method is also introduced, which allows calculating the partial density distributions without deformation measurement, but only if the sample is fully saturated with water.

The method was applied to bentonite and biocomposite samples. Bentonite is a natural clay material, which swells when absorbing water. As it has many useful properties, it is planned to be used as a buffer material between waste canisters and the bedrock in many nuclear waste disposal concepts. However, bentonite has turned out to be very difficult material to model, and hence data on groundwater transport and induced deformation are needed to properly model its behavior in the nuclear waste repository conditions. Composite materials typically consist of a polymer matrix mixed with fibers as reinforcement, which form, when combined appropriately, a light but strong material. In more environmental friendly biocomposites, the fibers are extracted from natural sources and the polymer matrix may also have been made from renewable resources. However, the strength and lifespan of natural fibers, and thus biocomposite materials, are degraded when the fibers are exposed to water. Hence, data on water transport in biocomposites are needed to understand the transport mechanisms and to develop better materials for variable environmental conditions.

This thesis is structured as follows. The materials are introduced in Chapter 2. As bentonite was the main material for developing and applying the method, it is covered in more detail than biocomposite. In Chapter 3, the basics of X-rays, their generation and interactions with matter, and the principles of X-ray imaging and tomography are given. Also, different kinds of image artifacts and their correction methods are described. In Chapter 4, practical procedures related to image acquisition and two special image correction techniques are introduced. Thereafter, the deformation measurement and the density analysis, which are used to produce the final results, are described. Four different applications, 1) constant volume wetting of bentonite, 2) water transport in composite material, 3) swelling of bentonite in a tube and 4) sedimentation of dilute bentonite suspension, are introduced in Chapter 5 (in chronological order). Finally, conclusions are drawn in Chapter 6.

2 MATERIALS

2.1 Bentonite

Bentonite is a natural clay material consisting predominantly of a smectite group clay mineral [24,25]. Typically, the clay mineral is montmorillonite whose content may vary and the rest is composed of wide variety of accessory minerals (e.g., quartz, feldspar, illite and calcite). Bentonite has been formed from volcanic ash or rock by weathering, diagenesis or hydrothermal alteration [26,27]. Due to different geological and chemical conditions during the formation, the composition of bentonite varies across deposits. In 2022, the total global production of bentonite was 19 million tons, of which around three-fourths was produced in the USA, India, China, Turkey, Greece and Denmark [28].

Bentonite has many peculiar and useful properties. It is very hygroscopic and it swells when absorbing water. Bentonite can expand many times its original volume in unrestricted conditions or generate a high swelling stress in a closed volume. Dry compacted bentonite is relatively hard solid material, but becomes plastic when wetted. If more water is added, it may turn into a gel or a sol. Bentonite has large surface area and high cation exchange capacity. Due to many useful properties, bentonite is used in numerous applications such as desiccant, sealing material, drilling mud component, clumping cat litter, anti-caking and clarifying agent in food industry [29].

Nuclear waste management

One important application of bentonite is found in the field of nuclear waste management. Spent nuclear fuel from nuclear power plants is considered to be high-level nuclear waste due to a mixture of highly radioactive fission products [30,31]. The radioactivity of spent fuel is initially high but decreases exponentially (Table 2.1). However, due to long-lived radionuclides (actinides), it takes hundreds

TABLE 2.1 Approximate activity of spent nuclear fuel against time. The activity of spent fuel (A_{fuel}) is here compared to the activity of uranium ore needed to product the fuel (A_{ore}) [31].

Time [yr]	$A_{\text{fuel}}/A_{\text{ore}}$
0	1000000
50	3000
1000	50
250000	1

of thousands of years for the radioactivity to fall back to that of uranium ore. Such long timescales require a permanent solution for disposal where the waste is safely isolated from the biosphere and many environmental conditions and risk scenarios (e.g., glacial periods, climate change, geological activity) are taken into account.

Many countries rely on deep geological disposal, where spent fuel is buried deep under the surface of earth into geological formations [32]. For example in Finland, high-level nuclear waste will be deposited at a depth of around 450 m in the bedrock using a multibarrier concept (Figure 2.1) [33]. The barriers are the solid fuel itself, a canister made of iron and copper, a bentonite buffer and the bedrock. The bentonite buffer between the canister and the bedrock has an important role. It prevents direct groundwater flow to the canisters. It also dampens possible rock movements and may even reseal the canisters due to its swelling ability. In the case of canister failure, the buffer impedes radionuclide transport into groundwater. However, bentonite has turned out to be very difficult material to model. Water transport mechanisms and mechanical behavior are not fully understood despite decades of research. Hence, detailed experimental data would help in developing and validating proper transport and material models, which could be then used for safety assessments of disposal concepts.

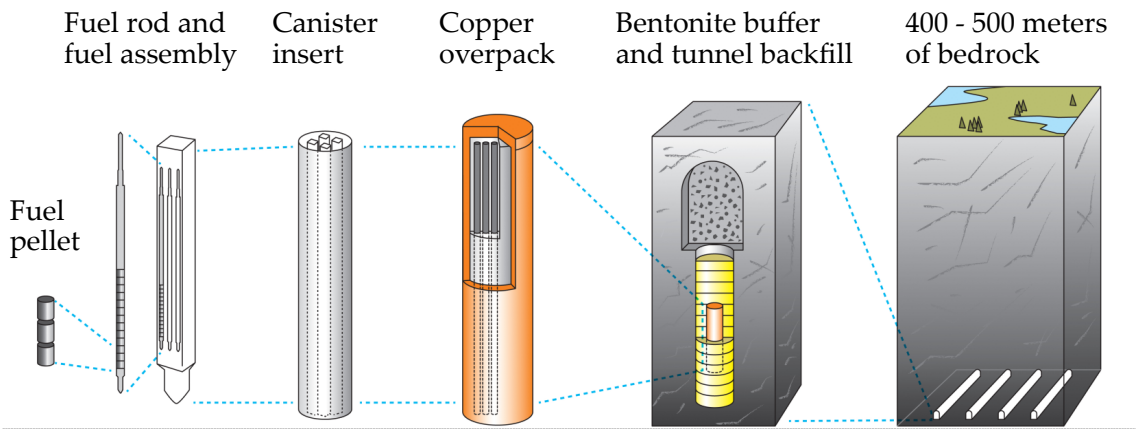

FIGURE 2.1 Nuclear waste disposal concept in Olkiluoto, Finland. Adapted from image by Posiva [34].

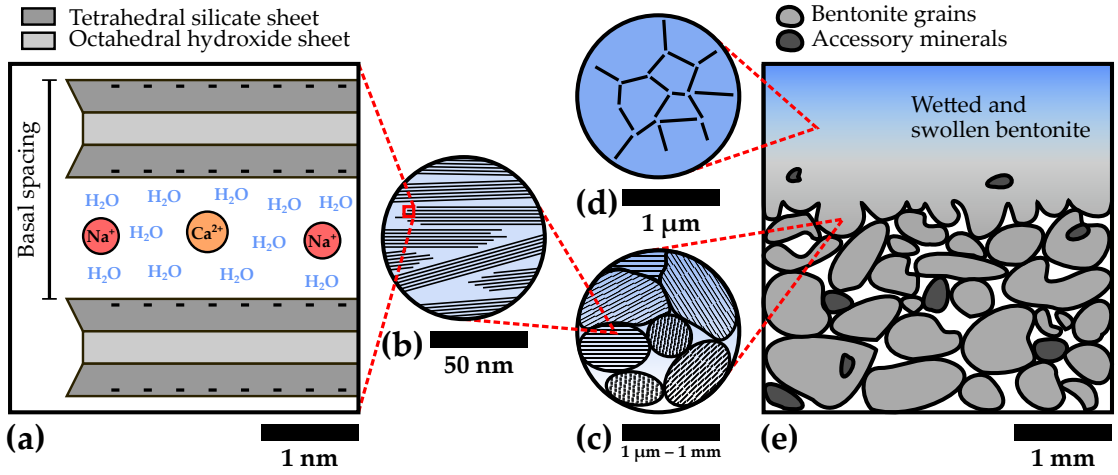

FIGURE 2.2 Structure of bentonite in different scales. The interlayer space between montmorillonite layers contain water and cations (a). Several layers form stacks (b), which in turn form aggregates (c). Loosely bounded layers or stacks form bentonite gel in dilute solutions (d). Dry bentonite may initially be granular but quickly becomes more homogeneous when absorbing water (e).

Structure and swelling

Montmorillonite and other clay minerals [35,36] are phyllosilicates and consist of sheet-like molecules called layers (or platelets). A montmorillonite layer is about 1 nm thick and its effective diameter ranges from 50 to 500 nm [37,38]. It consists of two tetrahedral silicate sheets and an octahedral hydroxide sheet, which together have a negative charge (Figure 2.2a). This charge is compensated by interlayer cations, usually Na^+ and Ca^{2+}, sometimes, e.g., K^+ and Mg^{2+}. Water molecules can enter the interlayer space and hydrate the cations. This leads to crystalline swelling, where the basal spacing can increase from 1 to 2 nm. Interlayer cations are not fixed, those can be exchanged with other types of cations present in water (cation exchange capacity). This may lead to different swelling behavior since the electric charge, ionic radius and hydration ability of different cations vary.

Typically, a few to tens of layers are stacked together and form stacks (or tactoids) (Figure 2.2b) [39]. Na-montmorillonite (Na^+ cations dominate) stacks can disintegrate into single layers at low salinity due to osmotic swelling (beyond a basal spacing of 2 nm), whereas the swelling of Ca-montmorillonite (Ca^{2+} cations dominate) is mostly limited to the crystalline swelling. Stacks in turn form larger structures, aggregates, about which little information (e.g., orientation of stacks in aggregates, sizes and shapes of aggregates) seems to be available. Their existence is, however, justified by mercury intrusion porosimetry (MIP) studies [40, 41], where bimodal pore size distributions are obtained for bentonite. The peaks at around 20 nm and approximately in the range 1–50 µm are believed to be related to the pores between stacks (Figure 2.2b) and the pores between the aggregates

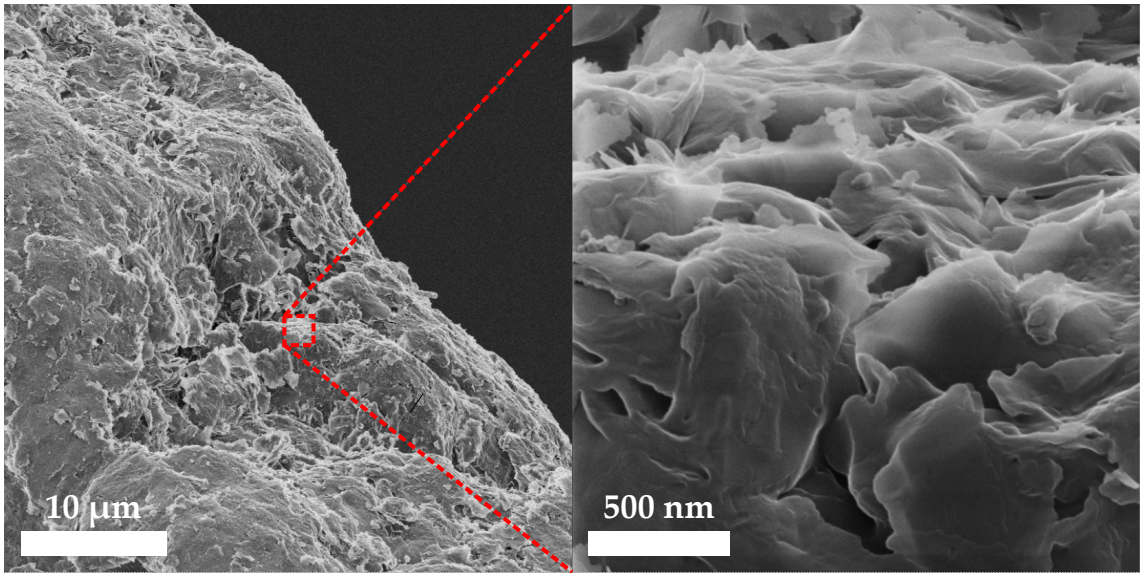

FIGURE 2.3 Helium ion microscope (HIM) images of MX-80 bentonite grain. The images were taken during HIM training with the great help of Kai Arstila.

(Figure 2.2c), respectively (interlayer pores are too small for MIP).

If the water content is high and the solid content low, layers may form loosely bound networks and bentonite turns into a gel (Figure 2.2d) [42]. If the solid content decreases further, clay particles may not be bound with each other anymore and bentonite becomes a sol. A stable sol is possible only for Na-montmorillonite.

Bentonite is often supplied in a granular form where the grain size distribution depends on grinding and sieving processes (Figure 2.2e). Initially granular bentonite becomes quite homogeneous when wetted. This process is not reversible, the swollen grains do not return to their original shape when bentonite is dried, instead of that drying cracks may occur. Hence, the structure also depends on wetting-drying history, at least at this scale.

To get a more realistic view of the microstructure of bentonite in micrometer scale, Figure 2.3 shows helium ion microscope images of the surface of a bentonite grain. The structure looks rather dense, irregular and layered, although individual layers are not readily visible.

Water in bentonite

Water can exist in more or less bound forms in different scale structures in bentonite [43]. Interlayer water between layers contains only cations and is bound to a certain degree. Diffuse double layer water around stacks contains mostly cations but also anions and is less bound than the interlayer water. Pore water in larger pores is charge neutral and is least bound. A small amount of water can also exist as vapor in pores under unsaturated conditions.

The (gravimetric) water content is defined as

$$w = \frac{m_w}{m_d} = \frac{\rho_w}{\rho_d}, \tag{2.1}$$

where m_w and m_d are the masses and $\rho_w = m_w/V$ and $\rho_d = m_d/V$ are the partial densities of water and solid in volume V, respectively. The partial density of solid is also commonly called dry density. The standard way to measure the water content of a soil sample is to weigh it before and after oven drying at 105 °C for 24 h [44]. Although this temperature is not high enough to remove all the bound water from bentonite [45, 46], it is still commonly used. The residual water content (only a few percents) can be considered to be a part of the solid material for the method in this thesis. Another, sometimes used quantity for water content is the volumetric water content

$$\theta = \frac{V_w}{V}, \tag{2.2}$$

where V_w is the volume of liquid water and V is the total volume.

Swelling stress

When bentonite absorbs water and its expansion is restricted, swelling stress is created. Swelling stress is isotropic if the structural units in bentonite (layers, stacks, aggregates or grains) are randomly oriented, whereas samples made by uniaxial compaction or made of sedimented bentonite may be more or less anisotropic [47]. The swelling stress depends on dry density, bentonite type and the salinity of water used to saturate the material [25]. The dependence on dry density is approximately exponential. For example, the swelling stress of MX-80 bentonite, fully saturated with pure water, is approximately given by

$$\sigma_s[\mathrm{MPa}] = \exp(6.11 \cdot \rho_d[\mathrm{g/cm^3}] - 7.79) \tag{2.3}$$

for dry densities ρ_d = 1.0–1.7 g/cm^3 [48]. As the dry density of the bentonite buffer in the Finnish nuclear waste repository is planned to be around 1.7 g/cm^3 [33], the swelling stress in the saturated state is around 13 MPa. When applying the method introduced in this thesis, such high swelling stress values may cause challenges in constant volume wetting experiments. The material of the sample chamber needs to be strong enough but at the same time light enough to be transparent for X-rays.

Modeling

In the framework of nuclear waste management, bentonite research primarily aims at better understanding of the behavior of the bentonite buffer in repository conditions, which is needed for reliable safety assessments. Many relevant coupled processes, such as thermal, hydraulic, mechanical, chemical and (micro)biological processes, need to be taken into account when developing comprehensive models for the bentonite buffer [49, 50]. As the modeling has turned out to be very challenging, often only subsets of the processes are considered simultaneously.

The mechanical part is often modeled using some elasto-plastic material model from the field of soil mechanics [51]. The original and modified Cam-Clay models were developed for saturated non-swelling clays. The Barcelona Basic Model (BBM) is an extension of the Cam-Clay models for unsaturated soils. It uses the soil suction (negative water potential) as an extra stress variable, through which it is coupled with the hydraulics. The model was further extended to swelling clays by introducing the Barcelona Expansive Model (BExM). It has two coupled structure levels, active microstructure, and macrostructure that is described by the BBM. This double-structure approach has since been used in many newer variants of the models.

Water transport mechanisms in bentonite are not fully understood. In soil sciences, water transport in unsaturated conditions (pores are partially filled with water) is commonly described using the Darcy's law in a form

$$\vec{q} = -K(h)\nabla H\,, \tag{2.4}$$

where $\vec{q}$ is the volumetric flux vector, $K(h)$ is the hydraulic conductivity, $H = h + z$ is the total head, i.e., the sum of the pressure and the elevation head [52]. Combining Equation 2.4 with the continuity equation

$$\frac{\partial\theta}{\partial t} + \nabla\cdot\vec{q} = 0 \tag{2.5}$$

gives the head-based formulation for unsaturated flow as

$$C(h)\frac{\partial h}{\partial t} = \nabla\cdot\left[K(h)(\nabla h + \nabla z)\right], \tag{2.6}$$

where $C(h) = d\theta/dh$ is the soil water capacity and θ is the volumetric water content (Equation 2.2). Equation 2.6 is also called the Richards equation, and is commonly used in soil science, e.g., to model groundwater transport in the vadose zone. The soil water retention curve $\theta(h)$ and the hydraulic conductivity $K(h)$ are highly non-linear functions, which can be evaluated using, e.g, van Genuchten relations [53], where a few material specific fitting parameters are needed. Equation 2.6 can also be expressed in the saturation-based form

$$\frac{\partial\theta}{\partial t} = \nabla\cdot\left[D_h(\theta)\nabla\theta\right] + \frac{\partial K(\theta)}{\partial z}\,, \tag{2.7}$$

where $D_h(\theta) = K(\theta)\cdot dh/d\theta$ is the hydraulic diffusivity. Apart from the gravitational term $\partial K/\partial z$, the above equation is identical to the diffusion equation

$$\frac{\partial\varphi}{\partial t} = \nabla\cdot\left[D_m(\varphi)\nabla\varphi\right], \tag{2.8}$$

where φ is the concentration and $D_m(\varphi)$ is the mass diffusivity (or diffusion coefficient). This is not surprising since the derivation of the diffusion equation (Equation 2.8) is identical to the derivation of the saturation-based form for unsaturated flow (Equation 2.7). In the case of diffusion, the continuity equation is combined with the Fick's first law

$$\vec{j} = -D_m(\varphi)\nabla\varphi\,, \tag{2.9}$$

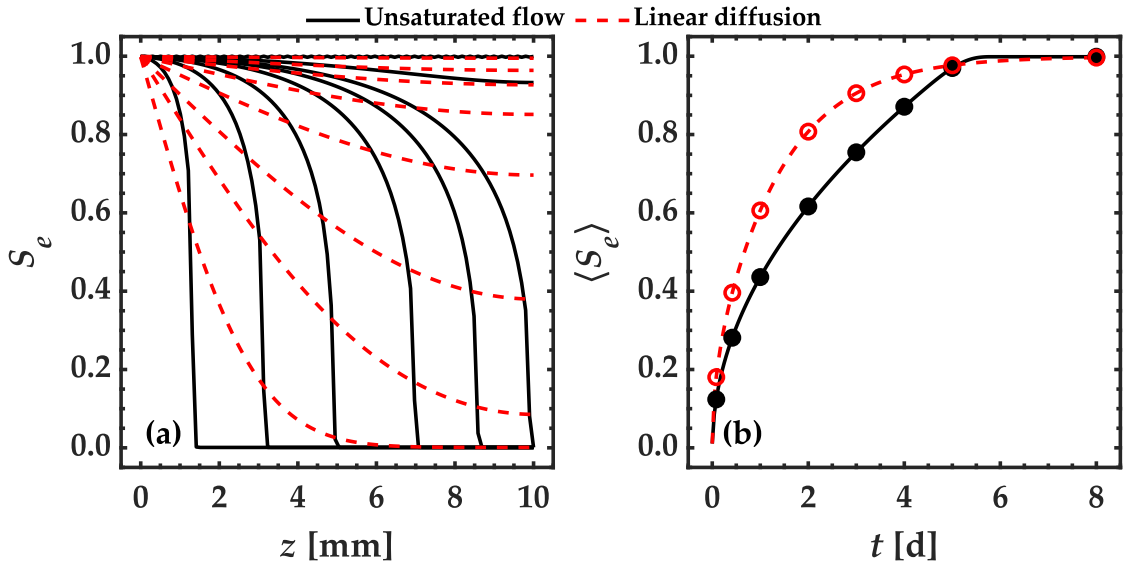

FIGURE 2.4 Comparison of one-dimensional unsaturated flow and linear diffusion of water in bentonite sample. The effective saturation profiles (S_e) at different instants of time show the fundamental difference between the transport mechanisms (a). Also, the effective saturation of the entire sample ($\langle S_e \rangle$) against time shows differences between the transport mechanisms (b). The data points in subfigure b correspond the profiles in subfigure a. The sample is wetted from the end at $z = 0$ mm and the other end at $z = 10$ mm is impermeable to water. Van Genuchten parameters [48] and the mass diffusivity are chosen to correspond the wetting experiment in Figure 5.6. Gravity is ignored.

where $\vec{j}$ is the diffusion flux vector. This equation is similar to the Darcy's law (Equation 2.4). The fundamental difference is that unsaturated flow is driven by the pressure gradient (water potential difference) and diffusion is driven by the concentration gradient (water content difference).

To illustrate the differences of two rather extreme cases, water transport by unsaturated flow (highly non-linear D_h) and by linear diffusion (constant D_m), Figure 2.4a shows one-dimensional effective saturation[1] profiles for both transport mechanisms in a sample wetted from one end. It can readily be seen that the shapes of the profiles are very different. Relatively sharp wetting fronts are visible when the water is transported by unsaturated flow, while such features are not seen in the linear diffusion profiles. Figure 2.4b shows the effective saturation of the entire sample against time. The sample is fully saturated after a certain point in time when water is transported by unsaturated flow, whereas the saturation asymptotically approaches the full saturation value when water is transported by linear diffusion.

[1] The effective saturation is defined as $S_e = (\theta - \theta_r)/(\theta_s - \theta_r)$, where θ_r = residual volumetric water content and θ_s = volumetric water content at full saturation.

Some researchers have pointed out that the soil scientific approach is too simplistic for bentonite as it relates the matric potential (water potential that is related to water soil interactions) to capillary action only and does not consider adhesive effects of chemically active clay minerals [51,54]. Indeed, based on experimental data (e.g., [55] and Figure 5.6), the water transport in bentonite resembles rather linear diffusion than unsaturated flow. Thus, it seems that the traditional soil scientific model for water transport in porous media is not applicable as such for bentonite.

One interesting water transport model, where diffusion is assumed to be the main transport mechanism, is the extended vapor diffusion model [56]. In this model, water first quickly flows and saturates a narrow zone at the wetting end of a bentonite sample. From that zone, water is transported by vapor diffusion in the pore space and diffusion in the interlayer space. Although this model is not coupled with mechanics and some questions remain, the model has performed well when compared to experimental data.

Despite the increased knowledge, there are still challenges in understanding and modeling the mechanical behavior of bentonite and the water transport in it. Hence, detailed experimental data are needed to deepen understanding and to develop and validate better models. As the mechanical behavior and the water transport are likely to be coupled, simultaneous data on deformation and water transport would be very valuable from the modeling point of view.

2.2 Biocomposite

Composite materials [57,58] combine two or more materials to give better properties than each material alone. Usually a composite material consists of a matrix and a reinforcement, which can be, e.g., particles, flakes or fibers. Many natural materials are composites, e.g., wood consists of cellulose fibers in lignin and bone consists of collagen fibers and hydroxylapatite. Some examples of familiar man-made composites are cement paste reinforced with coarse aggregate and steel rods in concrete, and rubber reinforced with carbon black, steel wires and textile layers in tires. In more restricted sense, composite materials are understood to mean polymer matrix composites (PMC). These consist of a polymer matrix (thermoset or thermoplastic) reinforced most often with glass, aramid or carbon fibers. PMC have good strength-to-weight ratio, and resistance to fatigue stress and corrosion. Hence, they are used in many products, most notably in aircraft, cars, boats, sports equipment and construction materials. Some disadvantages of PMC are high material and fabrication cost, adverse effects of moisture and temperature, and possible poor strength in certain directions. PMC can be made by a lay-up technique, where layers of reinforcement mats and matrix material are applied one after another (Figure 2.5a). Another way is to use compression or injection molding, where the matrix and reinforcement are mixed prior to the molding, resulting in more or less

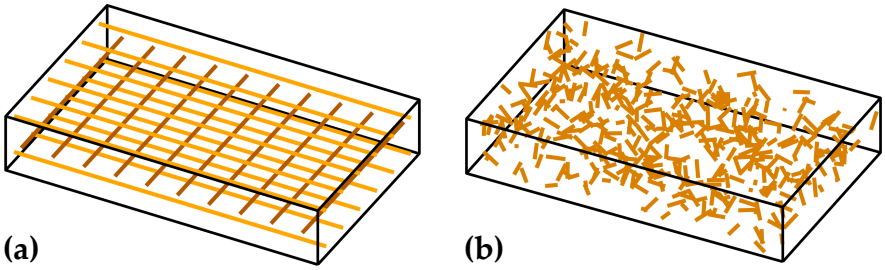

FIGURE 2.5 Fiber composite materials made by lay-up technique (a) and by compression or injection molding (b).

randomly distributed and oriented reinforcements (Figure 2.5b). The fibers in a composite material made by the lay-up technique are effectively infinitely long, whereas the molding processes restrict the fiber length.

Demand for environmental friendly composite materials (biocomposites) has been increased due to increased environmental awareness [59, 60]. Biobased polymers (bioplastics) are renewable alternatives for petroleum-derived counterparts. Some bioplastics are also biodegradable but often only in long timescales or in specific environmental conditions. Examples of bioplastics are polylactic acid (PLA) made from corn starch, and polyamide 11 (Nylon 11) made from castor oil. Natural fibers (biofibers) extracted from wood or plants (e.g., hemp, flax, sisal, jute) are cheap, renewable and biodegradable alternative for artificial fibers. All biofibers extracted from wood or plants consist of cellulose and lignin but the ratio varies. The specific strength of some biofibers is almost as good as that of glass fibers. However, biofibers are more prone to quality differences. Another major disadvantage is the moisture absorption ability. Cellulose fibers are hydrophilic whereas many matrix materials are hydrophobic [61]. Moisture lowers the strength of the fibers, may cause the fibers to detach from the matrix, exposes the fibers to rotting and causes dimensional changes to the composite material. Hence, water transport in such materials is of great importance when studying the performance of biocomposites in practical applications. Better understanding of water transport processes may help to develop more durable materials.

3 X-RAY IMAGING AND TOMOGRAPHY

3.1 X-rays

Electromagnetic waves with wavelengths between around 10 pm and 10 nm (or photon energies 0.1–100 keV) are called X-rays [62]. They have ability to partially penetrate many materials opaque to visible light, and thus their usefulness in imaging applications was realized soon after discovery in 1895. Nowadays, X-rays are routinely used in non-destructive two- and three-dimensional imaging in medicine, security screening, industry and research. Other important applications of X-rays can be found in the fields of X-ray crystallography and X-ray spectroscopy.

Interaction with material

X-rays are attenuated (absorbed or scattered) when they pass through material and interact with electrons, mainly by three mechanisms, by 1) photoelectric absorption, 2) Rayleigh scattering[1] and 3) Compton scattering (Figure 3.1). X-ray photons are effectively absorbed in many materials by photoelectric absorption as the secondary radiation (photoelectrons and characteristic X-rays) is usually stopped close to the point of origin. In both forms of scattering, X-ray photons change direction and can further interact by any mechanism (1–3) or have no interaction (0). The X-ray photon energy is conserved in Rayleigh scattering (elastic scattering), whereas in Compton scattering some part of the energy is transferred to removed electrons (inelastic scattering).

The attenuation of a narrow monochromatic X-ray beam is given by the Beer-

[1] Rayleigh scattering is sometimes also called Thomson scattering. In Thomson scattering, however, a photon is scattered elastically from a single free electron, whereas in Rayleigh scattering a photon is scattered elastically from all the bound electrons of an atom.

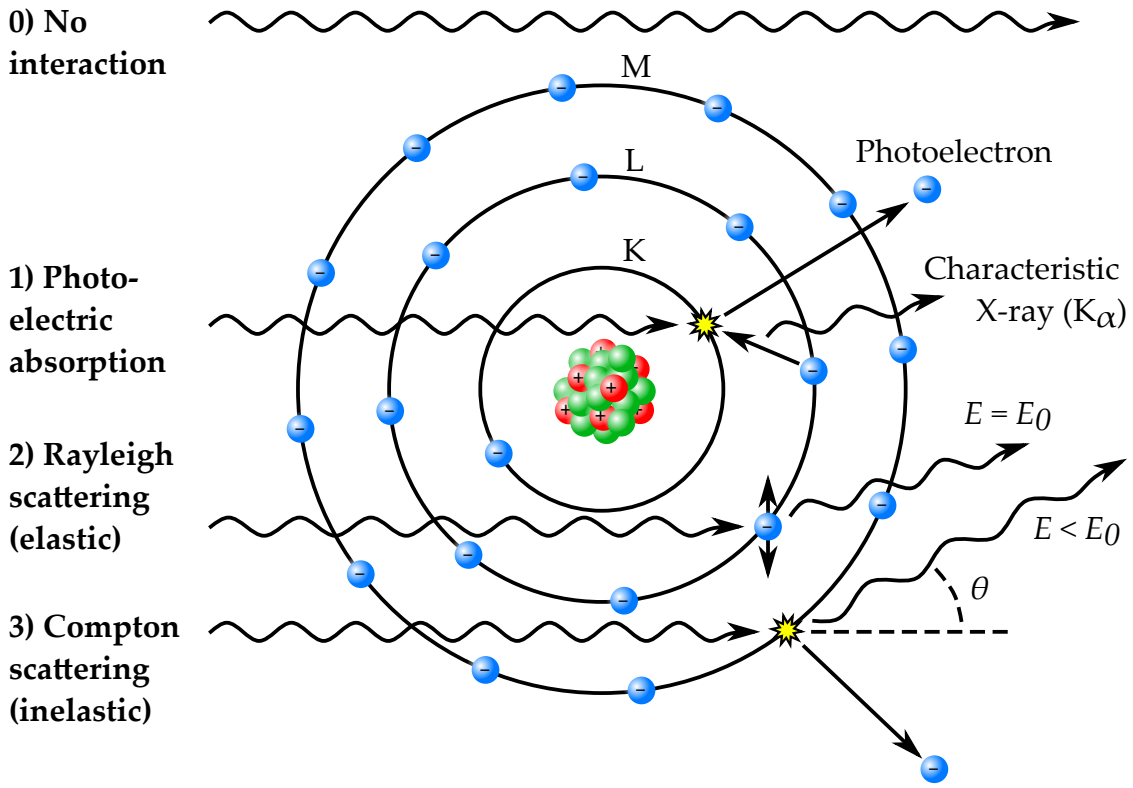

FIGURE 3.1 Main interaction mechanisms of X-rays with atom.

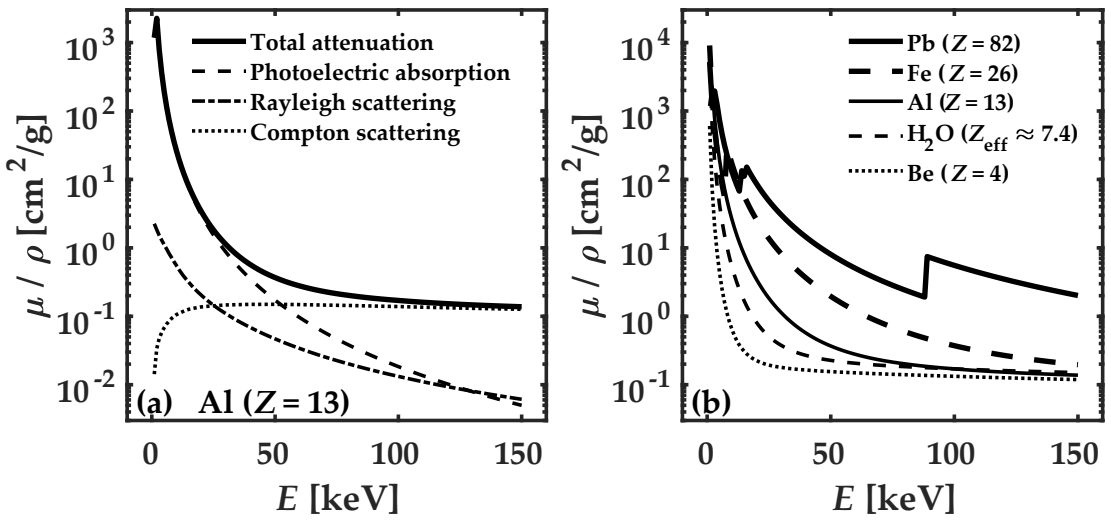

FIGURE 3.2 Mass attenuation coefficients against energy. The mass attenuation coefficient (μ/ρ) is plotted against the photon energy (E) for different interaction mechanisms in aluminum (a) and for selected elements and water (b). The sharp jump is the Pb K-edge (88.0 keV). The data are from NIST XCOM: Photon Cross Sections Database [63].

Lambert law

$$\frac{I}{I_0} = \exp\left(-\int_C \mu dx\right), \tag{3.1}$$

where I/I_0 is the transmittance, I is the intensity of the attenuated X-ray beam, I_0 is the intensity of the unattenuated X-ray beam, μ is the linear attenuation coefficient and x is the position along the X-ray path C. As the linear attenuation coefficient is directly proportional to density ρ, it can be expressed as

$$\mu = c \cdot \rho\,, \tag{3.2}$$

where $c = (\mu/\rho)$ is the mass attenuation coefficient, which depends only on material (atomic number) and photon energy. The mass attenuation coefficient for compounds can be calculated using the mixture rule

$$c = \sum_i W_i \cdot c_i\,, \tag{3.3}$$

where $W_i = m_i / \sum_i m_i$ and c_i are the mass fraction and the mass attenuation coefficient of element i, respectively.

The total mass attenuation coefficient is the sum of the mass attenuation coefficients of each interaction mechanism. These are plotted against photon energy for aluminum (Z = 13) in Figure 3.2a. For this material, the photoelectric absorption dominates below 50 keV and the Compton scattering above 50 keV. Figure 3.2b shows the total mass attenuation coefficients for selected elements and water. In most cases, the mass attenuation coefficient increases with atomic number and decreases with photon energy

Generation

X-rays are generated by two fundamental processes, by atomic energy level transitions and by accelerating charged particles. Both processes are important in an X-ray tube, which is the most common type of X-ray source in laboratory-sized X-ray devices. A schematic illustration of an X-ray tube is shown in Figure 3.3. Thermally emitted electrons from a hot filament are accelerated by the tube voltage between an anode and a cathode. A focused electron beam hits a target material (most often tungsten) in the anode. The electrons violently slow down when passing close or hit the positively charged nuclei of the target atoms. As the electrons experience different degrees of accelerations when slowing down, a continuous energy spectrum of X-rays (bremsstrahlung or braking radiation) is generated. Some of the electrons and the generated X-rays can also kick off electrons from the target nuclei. When electrons from higher energy levels fill these vacancies, the energy differences are emitted as material specific characteristic X-rays (similarly than in the photoelectric absorption in Figure 3.1). X-ray tubes are inefficient in the sense that only around 1% of the electron beam energy is converted to X-rays and the rest is dissipated as heat. The melting point of the target material and the heat transfer characteristics of the anode limit the maximum power of the

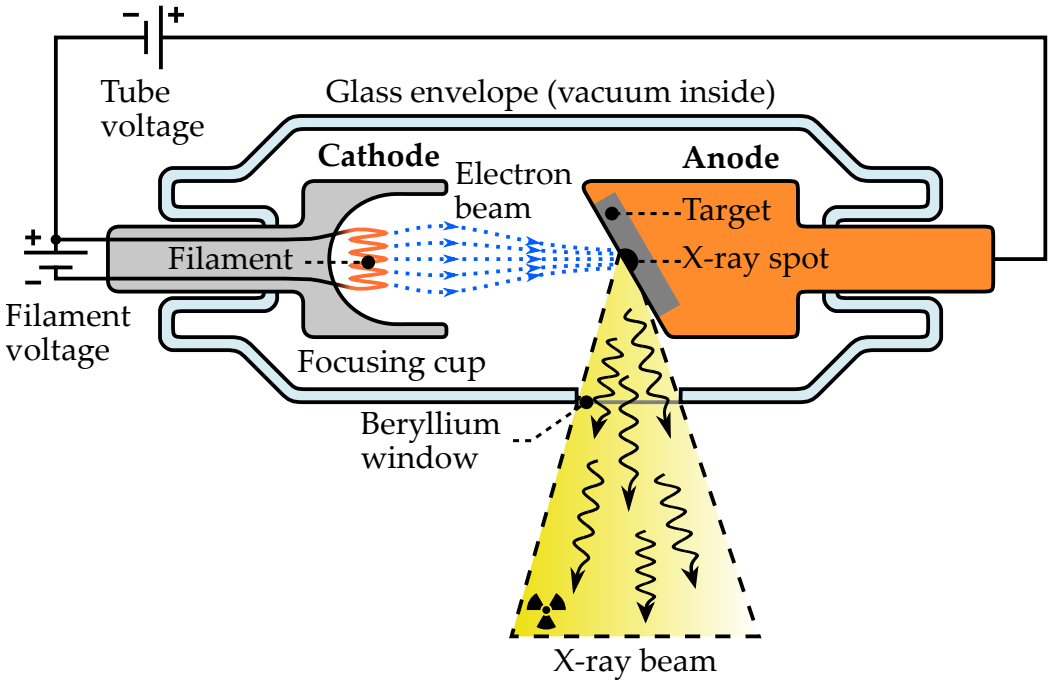

FIGURE 3.3 Schematic cross-sectional view of X-ray tube.

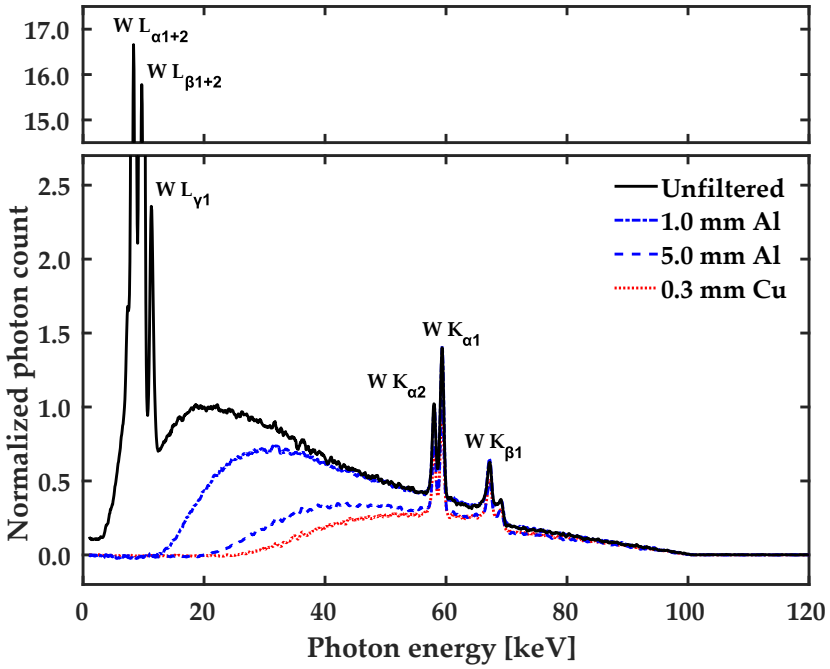

FIGURE 3.4 X-ray tube spectrum with different X-ray filters. The spectra were measured with an Amptek XR-100T-CdTe X-ray spectrometer from a Hamamatsu L12161-07 microfocus X-ray tube, operated at 100 kV. Most visible characteristic peaks of a tungsten (W) target are also labeled. The unfiltered spectrum is inherently filtered by the target and Be-window.

electron beam that can be aimed at a small X-ray focal spot (roughly 200 kW/mm^2 for tungsten) [64].

An example of an unfiltered X-ray tube spectrum is shown in Figure 3.4. The tube voltage (here 100 kV) directly gives the maximum photon energy in electronvolts (100 keV). The spectrum consists of a continuum part and some characteristic peaks of the tungsten (W) target. Also shown are the spectra for different X-ray filter plates in use. The filtering effectively cuts the low energy part of the spectrum but also lowers the total intensity of the X-ray beam. In imaging applications, a suitable energy range is chosen by changing the tube voltage and filtering.

There are also other ways to produce X-rays for imaging purposes, although not so readily available. Extremely high intensity X-rays are produced in synchrotron facilities. There, electrons are first accelerated to relativistic speeds, and then kept rotating in a storage ring (diameter from tens to hundreds of meters). When electrons travel through strong magnetic fields in bending magnets and insertion devices (wiglers and undulators), they experience violent accelerations and produce X-rays, which are utilized in specific beamlines. The high intensity enables fast imaging even after monochromatization of the beam. Other interesting but relatively rare types of X-ray sources are free-electron lasers and inverse Compton sources.

3.2 X-ray imaging

In conventional attenuation-based X-ray imaging (or radiography) [62, 65], a sample is illuminated with an X-ray beam and an intensity image is recorded with a detector (Figure 3.5). There, a scintillator layer converts X-rays into visible light

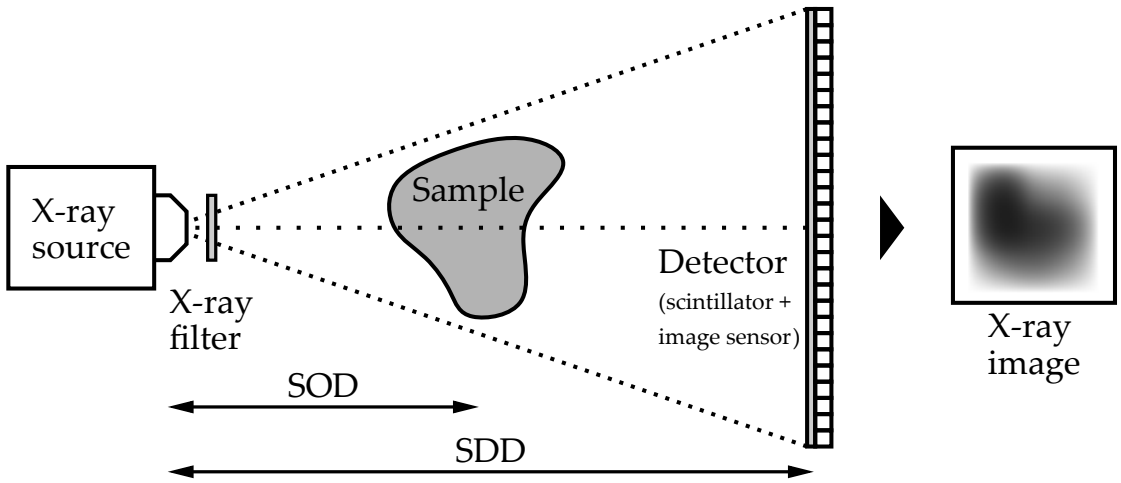

FIGURE 3.5 X-ray imaging setup. SOD is the source-to-object distance and SDD is the source-to-detector distance.

(photoluminescence), which is then captured with an image sensor. Some detectors use fiber optics or mirrors and lenses between the scintillator and the image sensor to match their sizes and to prevent radiation damage to the sensor [66]. In semiconductor image sensors (e.g., CCD, CMOS, TFT), light photons first create electron-hole pairs. The collected electrons within each pixel are then converted into voltages and finally digitized into numerical pixel values of X-ray images. These values are approximately proportional to the X-ray intensities incident to the scintillator. There are also direct semiconductor detectors, where no scintillator is used and X-rays directly produce electron-hole pairs, but these detectors are efficient only for low X-ray energies. Nowadays, photon counting detectors exist, where individual photons can be counted and grouped into several energy bins in each pixel [67]. Such detectors allow spectral X-ray imaging, which can potentially be used, e.g., for material decomposition.

Imaging procedure

Here, a typical procedure in X-ray tube based research or industrial X-ray imaging is described step by step with some additional information related to each step.

1. **Sample positioning.** The sample is positioned relative to the source and the detector in such a way that the whole sample or the region of interest fits in the field of view. The geometrical magnification for a conical X-ray beam is given by
$$M = \frac{\mathrm{SDD}}{\mathrm{SOD}}, \tag{3.4}$$
where SDD is the source-to-detector distance and SOD is the source-to-object distance. Hence, the image pixel size is given by
$$p_i = \frac{p_d}{M} = p_d \cdot \frac{\mathrm{SOD}}{\mathrm{SDD}}, \tag{3.5}$$
where p_d is the detector pixel size. A small image pixel size and high resolution are thus achieved by placing the sample near the source or moving the detector farther away. These adjustments have, however, some drawbacks. When the sample is close to the source, the blurring caused by the finite size of the X-ray spot limits the resolution at high magnifications. Also, increasing the SDD decreases the intensity according to the inverse square law. Some devices (e.g., Xradia MicroXCT-400, see Figure 3.11) use minimal geometrical magnification together with high optical magnification between the scintillator and the image sensor. This technique produces a smaller half-shadow (blurring) and thus a better resolution than would be achieved using high geometric magnification alone.
2. **Tube voltage and X-ray filtering.** The transmittance through the sample is adjusted by changing the tube voltage and the X-ray filtering (i.e., changing the spectrum, see Figure 3.4). Thick, dense and high atomic number materials require higher energies, whereas lower energies are used for small and light samples. The optimal transmittance through the thickest part of the sample

is typically between 0.1 and 0.5. However, as the optimal settings are sample and device specific, it is best to perform optimization tests to find the settings that maximize the contrast-to-noise ratio between the details of interest.

3. **Tube current and exposure time.** The pixel values of X-ray images are proportional to the tube current and the detector exposure time. These are adjusted in such a way that the pixel values are in the linear response range and overexposure is avoided. Typically, the pixel values are then between 50% and 90% of their maximum value obtained without the sample in the field of view.
4. **Exposure.** A single X-ray image is taken of the sample, or alternatively several images of the same setup are taken and averaged to increase the signal-to-noise ratio.
5. **Flat-field correction.** The standard way to correct detector dark current (temperature-induced signal), gain and offset differences between different pixels and uneven intensity distribution of X-rays is to apply the flat-field correction (FFC)

$$\frac{I}{I_0} = \frac{I' - I_D}{I_B - I_D}, \tag{3.6}$$

where I/I_0 is the flat-field corrected transmittance, I' is the raw X-ray image (taken in step 4), I_D is the dark field (image taken without X-rays) and I_B is the bright field (image taken with X-rays and without sample). Although the FFC cannot correct nonlinear variations, it is usually sufficient in conventional X-ray imaging.

Radiographic reconstruction

Radiographic reconstruction means here calculation of the two-dimensional linear attenuation coefficient map of the sample from a single X-ray image. This requires knowing the thickness map of the sample, which is easily calculated for the samples of simple shape, e.g, for a cylindrical sample in a tube (Figure 3.6). The Beer-Lambert law (Equation 3.1) can now be written as

$$\mu_s x_s + \int_{C_0} \mu dx = -\ln\left(\frac{I}{I_0}\right)_c, \tag{3.7}$$

where μ_s is the average linear attenuation coefficient and x_s is the thickness of the sample along the line from the source to a detector pixel. The term $\int_{C_0} \mu dx$ includes all the other materials except the sample along the same line (e.g., sample holder tube). This term can be calculated if the μ is known along the path C_0, but is easily obtained by taking an X-ray image without the sample ($x_s = 0$). It is important that beam hardening corrected transmittance $(I/I_0)_c$ is used on the right side of Equation 3.7 so that the Beer-Lambert law is valid (see Sections 3.4 and 4.3 for beam hardening correction).

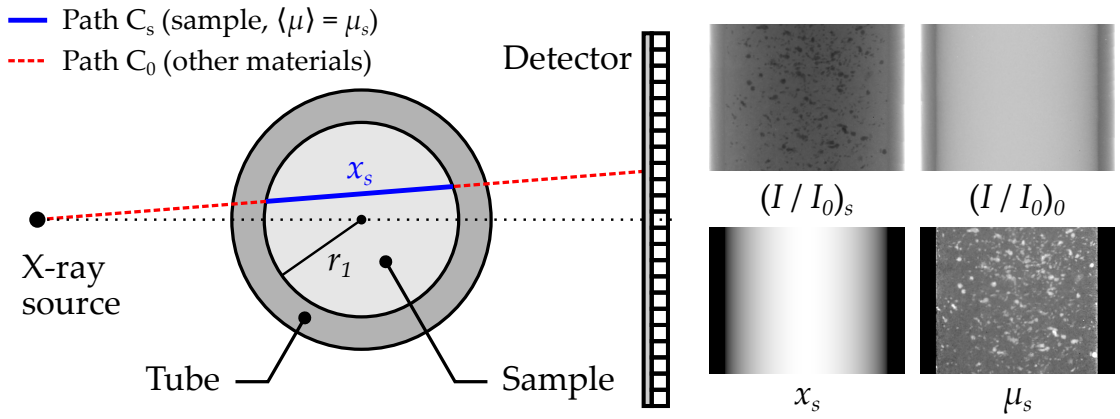

FIGURE 3.6 Radiographic reconstruction for cylindrical sample in tube. For this sample, the thickness x_s for each ray can easily be calculated using the known geometry. The transmittance of the sample tube with $(I/I_0)_s$ and without $(I/I_0)_0$ sample can then be used to calculate the linear attenuation coefficient map of the sample μ_s.

3.3 X-ray tomography

In X-ray tomography (or computed tomography, CT) [62, 65, 68–70], X-ray images taken around a sample are used to calculate the three-dimensional structure of the sample. The imaging setup is similar to that of X-ray imaging (Figure 3.5), but now the sample is rotated around the vertical axis between consecutive X-ray images (Figure 3.7a).

In X-ray tomography, the procedure is typically the following.

1. **Sample positioning.** The sample is positioned similarly than in X-ray imaging (see Section 3.2), but now the sample needs to fit in the field of view horizontally to avoid missing data, which may lead to challenges in the reconstruction stage

2.-5. Similar to X-ray imaging (see Section 3.2).

6. **Angles.** The X-ray images are taken from evenly spaced angles covering either the half circle (180° + cone angle) or the full circle (360°). The number of X-ray images affects the quality of reconstructed images and is discussed later (see Equation 3.14 and Figure 3.9).
7. **Scan.** X-ray images from the different angles are taken with the settings chosen above. The sample is either continuously rotated or the rotation is stopped at each angle during the exposure.
8. **Reconstruction.** X-ray tomographic reconstruction is a process where the X-ray images taken from different angles around the sample are used to calculate the three-dimensional linear attenuation coefficient distribution of the sample (Figure 3.7b). Reconstruction produces axial cross-sectional images of the sample (slices), which can be stacked to obtain the full three-

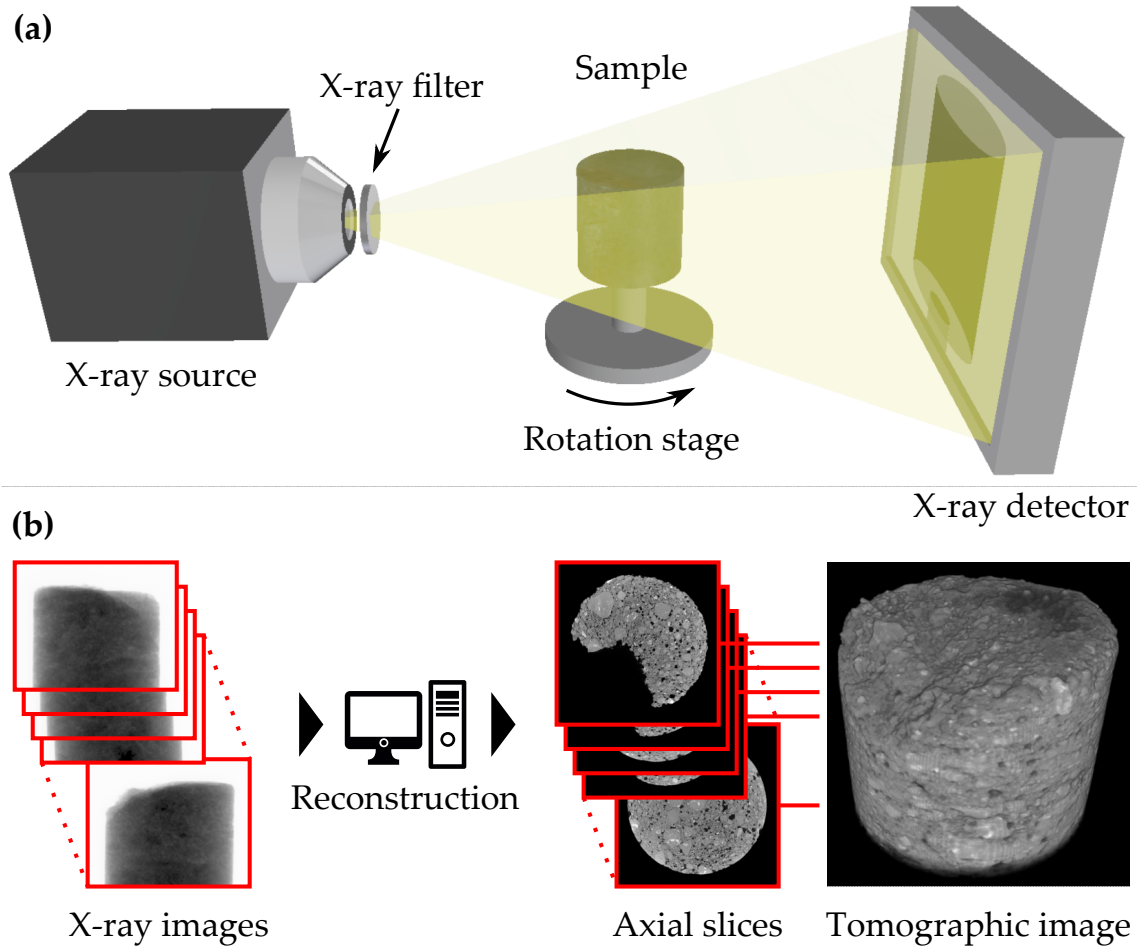

FIGURE 3.7 Imaging setup (a) and reconstruction (b) in X-ray tomography.

dimensional image. Reconstruction is discussed in more detail below.

Tomographic reconstruction

Tomographic reconstruction is an inverse problem (inverse Radon transform) and requires special solving techniques as the underlying mathematical problem is sensitive to noise and is often underdetermined. The principle of reconstruction is here first illustrated using two-dimensional parallel beam geometry.

Direct Fourier reconstruction utilizes the projection slice theorem

$$\mathcal{F}_{1D}\{\mathcal{P}f\} = \mathcal{S}\mathcal{F}_{2D}\{f\}\,, \tag{3.8}$$

where f is a two-dimensional function, $\mathcal{F}_{1D}$ and $\mathcal{F}_{2D}$ are the one- and two-dimensional Fourier transforms, and $\mathcal{P}$ and $\mathcal{S}$ are the projection and slicing operators (Figure 3.8). This reconstruction method is, however, impractical due to errors arising from tricky interpolation in the Fourier space. The interpolation can

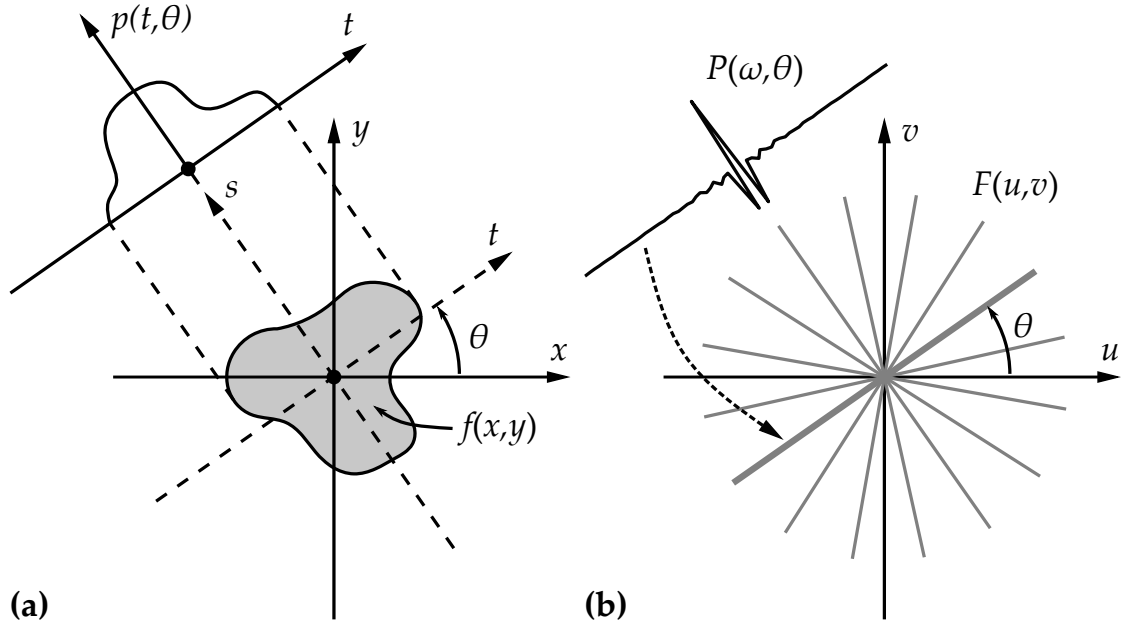

FIGURE 3.8 Projection slice theorem. The projection of a two-dimensional function $f(x,y)$ at the angle θ is $p(t,\theta) = \int_{-\infty}^{\infty} f(x,y)ds$ (a). The Fourier transform of the projection is $P(\omega,\theta)$, which corresponds data on a line at the angle θ in the Fourier space (b). In direct Fourier reconstruction, the function $F(u,v)$ is estimated by taking projections from different angles and filling the Fourier space with corresponding lines. An estimate for the original function f is then obtained by taking the inverse Fourier transform of the function F.

be avoided by writing the two-dimensional inverse Fourier transform as

$$f(x,y) = \int_{-\infty}^{\infty}\int_{-\infty}^{\infty} F(u,v)\exp[i2\pi(ux+vy)]dudv \tag{3.9}$$

and performing the change of variables $u = \omega\cos\theta$ and $v = \omega\sin\theta$. This leads to the filtered back projection (FBP) formula for the parallel beam geometry

$$f(x,y) = \int_{0}^{\pi}\int_{-\infty}^{\infty} P(\omega,\theta)|\omega|\exp[i2\pi\omega(x\cos\theta + y\sin\theta)]d\omega d\theta\,. \tag{3.10}$$

In this form, each Fourier transformed projection P is first filtered with the ramp function $|\omega|$, then inverse Fourier transformed, and finally back projected to form the function f. Another formulation of Equation 3.10 is obtained by using the convolution theorem

$$\mathcal{F}\{p * h\} = \mathcal{F}\{p\}\cdot\mathcal{F}\{h\}\,, \tag{3.11}$$

where $\mathcal{F}$ is the Fourier transform, $*$ denotes the linear convolution and $\cdot$ denotes the point-wise multiplication. Now the FBP formula (Equation 3.10) can be written

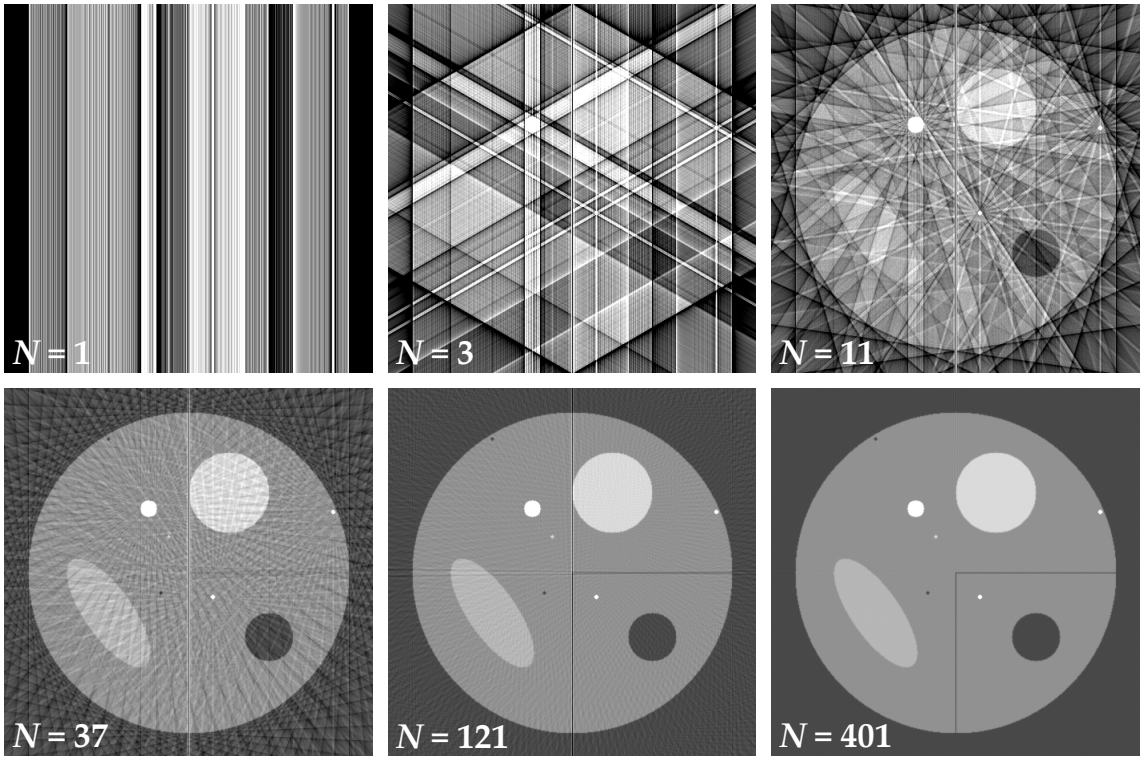

FIGURE 3.9 Filtered back projection reconstruction of simulated phantom (diameter 400 px) with different number of projections (N).

as

$$f(x,y) = \int_0^{\pi} (p * h)(x\cos\theta + y\sin\theta, \theta) d\theta \,. \tag{3.12}$$

In this form, the projections are filtered (convolved) with the kernel

$$h(t) = \int_{-\infty}^{\infty} |\omega| \exp(i2\omega t) d\omega \tag{3.13}$$

before the back projection.

To illustrate the back projection process and the effect of the number of projections N, FBP reconstructions of a simulated phantom with different values of N are shown in Figure 3.9. The image quality gradually increases with N. It seems that particles and other round objects can be detected with a relatively small number of projections, while more projections are required to properly reconstruct thin slits. Theoretically, the required number of projections for a faithful reconstruction can be justified by the Nyquist-Shannon sampling theorem and is given as

$$N \geq \frac{\pi}{2} \cdot D[\text{px}] \approx D[\text{px}] \,, \tag{3.14}$$

where D is the width of the sample in pixels. As the image quality is fairly good even with much lower values of N, the approximation gives an easy rule of thumb

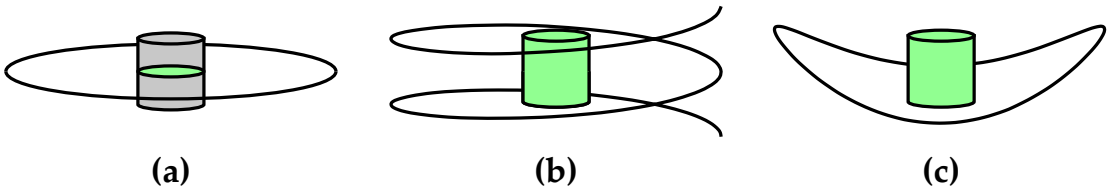

FIGURE 3.10 Tuy's data sufficiency condition for circular (a), helical (b) and saddle trajectories (c). Exact reconstruction is possible in the areas marked in green.

to remember: the required number of projections for high-quality reconstruction is the width of the sample in pixels.

The Feldkamp-David-Kress (FDK) algorithm [71] is an extension of the filtered back projection to the cone beam geometry. The FDK algorithm is approximate since exact reconstruction is not possible with any algorithm when a circular source trajectory is used. Tuy's data sufficiency condition states that exact reconstruction is possible at those points in the sample through which every plane intersects the source trajectory [72]. Hence, the common circular trajectory produces sufficient data only for the orbital plane and the reconstruction is approximate elsewhere (Figure 3.10a). The approximation and the image quality get worse with the cone beam angle (see section 3.4). Exact reconstruction is, however, possible if certain other types of source trajectories are used, such as helical or saddle trajectories (Figures 3.10b and 3.10c).

In iterative reconstruction (IR) algorithms [68,73–75], a large set of linear equations is formed by integrating the voxel (volumetric pixel) values along each ray from the source to the detector pixels according to the Beer-Lambert law (Equation 3.1). These ray sums are then compared with the projection values obtained from the X-ray images. The voxel values are updated at each iteration step such that the ray sums get closer to projection values, and the iterations are stopped when the difference is small enough. IR algorithms have many advantages compared to the FBP. They produce less noisy results and handle missing or sparse data better. Also prior information of the sample can easily be added. However, there are some downsides, IR algorithms are computationally intensive, there might be stabilization issues and small details may appear blurred in some cases. IR algorithms are nowadays popular in medical imaging to reduce dose, but for some reason those have not gained so much popularity in research and industry.

Image storage

X-ray tomography produces a large amount of data. For example, the file sizes of projection and reconstruction data sets produced by 1k $\times$ 1k detectors are typically a few gigabytes, by 2k $\times$ 2k detectors tens of gigabytes and by 4k $\times$ 4k detectors hundreds of gigabytes. Further image processing may also create many similar-

sized files. File sizes can be reduced by image binning, cropping and choosing a lower bit depth for saved images. Image binning means combining $n \times n$ X-ray image pixels into one using hardware (in detector) or software binning. Similarly, $n \times n \times n$ tomographic image voxels can be binned into one using software binning. Binning reduces the size and required number of projection images, and shortens scan time at the expense of resolution. If the sample is much smaller than the field of view, unnecessary areas can be cropped from the projections and the reconstructed images. X-ray detectors typically use 12-, 14- or 16-bit digitization and the resulting X-ray images are often saved as 16-bit (unsigned integer) images. As the reconstructed images may contain a wide range of linear attenuation coefficient values, they are preferably saved as floating point images (e.g., 32-bit). However, 8- or 16-bit (unsigned integer) image formats are often used to reduce file sizes. In such a case, the linear attenuation coefficient values are linearly mapped to integers ($g : \mathbb{R} \rightarrow \{0, 1, \ldots, g_{\max}\}$) as

$$g(\mu) = \begin{cases} 0\,, & \mu < \mu_{\min} \\ \text{Round}\left(g_{\max} \cdot \frac{\mu - \mu_{\min}}{\mu_{\max} - \mu_{\min}}\right)\,, & \mu_{\min} \leq \mu \leq \mu_{\max} \\ g_{\max}\,, & \mu > \mu_{\max}, \end{cases} \tag{3.15}$$

where $g_{\max} = 2^k - 1$ is the maximum voxel value of the k-bit image (8-bit: $g_{\max}$ = 255, 16-bit: $g_{\max}$ = 65535), and $\mu_{\min}$ and $\mu_{\max}$ are the minimum and maximum linear attenuation coefficient values for the conversion.

X-ray tomography devices

In medical CT devices, human-sized samples can be imaged with a spatial resolution of around 1 mm. There, the X-ray source and the detector are rotating inside a gantry while the patient is laying stationary on the table. The detector is usually wide but has a small number of pixel rows. The axial coverage is obtained by moving the table in the axial (horizontal) direction during the scan. In medical imaging, the primary aim is to keep the radiation dose level as low as possible to still achieve diagnostic image quality. Although medical CT devices are designed for imaging humans, they have also been successfully used in material research [76,77].

Microtomography (μCT) devices are used to obtain high-resolution (1–100 μm) three-dimensional images of relatively small samples (1–100 mm) [78]. This resolution range allows to study three-dimensional structures of many heterogeneous materials, and hence μCT has gained popularity especially in material sciences, biology and industry. To achieve such high resolution, a microfocus X-ray tube or a synchrotron X-ray source is needed to generate the X-rays. In μCT, the source and the detector are typically stationary while the sample is rotated during the image acquisition (see Figure 3.7a). In the applications of this thesis, X-ray imaging and X-ray tomography were performed using Skyscan 1172 and Xradia (ZEISS) MicroXCT-400 microtomography devices (Figure 3.11 and Table 3.1), located at the X-ray Tomography Laboratory at the University of Jyväskylä.

TABLE 3.1 Some specifications of Skyscan 1172 and Xradia MicroXCT-400 microtomography devices.

	SkyScan 1172	Xradia MicroXCT-400
Tube voltage	20–100 kV	20–90 kV
Max. tube power	10 W	8 W
Min. X-ray spot size	5 µm at 4 W	5 µm at 4 W
Max. spatial resolution	4 µm	1 µm
Max. sample diameter	3–50 mm	0.6–10 mm
Camera pixels	4k × 2k	2k × 2k

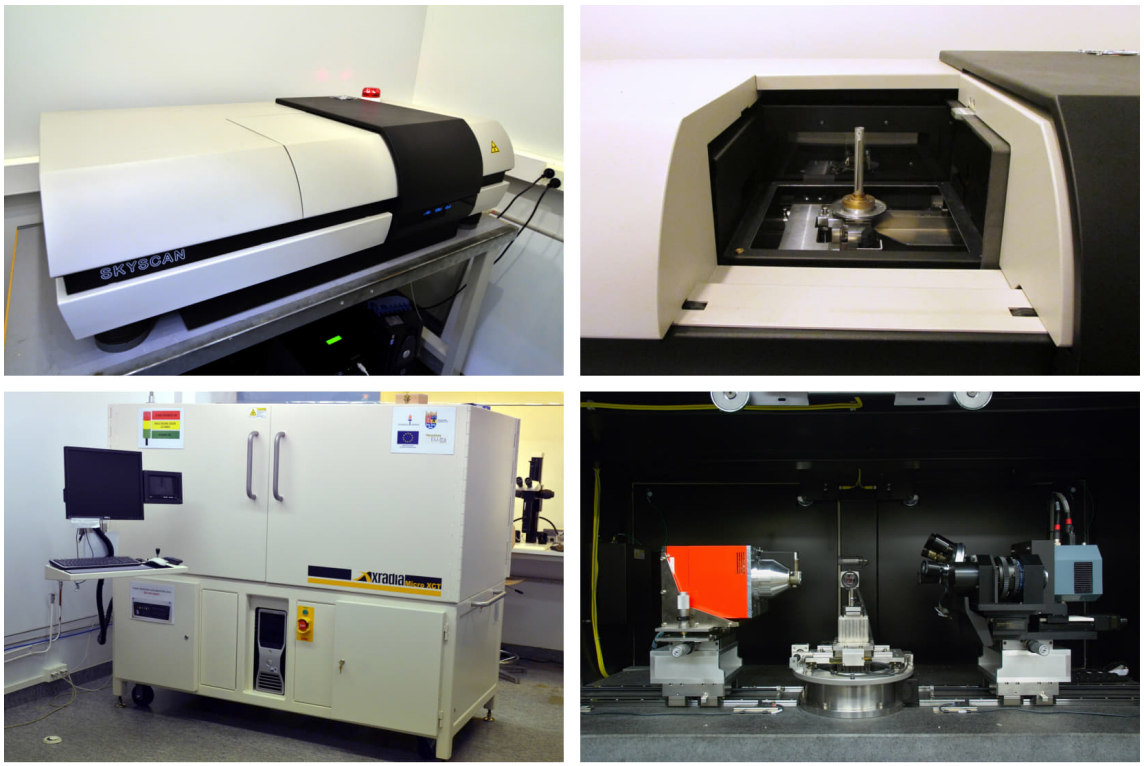

FIGURE 3.11 SkyScan 1172 (top row) and Xradia MicroXCT-400 (bottom row) microtomography devices.

3.4 Image artifacts

Both X-ray images and X-ray tomographic images may contain several different types of image artifacts [79] that hamper image analysis. Correcting them is thus important for quantitative image analysis. As X-ray tomographic images are reconstructed from X-ray images, most of the artifacts present in X-ray images manifest themselves also in X-ray tomographic images. However, some artifacts appear in X-ray tomographic images only. This section describes the most relevant image artifacts and their correction methods encountered in this thesis.

Noise

Noise is an unwanted signal that obscures the desired signal. Two types of noise are often present in X-ray images, fixed-pattern noise and random noise. Fixed-pattern noise arises, e.g., from gain and offset differences in camera pixels and is similar between different exposures. Random noise may consist of shot noise, dark noise and read-out noise. Shot noise is related to random fluctuations in photon or generated electron numbers and follows Poisson statistics. Dark noise is similar to shot noise but arises from temperature dependent dark current. Read-out noise is generated during the analog-to-digital conversion in the sensor.

Fixed-pattern noise is usually well corrected by the standard flat-field correction (Equation 3.6). Random noise in X-ray images can be reduced by averaging multiple images instead of a single exposure or by binning images. Noise also propagates to X-ray tomographic images, where it can be reduced by increasing the number of X-ray images, binning or using more noise-resistant reconstruction algorithms. Noise can also be reduced by numerous image processing filters, but care should be taken to avoid over-smoothing that may distort the underlying signal and remove important details.

Beam hardening

Beam hardening is an artifact caused by a polychromatic energy spectrum. As lower energy X-ray photons attenuate more efficiently than higher energy ones (see Figures 3.2 and 3.4), the average photon energy increases with material thickness. Therefore, the effective linear attenuation coefficient appears to decrease with the thickness of material (μ_{eff} = secant in Figure 3.12a). Beam hardening is not visually evident in X-ray images and is not usually corrected in X-ray imaging if the absolute transmittance values are not important. However, beam hardening is often very visible in X-ray tomographic images. A measured linear attenuation coefficient profile across a homogeneous sample is flat for monochromatic X-rays (Figure 3.12b), but for polychromatic X-rays the edges of the sample appear to be denser than the interior, and the profile is concave upward (Figure 3.12c). The effect of beam hardening can be reduced by using X-ray filters, which cut the lower part of the spectrum, where the mass attenuation coefficient changes the most (see Figure 3.2). However, filtering alone may not be enough, the standard beam hardening correction is often applied. It uses a quadratic polynomial in the form

$$\ln\left(\frac{I}{I_0}\right)_c = A_1 \cdot \ln\left(\frac{I}{I_0}\right) + A_2 \cdot \ln^2\left(\frac{I}{I_0}\right), \tag{3.16}$$

where $(I/I_0)_c$ is the corrected transmittance, $A_1 = 1$ (usually) and A_2 is chosen in such a way that the effect of beam hardening is minimized in the reconstructed images (i.e., choosing the value for A_2 that produces the flattest profile across the sample) [80]. Real samples are, however, rarely homogeneous, which makes it difficult to determine the correct value of A_2. As the same value of A_2 is used for every pixel, the standard beam hardening correction assumes that the effect

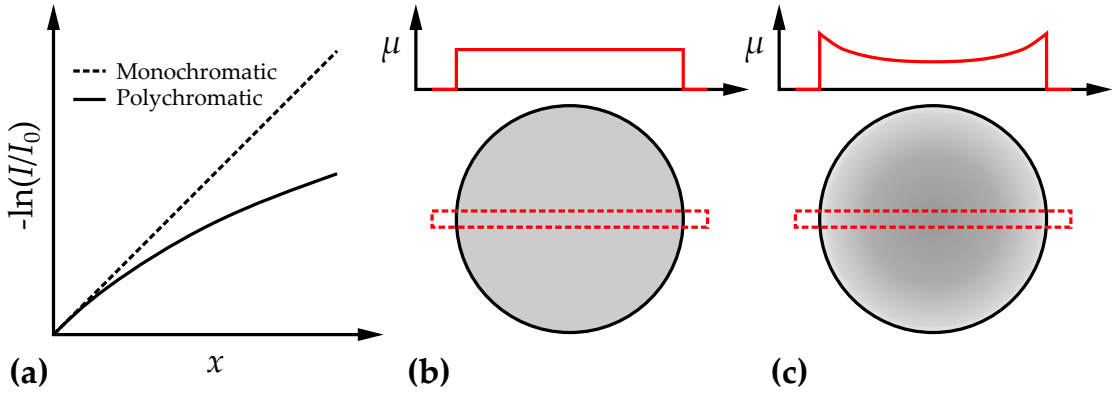

FIGURE 3.12 Beam hardening. The measured logarithmic transmittance is plotted against material thickness (x) for monochromatic and polychromatic X-rays (a). The linear attenuation coefficient profiles across reconstructed slices of a homogeneous sample are different for monochromatic (b) and polychromatic X-rays (c).

of beam hardening is uniform across X-ray images. This is usually not the case, e.g., due to anode heel effect (see below). The standard beam hardening correction may be adequate in conventional imaging, but to improve accuracy, local beam hardening correction was developed (see Section 4.3). Unfortunately, polynomial beam hardening correction methods do not fully work for different types of materials simultaneously. If the sample consists of materials whose effective atomic numbers[2] greatly differ from each other, image regions corresponding to one of them might be well corrected, while other regions are under- or overcorrected.

Anode heel effect

In X-ray tubes, the generated X-rays travel different distances from the X-ray focal spot to the surface of the target depending on direction (Figure 3.13, see also Figure 3.3). The distances are, on average, longer on the anode side, and hence the intensity is more attenuated on that side. This intensity variation is called anode heel effect. As the generated X-rays are polychromatic and the target material acts as an inherent X-ray filter, it is evident that the X-ray spectrum also depends on direction such that X-rays are harder on the anode side. It is also possible that surface roughness of the target creates irregular intensity and spectral variations. The standard flat-field correction (Equation 3.6) is often sufficient to correct the intensity variations in conventional imaging. Anode heel effect can be reduced by using a smaller part of the beam (smaller cone angle). Better correction is, however, achieved by using the local beam hardening correction (see Section 4.3).

[2] The effective atomic number of a compound can be approximated as $Z_{\text{eff}}^{3.5} = \sum_i f_i \cdot Z_i^{3.5}$, where f_i and Z_i are the fraction of electrons and the atomic number of component i, respectively [81].

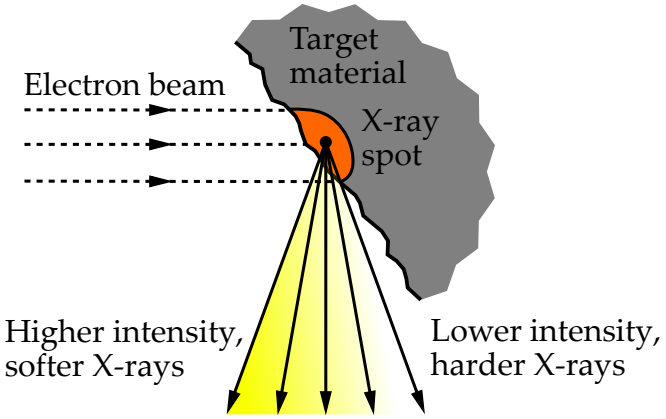

FIGURE 3.13 Anode heel effect. The average travel distance in the target is longer on the anode side (right), which lowers the intensity but hardens the beam.

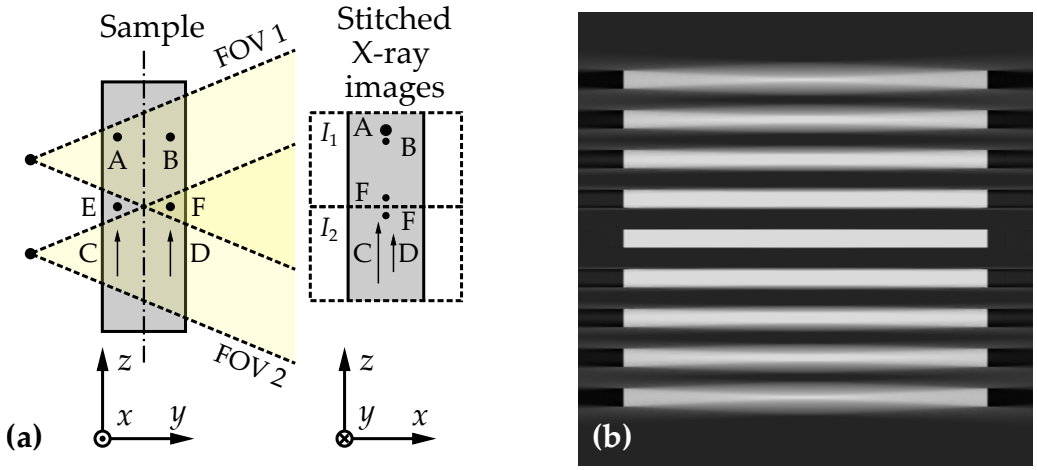

FIGURE 3.14 Cone beam related artifacts. Two identical particles (A and B), at the same height, appear to have different sizes and be at different vertical positions in an X-ray image (a). Similarly, displacements (C and D) may appear different at different y-positions. When X-ray images are stitched along the center line, some details (E) are missing and some (F) are duplicated. In X-ray tomography, the cone beam artifact is often visualized with a vertical slice of a Defrise phantom (or 'Feldkamp killer') consisting of equidistant discs (b). The image quality decreases with the distance from the orbital plane.

Cone beam related artifacts

In X-ray imaging, the conical beam causes some geometrical artifacts in images. The apparent sizes, positions and in dynamic processes also displacements of details in X-ray images depend on their distance from the source (Figure 3.14a). If X-ray images taken next to each other are stitched together, visible discontinuities of details may occur at the seams of the stitched images. Some details may also disappear or get duplicated near the seams. Slight transmittance variations may occur due to longer travel distances of inclined rays. These artifacts can be reduced by using a smaller cone angle, which is achieved by increasing the source-to-detector distance or by cropping the images.

In X-ray tomography, cone beam reconstruction algorithms take into account the imaging geometry, and hence the resulting image is, in principle, spatially accurate (details are in the right places) if no other artifacts and distortions are present. However, as the data acquired using the conical beam and the circular source trajectory are incomplete (see Section 3.3), the interfaces that are not parallel to X-rays (at any rotation angle) are not reconstructed properly. The image quality also degrades with the distance from the orbital plane. (Figure 3.14b). This is called cone beam artifact and can be somewhat reduced by using a smaller cone beam angle or can be totally avoided by using a trajectory that satisfies the Tuy's data sufficiency condition (e.g., helical trajectory). However, in many tomography devices that use cone beam geometry, the standard circular trajectory is the only option.

Scattering and blurring

The measured intensity at the detector is the sum of the intensities of primary X-rays (no interaction) and the X-rays scattered from the sample ($I = I_p + I_s$) (Figure 3.15). As the scattered X-rays produce a blurred version of the sharp image, scattering lowers contrast, adds systematic error, and thus hampers quantitative measurements based on the Beer-Lambert law (Equation 3.1). The scatter-to-primary ratio (I_s / I_p) increases with X-ray energy and decreases with the effective atomic number (see Figure 3.2). The intensity of scattered X-rays also depends on the distance between the sample and the detector according to the inverse square law.

Another effect of scattering is diffraction, where collective elastic scattering from atoms produces constructive and destructive interference patterns on the detector. This is utilized, e.g., in X-ray diffraction and phase contrast X-ray imaging. In this work, diffraction effects are, however, assumed to be negligible due to the low interaction probability of Rayleigh scattering and the use of polychromatic energy spectrum.

The primary and scattered X-rays are also subject to further scattering on the detector side, e.g., from a protective layer of scintillator, X-ray filters (placed

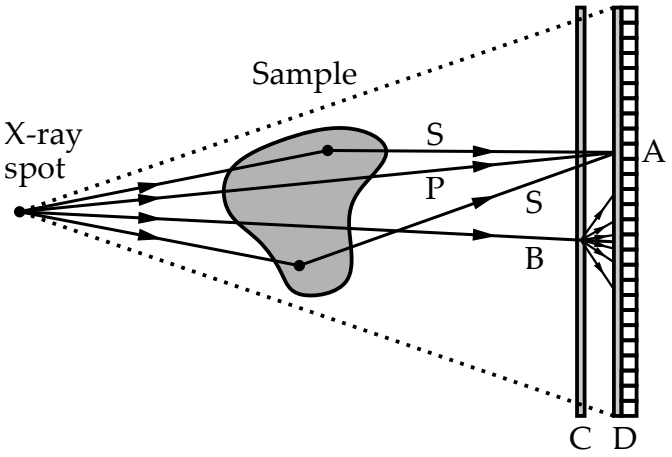

FIGURE 3.15 X-ray scattering in X-ray imaging setup. The intensity measured at point A at the detector (D) consists of primary (P) and scattered (S) X-rays. Each X-ray hitting the detector may further scatter (drawn here only for B) from a plate (C) between the sample and the detector (e.g., from a protective layer of scintillator or from an X-ray filter placed on the detector side in some devices).

on detector side in some models) and the scintillator itself (Figure 3.15). This scattering is one source of blur in images. Other sources giving a similar effect are, e.g., a finite size of X-ray spot, light scattering in the scintillator and charge spreading in the sensor.

Due to complicated nature of scattering and blurring, they are difficult to fully correct. Anti-scatter grids can be used to block most of the scattered X-rays at the detector. Beam-stop or beam-pass arrays can be used to estimate scatter fields. The contribution of scattering and blurring may also be estimated by simulations. In this thesis, a deblurring method based on deconvolution was used to remove the effect of blurring in one application (Section 5.4). This method is introduced in Section 4.2.

Scintillator memory effects

Common scintillator memory effects are bright burn, afterglow and radiation degradation [82–84]. Bright burn is seen as increasing light yield after the start of irradiation. Some of the electrons excited by X-rays fill metastable traps (caused by crystal defects) instead of creating light in luminescence centers. When the traps start to fill up, a larger amount of electrons are available for light production, and finally in the equilibrium state, the light yield saturates to its maximum value. The decay of the metastable trapped states is called afterglow. Long-term irradiation causes also permanent damage to scintillator materials. Although the exact damage mechanisms are not fully understood, the predominant mechanism is believed to be radiation-induced color center formation. These centers absorb visible light, and hence the optical transmittance of the scintillator decreases and it appears to produce less light. Memory effects may create ghost images of

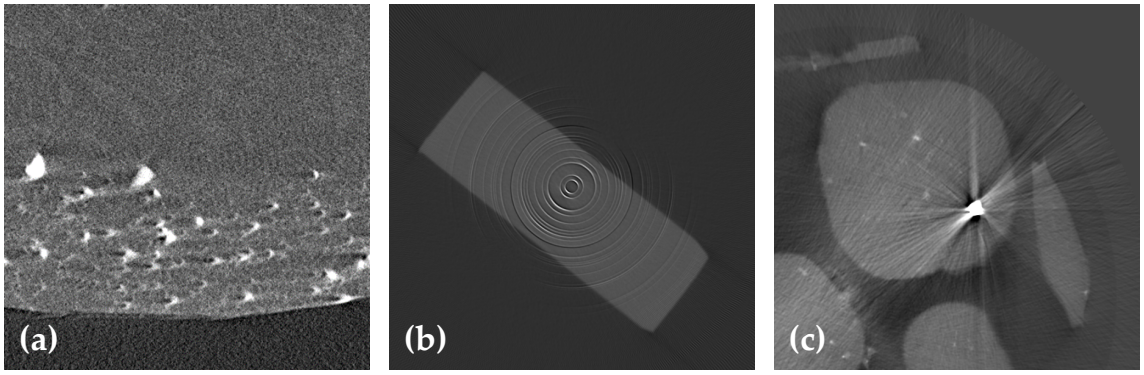

FIGURE 3.16 Image artifacts in X-ray tomographic images. A motion or misalignment artifact (a), ring artifacts (b) and a streak artifact (c).

previously imaged samples as different parts of the scintillator are irradiated differently. Such ghost images are usually well corrected using the flat-field correction (Equation 3.6). Typically, the bright and dark fields are obtained only once or a few times during the scan, which may be sufficient for permanent and slowly disappearing ghost images, but for faster effects the flat-fields need to be taken more frequently. The adverse effects of bright burn and afterglow can be reduced by irradiating the detector some time before the imaging and by waiting some time before dark field image is taken, respectively.

Undersampling

The effect of the number of projections on image quality was already discussed in Section 3.3. Acquiring too small number of projections (undersampling) produces radiating lines and streaks from the edges of objects in reconstructed images (see Figure 3.9). Obviously, these artifacts can be reduced by increasing the number of projections.

Motion and misalignment artifacts

A prerequisite for a high-quality image is that the sample does not move or deform during the imaging (apart from the controlled rotation in X-ray tomography). Otherwise, the image may contain double images or the details may be blurry and distorted (Figure 3.16a), and further image analysis may not be possible. It is challenging to keep the movements below the image resolution during long scans (hours to days). If dynamic processes are imaged, the exposure time and the scan duration should be chosen such that clear enough snapshots of the process can be obtained.

Motion artifacts can also be caused by inaccurate or faulty rotation and linear stages, and drifts in the X-ray spot position. Many tomography devices use image registration techniques to correct physical and apparent (focal spot drift) rigid body sample movements between X-ray images. More complicated motion and

deformation of samples may be impossible to correct.

In X-ray tomography, reconstruction algorithms typically assume that the rotation axis of the sample is in the middle of the X-ray images. Despite of regular calibration, these are usually not exactly aligned, which results in blurred details (artifacts are somewhat similar to those in Figure 3.16a). However, this misalignment is routinely corrected in most reconstruction software by trial and error, different center shift values are tested and the value producing the sharpest image is chosen [78].

Defective and nonlinear pixels

Image sensors may contain defective pixels, which do not respond to the light properly, and thus do not give useful information [85,86]. Dead pixels are stuck to the minimum or very low values, whereas hot pixels are stuck to the maximum or very high values. Some defective pixels may also have nonlinear responses or unusually large offset values. Single defective pixels can be corrected by detecting them and replacing the values with the mean or median value of the neighboring pixels. Some pixels may only occassionally be defective and are thus difficult to detect and correct. Nonlinear responses can be corrected by performing a procedure similar to the flat-field correction but by taking multiple images with different tube current values [87].

Defective pixels produce ring artifacts [78,88] in X-ray tomographic images (Figure 3.16b). These can be avoided by correcting the defective pixels from the X-ray images as above, by using random movement during the image acquisition or by using other correction methods. Adding a small random movement of the sample parallel to the detector plane at each angle step ensures that defective pixels are not at the same position relative to the sample in every projection. Hence, the erroneous signals spread to multiple pixels and the rings are less visible in reconstructed images. Other correction techniques often utilize the linear and concentric appearance of the rings in sinograms (i.e., projection data as a function of angle) and reconstructed images, respectively. An alternative method was also used here in the biocomposite study (see Section 5.2). A homogeneous sample made of similar material and having the same dimensions as the actual sample was imaged and processed to get an image containing only the rings. These rings were then subtracted from the actual images.

Streak artifacts

Streak artifacts (or metal artifacts) are often formed around highly attenuating particles in a much less attenuating matrix in X-ray tomography images [89]. Those are seen as more or less regular streaks radiating from the dense particles (Figure 3.16c). Streak artifacts are caused by multiple mechanisms, such as photon starvation (i.e., very low signal-to-noise ratio due to low number of photons), beam hardening, scattering, partial volume effects, undersampling, and motion. Those

can be reduced by using higher tube current values or higher photon energies, in which case the attenuation coefficients of the particles and the matrix will be closer to each other (see Figure 3.2b). There are also some correction algorithms, which try to manipulate the corrupted data to reduce the artifacts. These correction algorithms may, however, create other artifacts.

4 IMAGE-BASED MONITORING OF DEFORMATION AND WATER CONTENT

In this chapter, the method for monitoring water transport and deformation using X-ray imaging or X-ray tomography in swelling samples is introduced. Different stages of the method are illustrated in a flow chart shown in Figure 4.1. Image acquisition includes taking X-ray images of samples and also taking necessary correction X-ray images. This stage as well as strengths, weaknesses and limitations of both imaging methods, and other important considerations of imaging techniques are described in Section 4.1. The acquired X-ray images can be corrected by applying deblurring and local beam hardening correction to the images, described in Sections 4.2 and 4.3, respectively. As these correction techniques were developed after the first two applications, they were used only with the most recent ones (see Chapter 5). In the reconstruction stage, the radiographic reconstruction (Section 3.2) converts single X-ray images to two-dimensional linear attenuation coefficient images and the tomographic reconstruction (Section 3.3) converts a set of X-ray images to three-dimensional linear attenuation coefficient images. If a single image consists of multiple overlapping subimages, those are usually stitched after the reconstruction. As the image stitching was rather straightforward here (cropping and joining), it is not covered further. The flow chart illustrates the fact that the deformation analysis plays an important role in the method. The measured displacement fields are not only part of final results but also needed in the density analysis. Image normalization and deformation measurement are described in Section 4.4. Finally, Section 4.5 describes how the partial densities of solid and water are calculated from the linear attenuation coefficient images through pullback images.

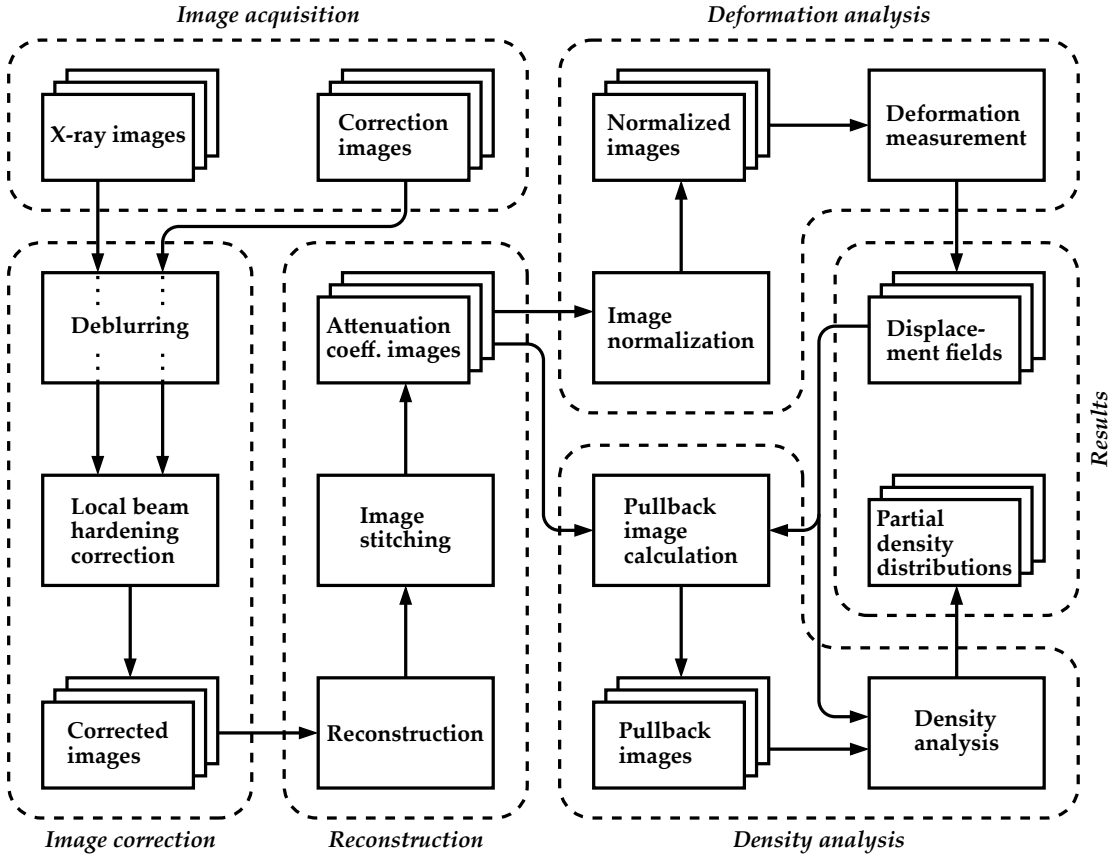

FIGURE 4.1 Flow chart of X-ray imaging and tomography method developed in this work.

4.1 Image acquisition

Both X-ray imaging and X-ray tomography can be used to monitor water transport in many materials, but in different situations. As single X-ray images can be taken in seconds, X-ray imaging is suitable for monitoring relatively fast processes. However, as X-ray images are two-dimensional projections, only one- or two-dimensional processes along the directions perpendicular to the X-ray beam can be studied properly. Radiographic reconstruction (see Section 3.2) requires knowing the thickness distribution of the sample, which can easily be calculated for samples of regular shape. Hence, X-ray imaging is most easily applicable to cases where the swelling is restricted to the beam direction (e.g., the sample is kept in a tube or between two plates). X-ray tomography can be applied to any sample geometry as it directly produces a three-dimensional image of the sample. However, the main disadvantage of X-ray tube based X-ray microtomography is the long imaging time (typically 1 h – 1 day), which limits the use to much slower processes. It should be noted that this limitation is not relevant in synchrotron based X-ray tomography, where hundreds of tomographic images can be taken in a second nowadays [90].

To monitor water transport and deformation in a sample, several images of the sample are taken during a wetting or drying process at suitable intervals. The imaging frequency is ideally matched with the rate of the processes (water transport and deformation) so that fast phenomena can be captured and unnecessary images are avoided. Although not strictly necessary, the first and last images are taken before and after the experiment. These images, together with corresponding weighings, can be used to calibrate the method. The method also needs a reference state, in which the water content distribution is known (e.g., dry state), and to which other states are compared.

The imaging settings should be chosen in such a way that the duration of a single image acquisition process is short compared to the rate of the transport process, while the image quality is good enough. The best possible resolution of the device is not necessarily needed, but the image pixel or voxel size needs to be at least a few times smaller than the smallest details (tracer particles) needed to resolve from the images. The resolution needs to be high enough that the motion of the details (displacements) can be measured with sufficient accuracy. It is also quite obvious that exactly the same imaging and reconstruction settings must be used for all the images.

4.2 Deblurring

As was already discussed in Section 3.4, X-ray images are always blurred for many reasons such as the finite size of the focal spot, X-ray scattering, light scattering and charge spreading in the image sensor. Hence, the blurring in X-ray images is a complicated process and difficult to fully correct. The blurring creates correlations between pixel values, i.e., a pixel value depends also on the values of the neighboring pixels. Slight blurring may not be an issue in conventional imaging, but when small pixel value differences need to be resolved, the blurring may cause problems. Here, the blurring was not corrected to make images sharper and to improve resolution, but to reduce the above-mentioned correlations and related systematic errors. The deblurring method was found here to be necessary only for the analysis of the sedimentation experiment (Section 5.4).

The standard way to describe image blurring is via the equation

$$I_b = I * \mathrm{PSF}\,, \tag{4.1}$$

where I_b is the blurred image, I is the unblurred image, PSF is the point spread function and $*$ denotes the two-dimensional linear convolution [91]. The PSF can be determined indirectly by first measuring the edge spread function (ESF), then calculating the line spread function (LSF), and finally reconstructing the PSF [92]. The ESF can be measured by taking an X-ray image of a straight edge of a highly attenuating plate, and thereafter calculating the transmittance profile perpendicular to the edge. As the PSF is, in general, an asymmetric function, the

ESF needs to be measured from several different angles θ. The spread functions are related as

$$\int_{-\infty}^{\infty} \mathrm{PSF}(x,y)ds = \mathrm{LSF}(t,\theta) = \frac{d}{dt}\mathrm{ESF}(t,\theta)\,, \tag{4.2}$$

where $t = x\cos\theta + y\sin\theta$ and $s = -x\sin\theta + y\cos\theta$ are the Cartesian coordinates of a rotated system of coordinates (counterclockwise rotation by angle θ). The left equality in Equation 4.2 may look familiar. It was already introduced in Figure 3.8, but with PSF $= f$ and LSF $= p$. This means that the calculation of the PSF from LSF measurements, acquired from different angles θ, is an identical inverse problem to the reconstruction in X-ray tomography, and can thus be solved using similar reconstruction techniques (see Section 3.3). However, in many cases scattering and blurring effects are circularly symmetric in the beam direction, and hence the PSF can also be assumed to be circularly symmetric and the ESF needs to be measured only at one angle. One option to calculate the PSF from the LSF is to first fit a sum of Gaussian functions

$$G(t) = \sum_{i=1}^{n} a_i \exp[-t^2/(2\sigma_i^2)] \tag{4.3}$$

to the LSF data. Then the PSF can be analytically calculated through the inverse Abel transform

$$\mathrm{PSF}(r) = -\frac{1}{\pi}\int_r^{\infty} \frac{dG}{dt}\frac{dt}{\sqrt{t^2 - r^2}} = \sum_{i=1}^{n} \frac{a_i}{\sigma_i\sqrt{2\pi}} \exp[-r^2/(2\sigma_i^2)]\,. \tag{4.4}$$

There are also many numerical methods to solve the inverse Abel transform directly from the LSF [93], but the above fitting also helps to reduce noise.

The calculation of the unblurred image from Equation 4.1 is called deconvolution and is generally not a trivial task. Deconvolution has a tendency to amplify the noise, and the direct inversion (using the convolution theorem, Equation 3.11) usually fails (result is dominated by noise) without some sort of regularization. One deconvolution technique is the Wiener filtering, which estimates the unblurred image as [91]

$$I \approx \mathcal{F}^{-1}\left\{ \frac{\overline{\mathcal{F}\{\mathrm{PSF}\}}\mathcal{F}\{I_b\}}{\overline{\mathcal{F}\{\mathrm{PSF}\}}\mathcal{F}\{\mathrm{PSF}\} + \varepsilon} \right\}, \tag{4.5}$$

where $\mathcal{F}$ and $\mathcal{F}^{-1}$ are the forward and inverse Fourier transforms, respectively, the overlines denote complex conjugates and $\varepsilon = 1/\mathrm{SNR}$. The frequency dependent signal-to-noise ratio (SNR) is not usually known, but it can be regarded as a small parameter to be tuned.

Figure 4.2 illustrates the effect of blurring in a simulated image and its correction using the Wiener filtering (Equation 4.5). The blurring mixes the transmittance values near the particles, and thus causes systematic error. The transmittance of the background is too low between the particles and the transmittance through

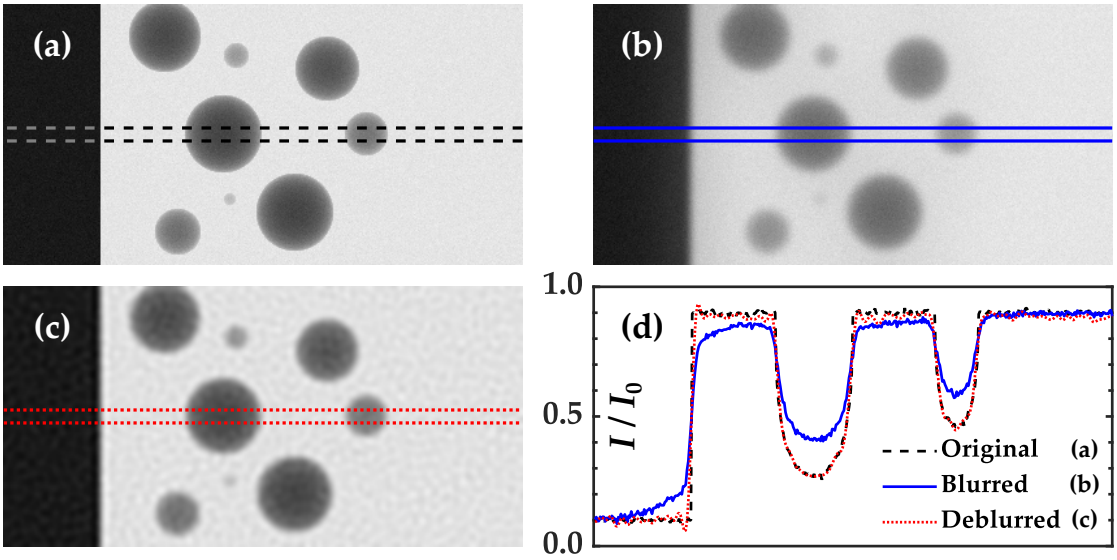

FIGURE 4.2 Blurring and deblurring. A simulated image (a) is convolved with a circularly symmetric (double Gaussian) PSF to produce a blurred image (b). An estimate for the original image, a deblurred image (c), is obtained by applying the Wiener filter (Equation 4.5) to the blurred image. Also shown are transmittance profiles across the images (d). Here the same PSF is used to blur and deblur the images, which is perhaps an inversion crime, but is used for illustrative purposes only.

the particles is too high. In this example, the deblurred image is very close to the original image due to the same PSF used to blur and deblur. Even in such a case, the original image cannot be fully restored due to noise. In general, deconvolution is very sensitive to errors in the PSF, which in turn is difficult to measure accurately as it is affected by noise, can be asymmetric and may depend on position and time.

4.3 Local beam hardening correction

The effect of beam hardening needs to be corrected to enable quantitative density analysis based on X-ray images or X-ray tomographic images. The standard beam hardening correction (Equation 3.16) may be adequate in many cases but to take spatial and temporal variations of beam hardening into account and improve accuracy, local beam hardening correction was developed. It is similar to the standard beam hardening correction, but the coefficients are measured and the correction is applied locally. Although the local beam hardening correction was here used only in X-ray imaging (Sections 5.3 and 5.4), it can be used in X-ray tomography as well.

The local beam hardening correction is based on the standard polynomial beam hardening correction (Equation 3.16), where the corrected transmittance, assumed

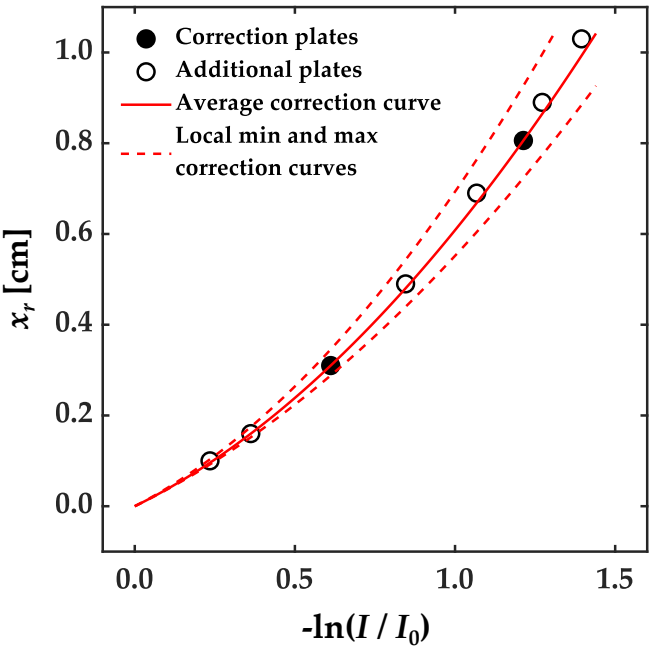

FIGURE 4.3 Local beam hardening correction. The correction curve (Equation 4.6) is fitted to the two data points obtained from the aluminum correction plates (averages over the entire images). Also shown are data points from additional aluminum plates and the most deviating local correction curves (without data points). Adapted from [P3] under the license CC BY 4.0.

to obey the Beer-Lambert law (Equation 3.1), is replaced with the transmittance of a homogeneous reference material of linear attenuation coefficient μ_r and thickness x_r. This yields the local beam hardening correction in the form

$$x_r = A_1' \cdot \ln\left(\frac{I}{I_0}\right) + A_2' \cdot \ln^2\left(\frac{I}{I_0}\right), \tag{4.6}$$

where $A_1' = -A_1/\mu_r$ and $A_2' = -A_2/\mu_r$. In this form, the measured transmittance I/I_0 is converted into the equivalent thickness of the reference material x_r instead of the corrected transmittance. This is useful since x_r can be used in further analysis with minimal modifications to equations and there is no need to choose a value for μ_r. The coefficients A_1' and A_2' can be determined by measuring the transmittance through homogeneous plates of uniform thickness made of the reference material. At least two plates of different thickness are needed to solve the two coefficients. The plates have to cover at least that part of the field of view that needs to be corrected. Two simultaneous equations can then be formed using Equation 4.6, which are solved for each pixel separately. As the degree of beam hardening usually varies slowly across X-ray images, it may be better to solve the coefficients in averaged subimages of $n \times n$ pixels (e.g., 10×10 pixels), and thereafter interpolate the coefficients to each pixel in order to reduce noise.

Figure 4.3 shows exemplar data from aluminum correction plates and the fitted correction curve. The curve closely follows the additional data points indicating

that the quadratic fit is sufficient in this case. The most deviating local curves illustrate how much the beam hardening varies locally in the image. If beam hardening also has temporal variations, X-ray images of correction plates need to be taken at regular intervals. For higher atomic number materials the effect of beam hardening is generally stronger and the quadratic polynomial may not be sufficient. In such a case, a higher order of polynomial with the corresponding number of correction plates can be used. Although the local beam hardening correction is intended to correct the effect of beam hardening and its variations, it corrects possible nonlinearities and variations arising from the detector as well.

If the local beam hardening correction is used in X-ray imaging, it is more convenient to use relative attenuation coefficients ($\mu' = \mu/\mu_r$) instead of absolute coefficients and calculate the radiographic reconstruction using the form

$$\mu'_s x_s + \int_{C_0} \mu' dx = x_r \tag{4.7}$$

instead of Equation 3.7. If the local beam hardening correction is used with X-ray tomography (was not used in this thesis), it is more straightforward to use the equivalent thickness of the reference material x_r as input data for the reconstruction software instead of the dimensionless projections

$$p = \int_C \mu dx = -\ln\left(\frac{I}{I_0}\right)_c = \mu_r x_r \,. \tag{4.8}$$

The result of the reconstruction will be then μ/μ_r instead of μ. As the unit of μ is usually 1/px and that of x_r is, e.g., cm, the unit of μ/μ_r will be cm/px, which is actually the pixel size. Hence, by dividing the result by the pixel size gives the dimensionless relative attenuation coefficient ($\mu/\mu_r = 1$ for the reference material). If the reconstruction software accepts only transmittance images $(I/I_0)_c$, a value for μ_r needs to be chosen.

4.4 Deformation measurement

The deformation of solid material is not only measured because it yields useful data on mechanical behavior but it is also needed in the density analysis (see Section 4.5). The deformation can be measured by applying digital image correlation techniques between the reference and deformed state images. Any algorithm that is capable of measuring the displacement field between the images can be used. In the applications of this thesis, a relatively simple block matching algorithm was found to be sufficient.

Block matching algorithm

The block matching algorithm is best suited to cases where the displacement gradients ($\partial u_i/\partial x_j \approx 0$) are small, i.e., the deformation corresponds approximately

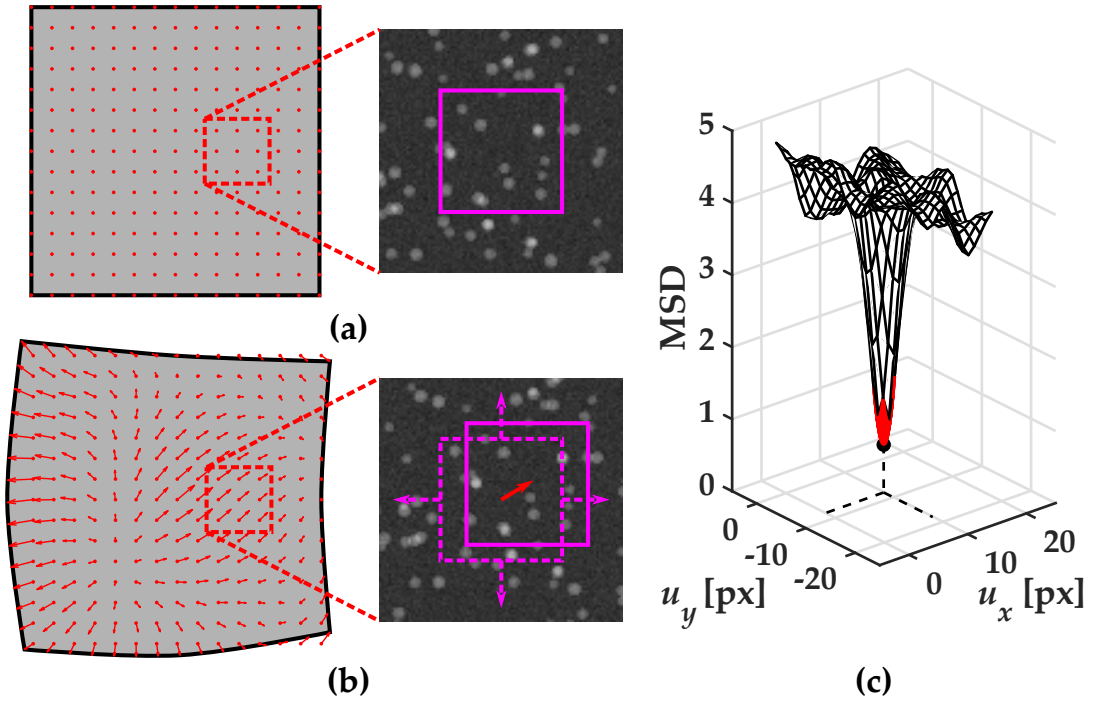

FIGURE 4.4 Block matching algorithm. A rectangular block (solid rectangle) is extracted from the reference state image (a), and the best matching block (solid rectangle) is searched from the deformed state image (b). The minimum of the MSD gives the displacement at this grid point (c). A quadratic fit (red mesh) to the minimum gives the displacement with subpixel accuracy.

to pure translation and there are no significant rotations or local deformations. The basic principle of the block matching algorithm is illustrated in two dimensions, the extension to three dimensions is straightforward. First, a rectangular grid of points is formed to cover the whole sample in the reference state image (Figure 4.4). In each grid point, a rectangular block B_{ref} (i.e., a subimage of $m \times n$ pixels centered at the grid point) is extracted from the reference state image. The best matching block B_{def} is then searched from the deformed state image by extracting similar-sized subimages around the grid point in each direction pixel by pixel. Common measures for the similarity are the sum of squared differences

$$\mathrm{SSD}(x, y, u_x, u_y) = \sum_{i=1}^{m} \sum_{j=1}^{n} [B_{\mathrm{def},ij}(x + u_x, y + u_y) - B_{\mathrm{ref},ij}(x, y)]^2 , \qquad (4.9)$$

or the mean of squared differences MSD = SSD / $(m \cdot n)$, the normalized cross-correlation and the phase correlation [94, 95]. In the applications of this thesis, the SSD or the MSD was used[1]. The minimum of the SSD gives an estimate for the displacement with an accuracy of one pixel. Subpixel accuracy is achieved

[1] The advantage of the MSD over the SSD is only cosmetic, the MSD produces nice small numbers that do not depend on the block size. However, the matching will give the same result, no matter which one is used.

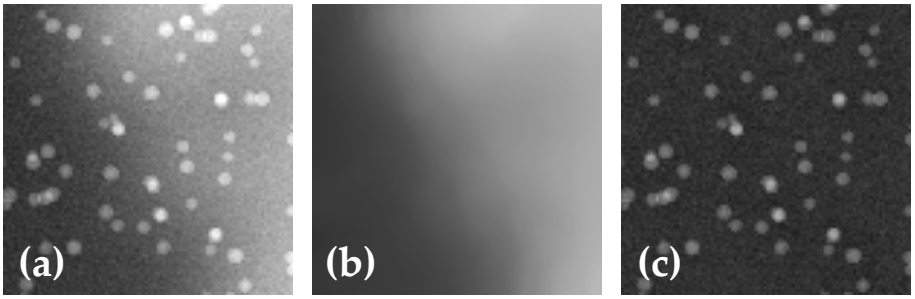

FIGURE 4.5 Image normalization. The original (a), background (b) and background-removed (or normalized) image (c).

by fitting a quadratic function (SSD = $a_0 + a_1(u_x - u_{x0})^2 + a_2(u_y - u_{y0})^2$) to the minimum locally, and then using $\vec{u} = (u_{x0}, u_{y0})$ as a more accurate estimate for the displacement. Other methods such as Gaussian fitting and a centroid method can also be used to find the location of the minimum [96].

A suitable grid point spacing and block size depend, e.g., on tracer particle density and size, local deformations and desired spatial resolution. The block size is good to be at least the distance of the grid points so that the entire image data can be utilized. A larger block size, to a certain point, improves the correlation and yields smoother results. The search ranges $u_x \in [u_{x1}, u_{x2}] \cap \mathbb{Z}$ and $u_y \in [u_{y1}, u_{y2}] \cap \mathbb{Z}$ should be wide enough so that the real displacements fall into those ranges and can thus be found. Optimal settings for each case are found by testing different values.

Image normalization

The correlation between the blocks ideally arises from the details that follow the motion of the solid material (natural details or added tracer particles). However, as water is transported and the sample locally deforms, the resulting image gradients may lead to false correlations. To avoid this, the images should be normalized in a simple way shown in Figure 4.5. The original image (Figure 4.5a) is first filtered (e.g., median filter with a suitable radius) such that the details disappear and only the background is visible (Figure 4.5b). This background is then removed by subtracting it from the original image for additive quantities (linear attenuation coefficient and equivalent thickness) or by dividing the original image by the background for multiplicative quantities (transmittance).

Extending block matching to large deformations

As previously mentioned, the block matching algorithm works well when the local deformation at block scale corresponds to pure translation. This may not always be the case, significant shrinking or swelling can occur in some materials. In such a case, the correlation between the reference and deformed state blocks may become too low at later times, which leads to inaccurate or failed deformation measurement. Another option is to measure the deformation between consecutive

images and sum the measured displacements to get the total displacement. If the sample has been imaged frequently, the deformation may be small and the correlation high between consecutive images. However, this approach seems to produce large cumulative error as small error is associated with each measurement. It may well be that the best strategy is something between the methods described above. This can be implemented by updating the reference block with a new one, from the deformed state image, only when the correlation becomes too low. The minimum value of the MSD can be used to monitor the goodness of match. It is zero for the perfect match, but for fully uncorrelated blocks ($\langle B_1 B_2 \rangle_0 = \langle B_1 \rangle \langle B_2 \rangle$) the expected value is

$$\langle \mathrm{MSD} \rangle_0 = \langle (B_{\mathrm{def}} - B_{\mathrm{ref}})^2 \rangle_0 = \langle B_{\mathrm{ref}}^2 \rangle + \langle B_{\mathrm{def}}^2 \rangle - 2 \langle B_{\mathrm{ref}} \rangle \langle B_{\mathrm{def}} \rangle \,. \tag{4.10}$$

The reference block is updated when the condition

$$\frac{\min(\mathrm{MSD})}{\langle \mathrm{MSD} \rangle_0} > k \tag{4.11}$$

is met. The main challenge here is the determination of the parameter $k \in [0, 1]$. This parameter is likely very case-specific, and hence the best option is to test different values of k and compare the results (e.g., water content distribution) with validation data. In general, non-optimal values of k seem to produce noisier results compared to the optimal value, and hence the smoothness of the results can also be utilized to determine a suitable value of k.

Errors in deformation measurement

The calculated dry density and water content values are very sensitive to errors in the deformation measurement (see Section 4.5), and hence the deformation needs to be measured very accurately. There are several possible sources of errors that affect the accuracy of the deformation measurement. It is possible that some parts of the sample do not contain enough details resulting in clearly wrong displacements in those areas. Some particles may lag or get stuck at the interface between the sample and the fixed wall. Spurious movement of particles may occur near large pores. Single erroneous displacements can usually be replaced with the mean or median values of the neighboring displacements.

The edges of the sample are also problematic, since there the blocks extend partially outside the sample, and thus fewer pixels are effectively available for the correlation. Fixed details outside the sample may also create false correlations near the edges. This can be avoided by setting the pixel values outside the sample to the background value. In some cases, the displacement at the edge can be measured more accurately by using some edge detection technique.

One source of error affecting the accuracy of deformation measurement is related to sampling. Tracer particles and many natural details are more or less randomly distributed in samples. A limited number of particles, even though completely randomly distributed, show particle density variations between different blocks

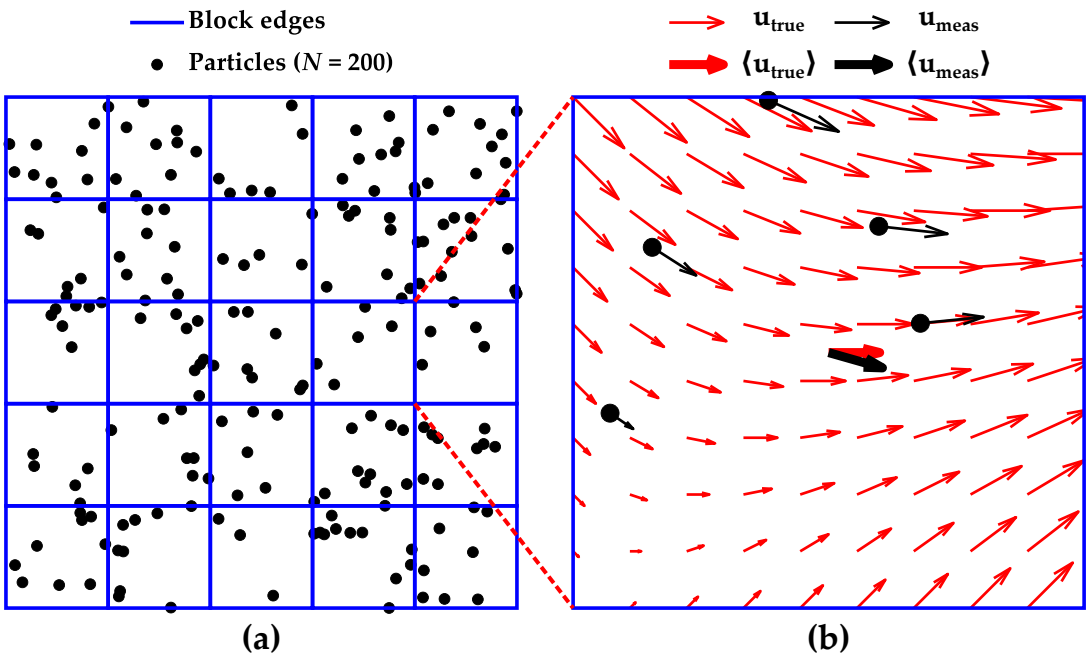

FIGURE 4.6 Sampling error in block matching. The number of particles in each block varies despite random positions (a). The low number of particles unevenly distributed in a block may lead to errors in analysis of displacement (b).

(Figure 4.6a). As the displacement of a block is effectively determined by the average displacement of the individual particles it contains, a small number of unevenly distributed particles in the block together with non-trivial deformation is prone to cause sampling error (Figure 4.6b). The error may be further increased if some of those particles do not properly follow the motion of solid material. The sampling error can be reduced by increasing the number of tracer particles (if tracer particles are used), but too high number of particles may hamper image analysis and affect material and transport properties.

4.5 Density analysis

Density analysis is based on the assumption that the sample consists of only two material components, solid and water, whose elemental compositions are homogeneous across the sample, but their partial densities may vary locally. Air and other gases can be ignored due to their low density and attenuation ($\mu_{\text{air}} \approx \mu_{\text{water}}/1000$). The mixture rule (Equation 3.3) is assumed to hold after the effect of beam hardening is corrected, and hence the linear attenuation coefficient in the sample can be written as

$$\mu_s = c_d \cdot \rho_d + c_w \cdot \rho_w \,, \tag{4.12}$$

where c_d and c_w are the mass attenuation coefficients and ρ_d and ρ_w are the partial densities of solid and water, respectively. If the local beam hardening correction (Equation 4.6) is used, Equation 4.12 can be divided by the linear attenuation coefficient of the reference material μ_r and the coefficients $\mu'_s = \mu_s/\mu_r$, $c'_d = c_d/\mu_r$ and $c'_w = c_w/\mu_r$ can be used instead of μ_s, c_d and c_w.

As was discussed in Section 3.3, the result of the X-ray tomographic reconstruction is the linear attenuation coefficient distribution and is often stored as such (floating point image formats) and can thus be directly used in the further analysis. If the values have been linearly mapped to grayscale values (unsigned integer image formats, Equation 3.15) or other special units are used (e.g., Hounsfield units), those should be first converted back to linear attenuation coefficients. However, such a conversion is not necessarily needed, a general linear function

$$g_s = \alpha_0 + \alpha_d \cdot \rho_d + \alpha_w \cdot \rho_w \tag{4.13}$$

between grayscale values g_s and densities ρ_d and ρ_w may be used instead of Equation 4.12.

Density calibration

The mass attenuation coefficients in Equation 4.12 can be determined if there are at least two calibration points (three if Equation 4.13 is used and α_0 is not readily known). These calibration points can be, e.g., the average values of ρ_d, ρ_w and μ_s of the entire sample in the initial and final states. The known average values in intermediate states, and larger areas of air or liquid water visible in the images may provide additional data points for fitting. Another option is to use data from different samples, where the average values of ρ_d and ρ_w vary. These samples can be actual test samples or specially made calibration samples, provided that the elemental compositions of solid and water do not vary between the samples.

Although the mixture rule (Equation 3.3) suggests that Equation 4.12 is linear, the polynomial beam hardening correction is not perfect, and hence the actual dependence may be slightly nonlinear. This is, however, not a problem if the dependence can be assumed to be locally linear within the density space encountered in the experiments. This requires local calibration points and adding the offset term in Equation 4.12. In principle, a nonlinear fit function could also be used, but finding the correct form and fitting may require an extensive set of calibration points.

Partial density distributions

By combining the definition of water content (Equation 2.1) and Equation 4.12, the partial density distribution of solid in the reference state can be calculated as

$$\rho_{d,\mathrm{ref}} = \frac{\mu_{s,\mathrm{ref}}}{c_d + w_{\mathrm{ref}} \cdot c_w}, \tag{4.14}$$

if the water content distribution in the reference state (w_{ref}) is known. The easiest choice for the reference state is the dry state (usually initial or final state) because

then $w_{\text{ref}} = 0$. In some cases, the sample may not be completely dry in its initial state, but the residual water content distribution can be assumed to be constant. This assumption is usually valid if the sample is made of carefully mixed material prior to experiments (e.g., mixing bentonite powder before compaction) or the sample have been kept in the same environmental conditions for a long period of time. It is also possible to use the fully saturated state as a reference state (see Equations 4.17 and 4.18).

The measured deformation is used to calculate the partial density distribution of solid in the deformed state as

$$\rho_d = \frac{\rho_{d,\text{ref}}}{1 + \nabla \cdot \vec{u}}, \tag{4.15}$$

where $\vec{u}$ is the displacement between the reference and deformed state and $\nabla \cdot \vec{u}$ is the relative volume change, which can be evaluated from the measured displacement field using, e.g., finite differences or local polynomial fitting.

As the partial density distribution of solid is now known in each state, Equation 4.12 gives the partial density distribution of water in the deformed state as

$$\rho_w = \frac{\hat{\mu}_s - c_d \cdot \rho_d}{c_w}, \tag{4.16}$$

where $\hat{\mu}_s(\vec{x}) = \mu_s(\vec{x} + \vec{u})$ is the pullback image of $\mu_s(\vec{x})$, i.e., the deformed state image given in material coordinates. Pullback images thus ensure that the material points (here pixels or voxels) between the reference and deformed state images correspond each other.

Saturation assumption

If the sample is fully saturated (i.e., all the pores are filled with water), the partial density of water (saturation limit) is given by

$$\rho_{w,\text{sat}} = \rho_w^* \cdot \left(1 - \frac{\rho_d}{\rho_d^*}\right), \tag{4.17}$$

where ρ_d^* and ρ_w^* are the intrinsic densities of solid and water. The former is also called grain density in soil sciences. Equation 4.17 is not necessarily fully accurate for all materials, since the density of tightly bound water can be greater than $1.0\,\text{g/cm}^3$ [97]. However, it can be assumed to hold relatively well if the proportion of bound water is small compared to free water.

It may be useful to compare the measured partial density of water (Equation 4.16) with the saturation limit (Equation 4.17) or calculate the degree of saturation $s = \rho_w / \rho_{w,\text{sat}}$ to see where the sample is saturated and to check that the method gives reasonable results ($s \approx 1$ in the areas where the sample is presumably saturated).

If the sample can be assumed to be fully saturated, the partial densities of solid and water can be calculated without deformation measurement. By combining

Equations 4.12 and 4.17 ($\rho_w = \rho_{w,\mathrm{sat}}$), the partial density distribution of solid can be calculated as

$$\rho_d = \frac{\mu_s - c_w \cdot \rho_w^*}{c_d - c_w \cdot \rho_w^* / \rho_d^*}\,, \tag{4.18}$$

and the partial density distribution of water is then given by the saturation limit (Equation 4.17).

About errors

As the main results, the partial density distributions of solid and water, are calculated using Equations 4.14–4.18, those are subject to several different sources of errors. These sources can be divided into three different categories.

1. **Image error** is caused by different image artifacts (beam hardening, blurring, noise, etc.) and their incomplete correction.
2. **Calibration error** occurs if the data used in the density calibration are erroneous or incorrect values of ρ_w^* and ρ_d^* are used.
3. **Deformation error** arises from the insufficient data (sampling error) and from the deformation algorithm itself.

It is, however, difficult to estimate the contribution of each source of error to the total error, and the magnitude of the total error in general. They likely depend on many factors such as the imaging device and settings, sample materials, deformation measurement algorithm and many other details in the method.

The deformation measurement is possibly the weakest link of the method in the applications of this thesis (apart from the sedimentation experiment, where the deformation was not needed, Section 5.4). The deformation was measured relatively well in all cases, but even small errors in the measured displacements lead to relatively large errors in the relative volume change values ($\nabla \cdot \vec{u}$), and further to the partial densities of solid in the deformed state. If the images and the calibration do not contain errors, it is evident from Equation 4.12 that error in ρ_d propagates to ρ_w as

$$\Delta\rho_w = -\frac{c_d}{c_w} \cdot \Delta\rho_d\,. \tag{4.19}$$

Due to the minus sign, the errors in the partial densities of solid and water point in the opposite directions, which amplifies the error in the water content values. Also, a high mass attenuation coefficient ratio may amplify the error. For the materials and imaging settings in this thesis, this ratio is $c_d/c_w \approx 2$ for bentonite and water, and $c_d/c_w \approx 1$ for biocomposite and water.

To get some idea of the accuracy of the method in the applications of this thesis, one may observe the comparisons of results with validation data in Figures 5.4 and 5.12.

5 APPLICATIONS

5.1 Constant volume wetting of bentonite

In this application, X-ray tomography was used to monitor water transport and induced internal deformations in small-scale bentonite samples kept in a constant volume. The main objective was to produce data for hydro-mechanical modeling of the bentonite buffer used in nuclear waste repositories. See Publication P1 for more details on this application.

Experimental setup and samples

Cylindrical bentonite samples of diameter 17 mm and height 10 mm were confined to a constant volume in a sample holder shown in Figure 5.1. The samples were wetted with synthetic groundwater (Allard-pH-7) from the bottom end through a filter disc of diameter 6 mm or 15 mm. A block above the sample included a filter disc and a channel for releasing pore air. The axial swelling stress was measured using the force sensor assembled in the top part of the sample chamber. The bentonite powder used (MP Biomedicals bentonite) was very fine-grained, and thus hollow glass microspheres ($d \approx 100\,\mu m$) were mixed with the powder to act as tracer particles for the deformation measurement. The samples were uniaxially compacted to two different dry densities ($1.2\,g/cm^3$ or $1.5\,g/cm^3$).

Imaging procedure

X-ray tomographic scans were performed with a SkyScan 1172 microtomography device (see Figure 3.11). In each scan, 554 X-ray images (360° scan), covering a field of view[1] of around 24 mm × 13 mm with a pixel size of 24 µm, were acquired using an exposure time of 10 × 316 ms. The tube voltage was 100 kV, the tube

[1] In this thesis, image and grid sizes are given as width × height (x, y) or width × height × depth (x, y, z). In both cases, the last dimension corresponds to the vertical direction.

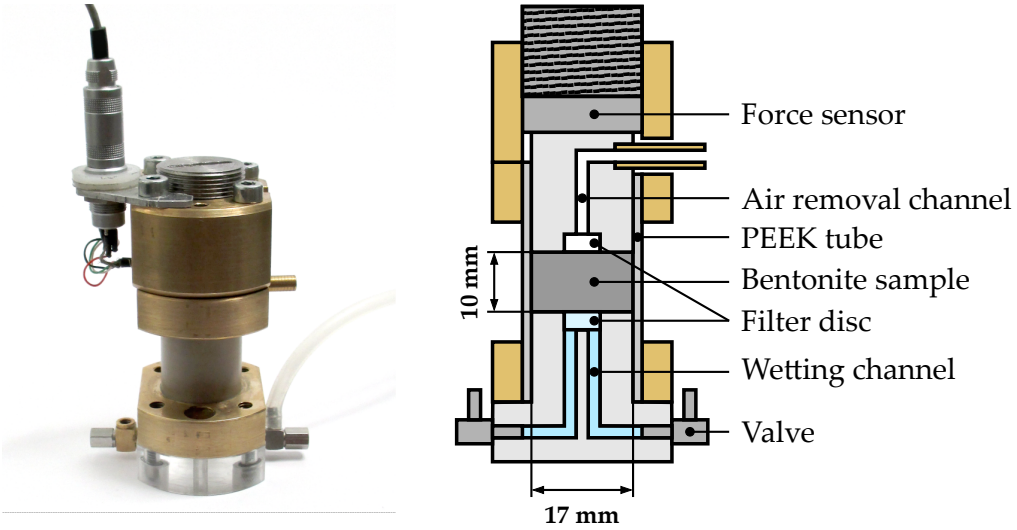

FIGURE 5.1 Photograph (left) and schematic cross-sectional view (right) of sample holder used in constant volume wetting experiments. Adapted with permission from [P1] Copyright © 2015 Elsevier B.V.

current was 80–100 µA and the lower part of the spectrum was cut with 0.5 mm thick aluminum and 0.04 mm thick copper filters. The total scanning time was around 45 min. The projections were reconstructed using the standard beam hardening correction and the filtered back projection algorithm implemented in NRecon software by SkyScan. The reconstruction resulted in tomographic images of size 1000 × 1000 × 524 voxels with a voxel size of 24 µm. Examples of such images of a bentonite sample in a sample holder tube are shown in Figure 5.2. The added tracer particles can be seen as dark spots (lighter than bentonite) in the sample.

Each sample was first scanned in the reference state before wetting, and thereafter

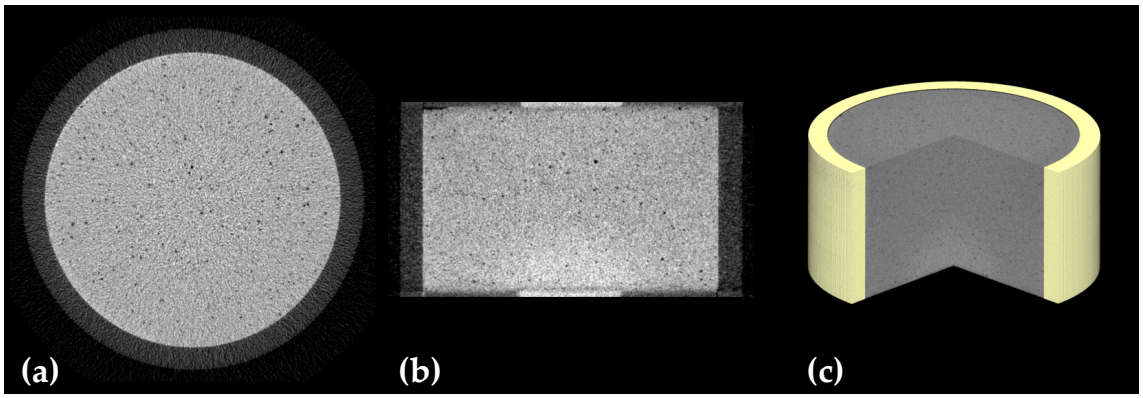

FIGURE 5.2 Examples of X-ray tomographic images of bentonite sample. An axial slice (a), a vertical slice (b) and a three-dimensional visualization (c) of a bentonite sample.

around 10 times until the sample was fully saturated with water. This took 1–2 weeks depending on the size of the filter disc, through which the sample was wetted. The mass of absorbed water was also monitored by weighing the whole sample holder before and after each scan.

Deformation and density analysis

The deformation between the reference state (initial state) and each deformed state was measured using a three-dimensional block matching algorithm from normalized images (downscaled to $425 \times 425 \times 235$ voxels). The displacements were calculated in a rectangular grid of $31 \times 31 \times 19$ points using a grid spacing of 12 voxels. The comparison and search radii were 20 voxels and 5 voxels, respectively. However, not all the analyzes used exactly the settings above. The measured displacement fields were used to calculate the pullback images and the relative density change in each deformed state.

Linear dependence between the partial densities of bentonite and water and the grayscale values of X-ray tomographic images was assumed, and hence Equation 4.13 was fitted to the average values of ρ_b, ρ_w and g of around 10 samples (around 100 data points). The partial density distribution of bentonite in the reference state ($\rho_{b,\mathrm{ref}}$) was first calculated from the initial state image by using such a fit and a predetermined (oven drying bentonite powder at 105 °C) constant value for the initial water content (Equation 4.14). The partial density distributions of bentonite and water in the wetted and deformed states were calculated using Equations 4.15 and 4.16.

The deformation measurement was validated by compressing a silicone rubber sample in a material testing stage, with a similar dimensions and amount of glass microspheres than what was used for the bentonite samples (Figure 5.3). The no-slip boundary condition at both ends led to the barrel-shaped sample after an applied axial displacement of 0.35 mm. The measured displacement field was compared to a numerical solution obtained by COMSOL (assuming incompressible and linear elastic material). The results seem to be very similar but somewhat differ near the ends of the sample. The differences are possibly caused by larger displacement gradients near the ends or by the blocks that partially extend outside the sample.

The density analysis was validated by performing a wetting experiment similar to the actual experiments, but interrupting the experiment at an intermediate state after around one day so that there was a non-trivial water content distribution. The sample was cut into 10 slices and the water content in the slices was determined by oven drying at 105 °C. Figure 5.4 shows the water content profiles in the axial direction, measured from the cut slices and using the X-ray tomographic method. The results are very similar in the middle part but differ near the ends, likely due to the cone beam artifact and the unreliable deformation measurement near the ends as discussed above. Also shown is the water content profile measured with

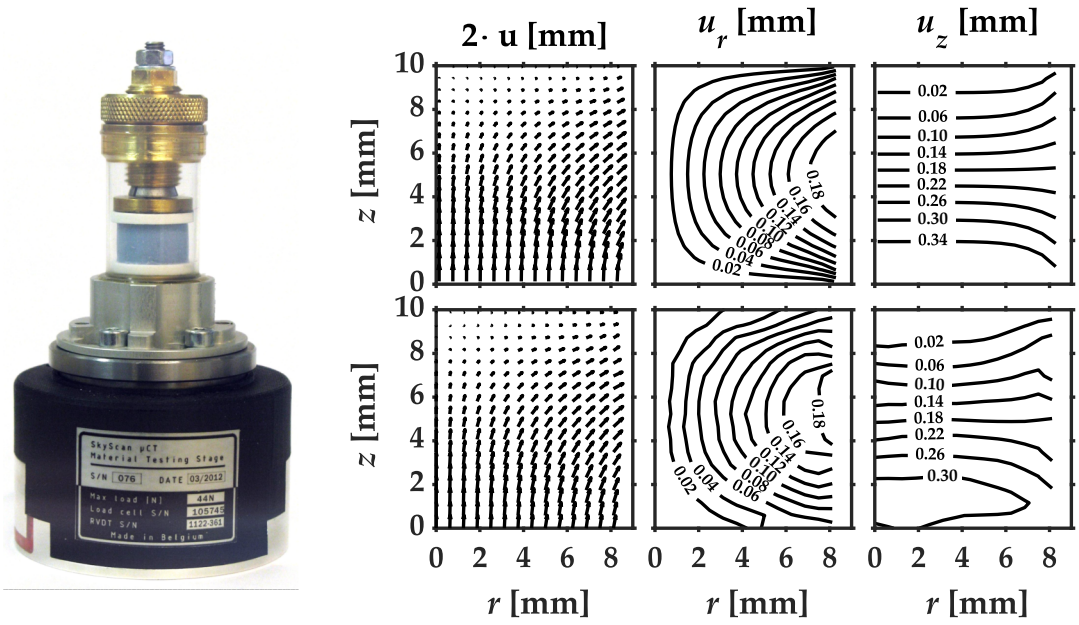

FIGURE 5.3 Validation of deformation measurement. A silicon rubber sample (d = 17 mm, h = 10 mm) was slightly compressed in a material testing stage (photograph on left). The top and bottom rows show the numerical solution and the measured displacements, respectively. Adapted with permission from [P1] Copyright © 2015 Elsevier B.V.

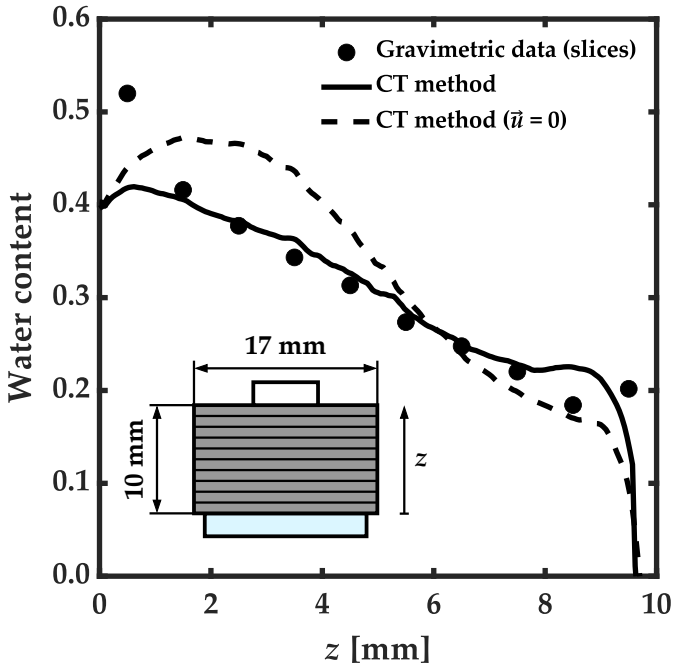

FIGURE 5.4 Validation of density analysis. A bentonite sample was wetted from one end (z = 0 mm) for one day and then sliced to obtain the gravimetric validation data. The results given by the X-ray tomographic (CT) method are shown with and without ($\vec{u} = 0$) deformations. Adapted with permission from [P1] Copyright © 2015 Elsevier B.V.

the X-ray tomographic method, but ignoring the deformation ($\vec{u} = 0$). In this case, the result differs also in the middle parts of the sample. This illustrates how essential the deformation measurement is for a swelling material even in constant volume conditions.

Results

Examples of results, azimuthally averaged water content distributions and displacement fields of two different wetting geometries at four different instants of time, are shown in Figure 5.5. The water content distributions look qualitatively plausible and resemble a diffusion-like process. The time evolution of the displacement field is complicated during the wetting process. The method thus produces detailed data on rather complex hydro-mechanical behavior of bentonite, which is useful for model development and validation.

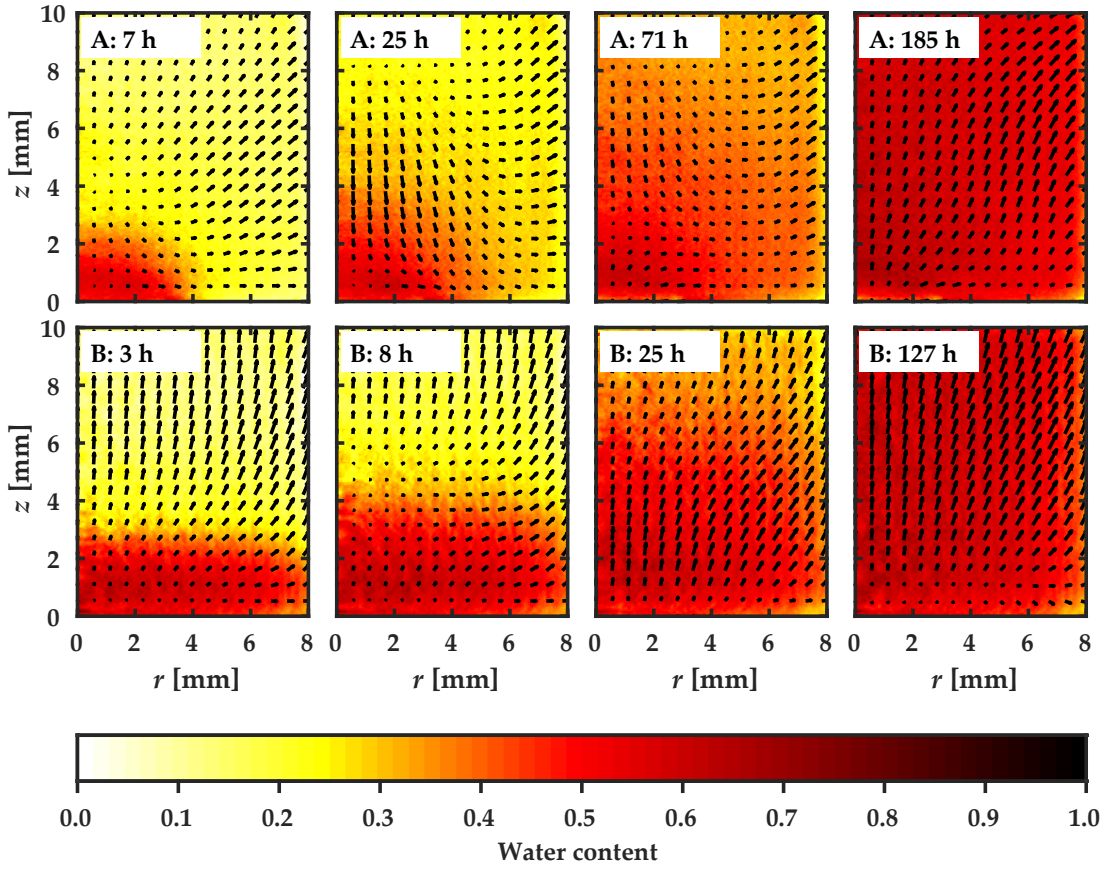

FIGURE 5.5 Azimuthally averaged water content distributions and displacement fields for two samples at four instants of time. Sample A (top row) and B (bottom row) were wetted through filter discs of diameter 6 mm and 15 mm, respectively. The dry density of both samples was 1.2 g/cm^3. The displacements are scaled by a factor of 5. Adapted with permission from [P1] Copyright © 2015 Elsevier B.V.

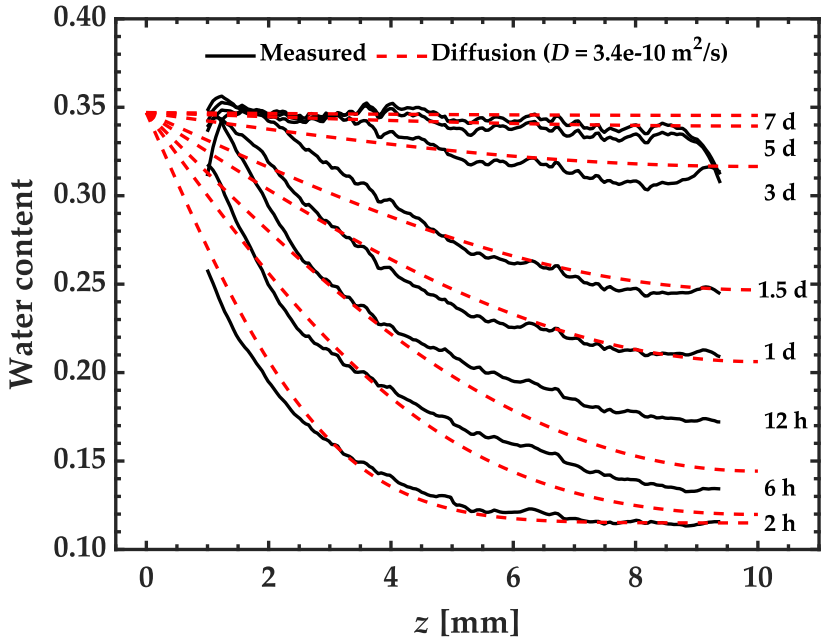

FIGURE 5.6 Comparison between measured water content profiles and linear diffusion for MX-80 bentonite.

The method was further successfully applied to similar-sized MX-80 bentonite samples [98], and the results were used to validate a hydro-mechanical model [99]. Figure 5.6 shows the measured one-dimensional water content profiles for an MX-80 bentonite sample (dry density 1.5 g/cm^3) from that study. Also shown are fitted linear diffusion profiles (Equation 2.8). The water transport clearly resembles more linear diffusion than unsaturated flow (compare to Figure 2.4), and hence it seems that diffusion is the dominant water transport mechanism in MX-80 bentonite in these conditions. However, as the measured water content profiles somewhat deviate from the ideal profiles, it is possible that the diffusion is slightly nonlinear, there are multiple diffusion processes or water is also transported to a lesser extent by flow.

5.2 Water transport in composite material

X-ray tomography was used to monitor water transport in a biocomposite material consisting of a polylactic acid (PLA) matrix and birch pulp fibers as reinforcement. This was a preliminary study where the applicability of the method to this type of material was tested. See Publication P2 for more details on this application.

Experimental setup and procedure

The experimental setup is shown in Figure 5.7. A cylindrical sample of diameter 2 mm and height 4 mm was cut and milled from a tensile test specimen made of

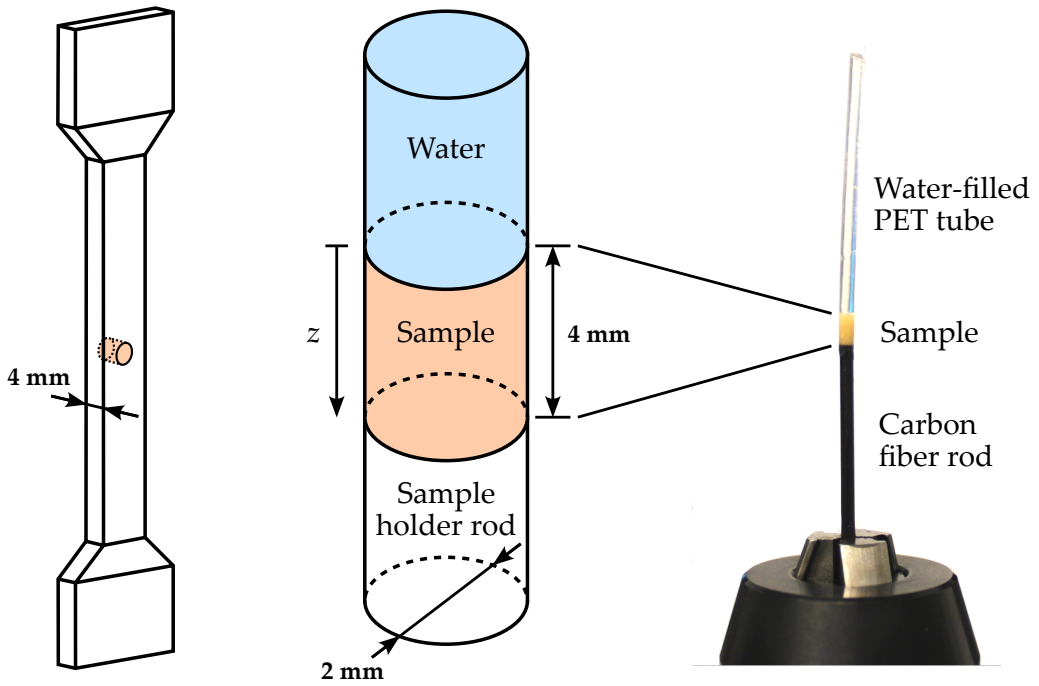

FIGURE 5.7 Experimental setup of wetting experiment for composite material. Adapted from [P2] under the license CC BY 3.0.

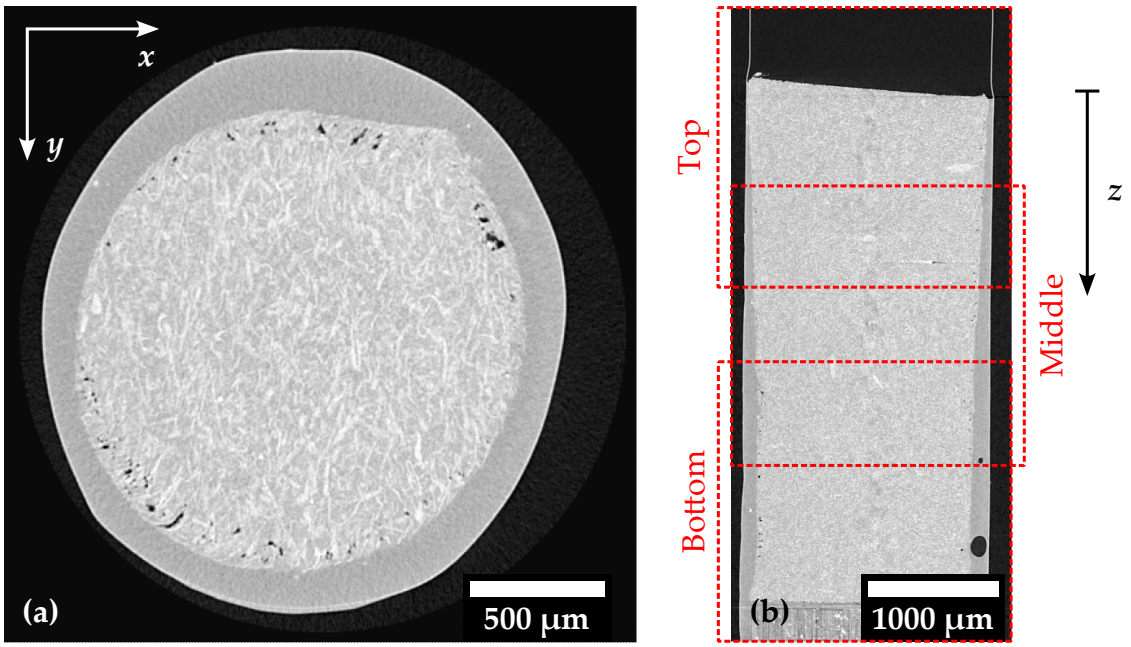

FIGURE 5.8 Examples of X-ray tomographic images of composite sample. An axial (a) and a vertical (b) slice (also showing the subscan areas) of a tomographic image. Adapted from [P2] under the license CC BY 3.0.

the composite material described above. The sample was placed and glued into a polyethylene terephthalate (PET) tube, which in turn was glued to a carbon fiber rod. The sample was first dried in the oven at 50 °C for 24 h. After that, the sample was imaged with an Xradia MicroXCT-400 microtomography device (see Figure 3.11) by taking 1129 X-ray images (180° scan) of 2.2 mm × 2.2 mm field of view with a voxel size of 4.7 µm. The tube voltage was 30 kV, the tube current was 100 µA and no X-ray filters were used. As the sample did not completely fit in the field of view in the vertical direction, three vertically overlapping subscans were acquired totaling 3 × 3.5 h = 10.5 h scan time. The size of a stitched tomographic image was around 500 × 500 × 1000 voxels. After acquiring the dry state image, wetting was started by adding water into the PET tube on the top of the sample. The sample was imaged 24 times during the 135-day long experiment. The interval between the images varied from 12 h to 1 week from the beginning to the end of the experiment. Figure 5.8 shows examples of X-ray tomographic images obtained from the composite sample.

Analysis

The acquired X-ray images were reconstructed using the standard beam hardening correction and the filtered back projection algorithm implemented in XMreconstruction software by Xradia. Some residual ring artifacts were visible in the reconstructed images. These were corrected by first imaging a homogeneous poly(methyl methacrylate) (PMMA) rod with the same settings as in the actual experiments. This resulted in an image where the rings were readily visible, which was then used to remove their contribution from the actual images. The mass attenuation coefficients were calculated using the densities and the average linear attenuation coefficients of the dry sample and the water layer above the sample. The average density of the composite sample was measured gravimetrically. The deformation was measured using a three-dimensional block matching algorithm, for which the fibers provided the necessary details in the sample. The displacements were calculated using a rectangular grid of 40 × 40 × 80 points with a spacing of around 12 voxels. The comparison radius was 5 voxels, and the search radius was 8 voxels in the xy-direction and 15 voxels in the z-direction (axial direction).

Results

As the wetting geometry was effectively one-dimensional in the axial direction, the results were averaged to one-dimensional profiles along the axial direction (Figure 5.9). The results seem qualitatively plausible, and the water transport somewhat resembles diffusion as no visible wetting front is seen (compare to Figure 2.4). However, the results may have been affected by water evaporation through the sides and the bottom end of the sample, since most polymers are permeable to water [100]. Better sealing is thus needed if similar experiments will be conducted in the future. Some profiles show peculiar behavior near the center of the sample.

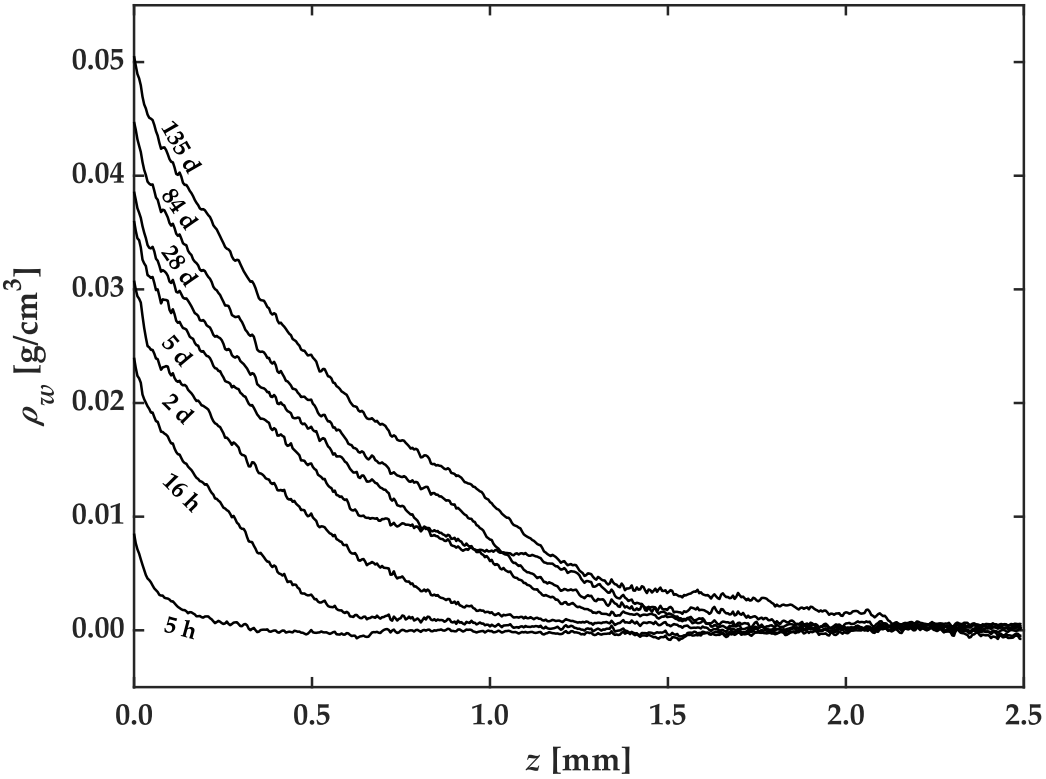

FIGURE 5.9 Partial density profiles of water along axial direction in composite sample at selected instants of time. Adapted from [P2] under the license CC BY 3.0.

It is not known whether this is a real phenomenon or just a measurement error. Although no proper validation was possible to perform for such a small sample used here, based on the consistent partial density profiles of water, the method was successfully applied to the composite material in this preliminary study.

5.3 Swelling of bentonite in tube

There are concerns that bentonite may slowly erode away from a nuclear waste repository through groundwater filled fractures in the bedrock, especially in low salinity conditions (e.g., after glacial periods) [101]. Here, the initial stage of such erosion, swelling of compacted bentonite into a fracture, was studied. As the initial swelling of bentonite turned out to be relatively fast, the process was monitored using X-ray imaging instead of X-ray tomography. See Publication P3 for more details on this application.

Experimental setup and samples

Figure 5.10 shows a sample holder used in the experiments. A fracture in the bedrock was replaced with a vertical aluminum tube, which was partly filled with compacted bentonite (MX-80). The bottom end was fixed while the top end

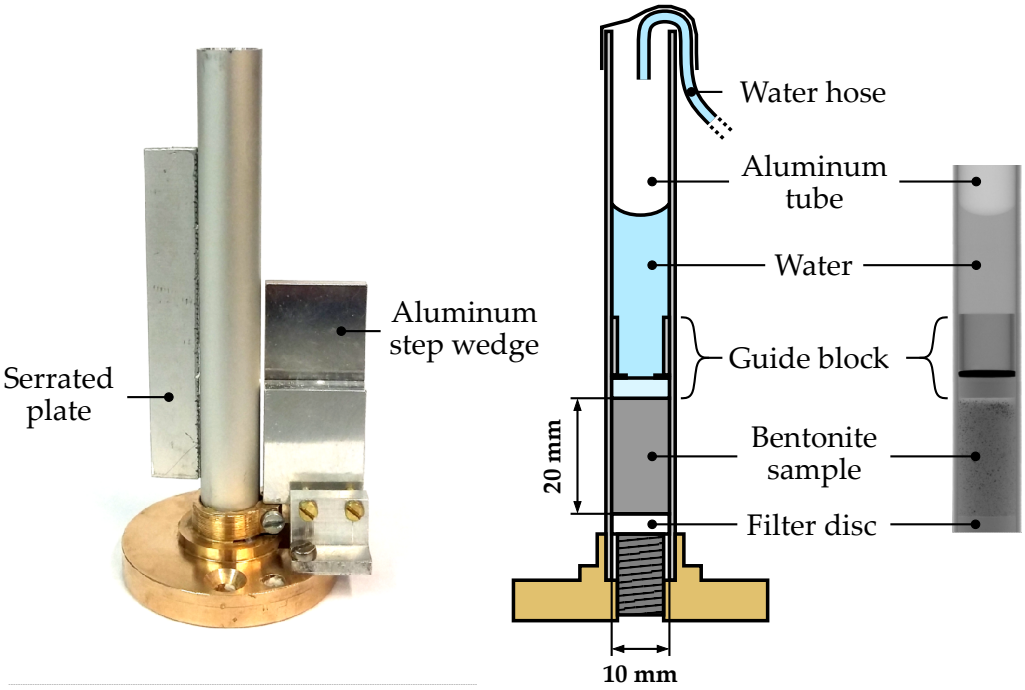

FIGURE 5.10 Photograph (left), schematic cross-sectional view (middle) and X-ray image (right) of sample holder used in swelling experiments. Adapted from [P3] under the license CC BY 4.0.

was able to freely move upward with a guide block permeable to water. An aluminum step wedge consisting of two plates of different thickness (3 and 8 mm) was attached next to the tube to be used for the local beam hardening correction. A total of 16 experiments were performed, where the initial dry density (1.40–1.80 $\mathrm{g/cm^3}$) and the initial water content (12%–24%) of the samples were varied. To facilitate the deformation measurement, iron particles ($d \approx 100\,\mu\mathrm{m}$, 1.5 wt%) were added and mixed with the bentonite powder before the compaction.

Imaging procedure

X-ray imaging was performed with a Skyscan 1172 microtomography device (see Figure 3.11) using a tube voltage of 100 kV, a tube current of 80 µA, Al+Cu (0.5 mm + 0.04 mm) filters, a pixel size of 32 µm and an exposure time of 10 × 1106 ms. The field of view was extended from 16 mm × 17 mm to 16 mm × 65 mm by taking partly overlapping images from different vertical positions. An automated image acquisition procedure was used to take X-ray images of the sample in the initial state and with three different imaging time intervals (20 s, 2 min, 20 min) after adding water (0.1 M NaCl) into the tube. X-ray images of the background and of the two aluminum correction plates in the step wedge were also taken regularly. After four days of swelling, the sample holder was quick-frozen in liquid nitrogen and cut into 4–6 slices of length around 7 mm. The partial densities of bentonite and water in the slices were determined gravimetrically. These results were used to validate the method in the final state.

Analysis

All the X-ray images taken of the sample were first corrected using the local beam hardening correction. Then the partially overlapping equivalent thickness images were stitched together. Normalized images were also calculated for the deformation measurement.

As the deformation of bentonite was effectively one-dimensional in this sample and wetting geometry, it was measured using a two-dimensional block matching algorithm applied only to the axial (or vertical) direction using 50 grid points with a spacing of around 13 pixels. The size of the block was around 310 $\times$ 40 pixels and the search radius was around 20 pixels. As the deformation was large, the reference block was updated whenever the correlation was too low according to Equation 4.11. The difference between the results and the gravimetric validation data was used to find the optimal value for the parameter k. The deformation was, however, observed to slightly deviate from the one-dimensional case, and thus the measurement was prone to sampling error. This is likely the main reason for relatively high scatter in the final results in some experiments. As the displacement of the top end was difficult to measure accurately with the block matching algorithm (tracer particle density became too low), it was measured more accurately by fitting sigmoid curves to attenuation coefficient profiles near the ends.

The mass attenuation coefficients of bentonite and water were obtained by performing sample-specific two-point calibration, using the data from the sample

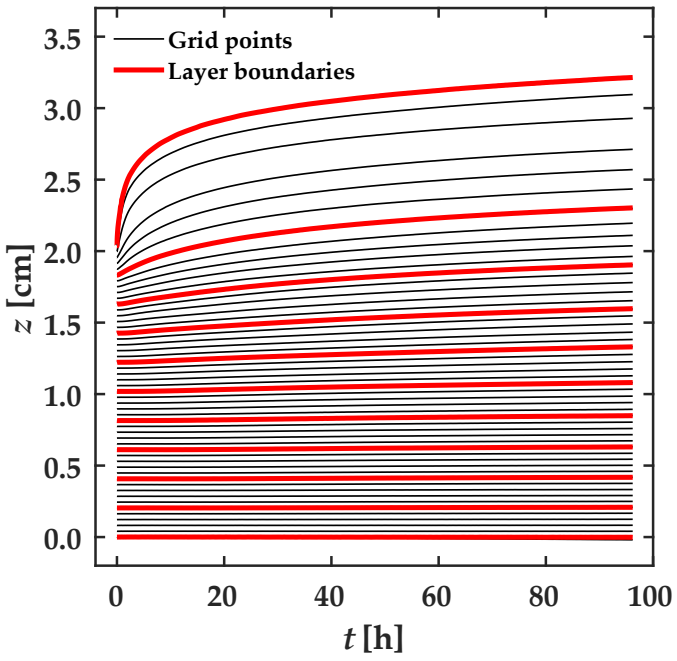

FIGURE 5.11 Example of measured deformation of sample. Adapted from [P3] under the license CC BY 4.0.

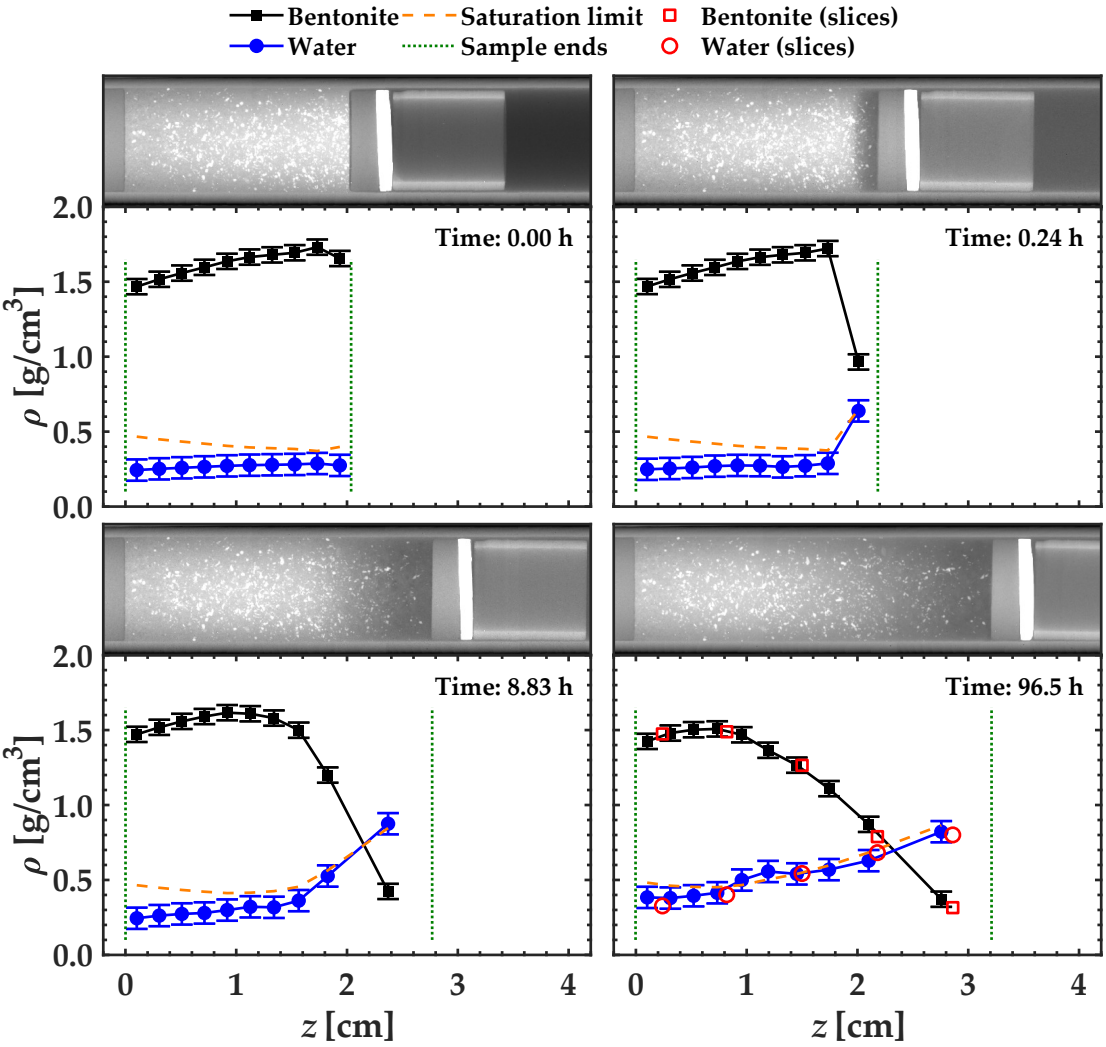

FIGURE 5.12 Example of results in swelling experiments. The partial density profiles of bentonite and water, and the saturation limit are plotted at four instants of time. The validation data, measured from the sliced sample, are plotted in the last subfigure. On the top of each plot is the corresponding X-ray image (aluminum equivalent thickness image). Adapted from [P3] under the license CC BY 4.0.

in the reference state and from the water layer above the sample. The density analysis was performed by first dividing the sample into 10 virtual layers in the reference state. Such a low number of layers was used to improve the signal-to-noise ratio. The mass of bentonite (m_b) in each layer was calculated from the reference state image. The measured deformation was used to track the positions of the layer boundaries, which were used to calculate the volume, the partial density of bentonite (m_b is conserved in layers), the attenuation coefficient and the partial density of water in each layer in the deformed states.

Results

Exemplarily, the result of a deformation measurement is shown in Figure 5.11. The deformation is rapid and large in the upper layers, while it is negligible in the lower layers. Apparently, no stationary stage is reached after four days of swelling, although the swelling rate is slowed down.

Also exemplarily, the partial density profiles of bentonite and water, are shown in Figure 5.12. The top part of the sample quickly swells and saturates, while the partial density of bentonite in the bottom part remains almost unchanged. However, the partial density of water is increased also in the bottom part. In some experiments, relatively large gas filled voids (possibly released compressed pore air) were visible in the upper part of the sample at later times, but they did not compromise the applicability of the method.

5.4 Sedimentation of dilute bentonite suspension

The purpose of the sedimentation experiment was to find out the critical water content below which bentonite suspension is able to support the weight of the tracer particles used in the swelling experiments (Section 5.3). Above this value, the deformation measurement obviously fails as the particles do not follow the movement of the solid material. See the supplementary material of Publication P3 for more details on this application.

Experimental setup

The initial plan was to drop tracer particles into suspensions of different concentrations, and then use X-ray imaging to observe in which suspensions the particles would sink to the bottom and in which they would keep floating. However, this approach failed since the suspensions started to sediment and non-trivial partial density profiles of bentonite were formed in the vertical direction.

An alternative way to find out the critical water content was used. A single suspension of water content $w = 20$, made of saline water (0.1 M NaCl) and MX-80 bentonite, was poured into an empty sample holder tube (Figure 5.10). The suspension was let to sediment for around 1 d, and thereafter some tracer particles were dropped into the tube. X-ray images of the sample holder tube and correction plates, with similar settings and procedures than in Section 5.3, were taken at four different times (0 h, 0.5 h, 5 h and 4 d after dropping the particles). X-ray images of the empty and water filled tube were also taken.

Analysis

As the blurring effect around the particles hampered the analysis, the X-ray images were first deblurred using the method described in Section 4.2. Thereafter, the images were corrected using the local beam hardening correction (Section 4.3). The resulting aluminum equivalent thickness images were used to calculate the relative attenuation coefficient profiles in the axial direction. The suspension was assumed to be fully saturated all the time, and hence Equations 4.12 and 4.17 can be combined to yield

$$\mu' = \mu'_w + C'_d \cdot \rho_d \,, \tag{5.1}$$

where the relative attenuation coefficient of water (μ'_w) was obtained from the image of the water filled tube. The coefficient $C'_d = c'_d - c'_w \cdot \rho^*_w / \rho^*_b$ was calculated from the equation

$$m_b = \int\limits_{V_{\text{sample}}} \rho_d dV = \frac{A}{C'_d} \int\limits_{z_1}^{z_2} (\mu' - \mu'_w)\, dz \,, \tag{5.2}$$

as the total mass of bentonite m_b in the suspension and the cross-sectional area of the tube A were known. The partial density profiles of bentonite and water were then calculated using Equations 5.1 and 4.17, respectively.

Results

Figure 5.13 shows the equivalent thickness image and the partial density profiles of bentonite and water 5 h after dropping the particles. Also shown are the partial density profiles without deblurring, giving incorrect values near the particles. The critical water content was measured to be around $w_c = 20$. The water content values in the samples were generally well below this value in the swelling experiments, and hence the tracer particles were assumed to follow the motion of bentonite.

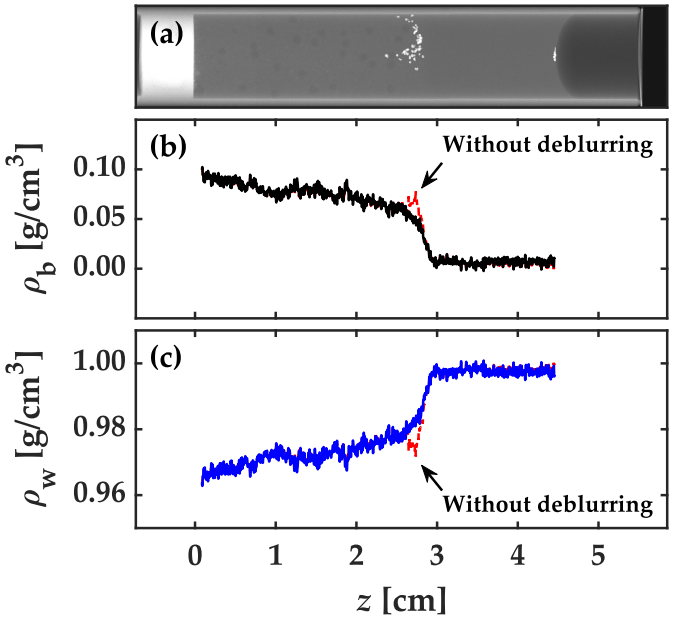

FIGURE 5.13 Sedimentation experiment 5 h after adding particles. An X-ray image (aluminum equivalent thickness image) shows that most of the particles are located in the middle of the tube (a). The calculated partial density profiles of bentonite (b) and water (c) can be used to calculate the critical water content. Also shown are profiles without deblurring. Adapted from [P3] under the license CC BY 4.0.

6 CONCLUSIONS

A method based on X-ray imaging or X-ray tomography for monitoring water transport and deformation in swelling materials was introduced. Several images of a wetting or drying sample are used to measure the displacement field and to calculate the partial densities of solid and water as a function of time. X-ray imaging is suitable to monitor fast processes in simple sample geometries, whereas X-ray tomography can be used for any geometry, provided that the process is slow enough. It is assumed that the sample consists of solid and water, whose mass attenuation coefficients, and thus the elemental compositions, are constant across the sample. The sample should also contain natural or added details visible in images, which follow the motion of the solid material and allow the deformation measurement based on image correlation. The water content distribution needs to be known in the reference state. Often, the initial state is the most straightforward choice for the reference state, but any intermediate or final state can be used, if known. A modification of the method, where the partial densities can be calculated without the deformation measurement applicable for cases where the sample is fully saturated, was also introduced.

Although the method is relatively straightforward, different image artifacts and challenges in the deformation measurement make quantitative image analysis difficult. Beam hardening, caused by a polychromatic X-ray source (e.g., X-ray tube), is the most important artifact to correct, and was here first corrected using the standard polynomial beam hardening correction. To increase accuracy, the local beam hardening correction was developed and used to correct spatial and temporal variations of beam hardening and other nonlinearities arising from the detector. While this correction method was here used only in X-ray imaging, it can also be used in X-ray tomography. Another special correction method, deblurring based on deconvolution, turned out to be useful in the sedimentation experiment, where it reduced the errors caused by blurring around highly attenuating tracer particles. Some image artifacts could not be corrected here, but their correction should be considered in the future. The cone beam artifact caused error at the

ends of the sample, as it mixes the attenuation coefficient values of materials on different sides of an interface. This artifact could be avoided by using a different source trajectory that allows exact reconstruction (e.g., helical trajectory). X-ray scattering from the sample was not considered here, but as the Compton scattering is a significant interaction mechanism (dominant at higher X-ray energies and in low-Z materials), it very likely adds systematic error to the results. The scattering is a complex phenomenon and thus difficult to correct. It can possibly be removed, e.g., by measuring its contribution using a beam-stop array or by simulations. The deformation measurement is likely the weakest link of the method. Displacements need to be measured very accurately as small errors cause relative large errors to the final results (partial densities). Here, sampling error, spurious movements of some details and challenges near the edges caused error to the measured displacements. By using energy-sensitive imaging, the final results could, at least in theory, be calculated without using the deformation measurement.

Despite the above-mentioned challenges and sources of errors, the method was successfully applied to bentonite and biocomposite samples. The results obtained by the method were plausible and essentially consistent with the validation data. Such results are useful for developing and validating mechanical and water transport models for these materials. Better models for the bentonite buffer are needed for more reliable safety assessments of nuclear waste disposal concepts, and better understanding of water transport in biocomposite materials helps to develop more durable materials. The method is, however, not restricted to the materials used here, it can potentially be used for many other solids and liquids as well.

REFERENCES

[1] Amiry-Moghaddam, M. and Ottersen, O. P. The molecular basis of water transport in the brain. *Nature Reviews Neuroscience*, 4(12):991–1001, 2003.

[2] Bodner, G., Nakhforoosh, A., and Kaul, H.-P. Management of crop water under drought: a review. *Agronomy for Sustainable Development*, 35(2):401–442, 2015.

[3] Banaei, S. M. A., Javid, A. H., and Hassani, A. H. Numerical simulation of groundwater contaminant transport in porous media. *International Journal of Environmental Science and Technology*, 18(1):151–162, 2021.

[4] Roy, S. and Bhalla, S. K. Role of geotechnical properties of soil on civil engineering structures. *Resources and Environment*, 7(4):103–109, 2017.

[5] Gusman, M., Nazki, A., and Putra, R. R. The modelling influence of water content to mechanical parameter of soil in analysis of slope stability. *Journal of Physics: Conference Series*, 1008:012022, 2018.

[6] Viitanen, H., Vinha, J., Salminen, K., Ojanen, T., Peuhkuri, R., Paajanen, L., and Lähdesmäki, K. Moisture and Bio-deterioration Risk of Building Materials and Structures. *Journal of Building Physics*, 33(3):201–224, 2010.

[7] Guo, Y., Li, Y., Tokura, H., Wong, T., Chung, J., Wong, A. S. W., Indulal Gohel, M. D., and Hang Mei Leung, P. Impact of fabric moisture transport properties on physiological responses when wearing protective clothing. *Textile Research Journal*, 78(12):1057–1069, 2008.

[8] Gao, Y. and Cranston, R. Recent Advances in Antimicrobial Treatments of Textiles. *Textile Research Journal*, 78(1):60–72, 2008.

[9] Mohorič, A., Vergeldt, F., Gerkema, E., de Jager, A., van Duynhoven, J., van Dalen, G., and Van As, H. Magnetic resonance imaging of single rice kernels during cooking. *Journal of Magnetic Resonance*, 171(1):157–162, 2004.

[10] Ben Abdelouahab, N., Gossard, A., Ma, X., Dialla, H., Maillet, B., Rodts, S., and Coussot, P. Understanding mechanisms of drying of a cellulose slurry by magnetic resonance imaging. *Cellulose*, 28(9):5321–5334, 2021.

[11] Zhao, H., Wu, X., Huang, Y., Zhang, P., Tian, Q., and Liu, J. Investigation of moisture transport in cement-based materials using low-field nuclear magnetic resonance imaging. *Magazine of Concrete Research*, 73(5):252–270, 2021.

[12] Cai, C., Javed, M. A., Komulainen, S., Telkki, V.-V., Haapala, A., and Heräjärvi, H. Effect of natural weathering on water absorption and pore size distribution in thermally modified wood determined by nuclear magnetic

resonance. *Cellulose*, 27(8):4235–4247, 2020.

[13] Esser, H. G., Carminati, A., Vontobel, P., Lehmann, E. H., and Oswald, S. E. Neutron radiography and tomography of water distribution in the root zone. *Journal of Plant Nutrition and Soil Science*, 173(5):757–764, 2010.

[14] Defraeye, T., Aregawi, W., Saneinejad, S., Vontobel, P., Lehmann, E., Carmeliet, J., Verboven, P., Derome, D., and Nicolaï, B. Novel Application of Neutron Radiography to Forced Convective Drying of Fruit Tissue. *Food and Bioprocess Technology*, 6(12):3353–3367, 2013.

[15] Tanaka, T., Avramidis, S., and Shida, S. Evaluation of moisture content distribution in wood by soft X-ray imaging. *Journal of Wood Science*, 55(1):69–73, 2009.

[16] Oesch, T., Weise, F., Meinel, D., and Gollwitzer, C. Quantitative in-situ Analysis of Water Transport in Concrete Completed Using X-ray Computed Tomography. *Transport in Porous Media*, 127(2):371–389, 2019.

[17] Hall, L. D., Amin, M. G., Dougherty, E., Sanda, M., Votrubova, J., Richards, K. S., Chorley, R. J., and Cislerova, M. MR properties of water in saturated soils and resulting loss of MRI signal in water content detection at 2 tesla. *Geoderma*, 80(3-4):431–448, 1997.

[18] Lehmann, E. H. Neutron Imaging Facilities in a Global Context. *Journal of Imaging*, 3(4):52, 2017.

[19] Khaddour, G., Riedel, I., Andò, E., Charrier, P., Bésuelle, P., Desrues, J., Viggiani, G., and Salager, S. Grain-scale characterization of water retention behaviour of sand using X-ray CT. *Acta Geotechnica*, 13:497–512, 2018.

[20] Chen, Y., Jha, N. K., Al-Bayati, D., Lebedev, M., Sarmadivaleh, M., Iglauer, S., Saeedi, A., and Xie, Q. Geochemical controls on wettability alteration at pore-scale during low salinity water flooding in sandstone using X-ray micro computed tomography. *Fuel*, 271:117675, 2020.

[21] Danvind, J. *Methods for Collecting and Analysing Simultaneous Strain and Moisture Data During Wood-Drying*. Licentiate thesis, Luleå University of Technology, 2002.

[22] Watanabe, K., Lazarescu, C., Shida, S., and Avramidis, S. A Novel Method of Measuring Moisture Content Distribution in Timber During Drying Using CT Scanning and Image Processing Techniques. *Drying Technology*, 30(3):256–262, 2012.

[23] Hansson, L. and Fjellner, B.-A. Wood Shrinkage Coefficient and Dry Weight Moisture Content Estimations from CT-Images. *Pro Ligno*, 9(4):557–561, 2013.

[24] Kogel, J. E., Trivedi, N. C., Barker, J. M., and Krukowski, S. T. *Industrial Min-*

erals & Rocks: Commodities, Markets, and Uses. Society for Mining, Metallurgy, and Exploration, 2006.

[25] Karnland, O., Olsson, S., and Nilsson, U. Mineralogy and sealing properties of various bentonites and smectite-rich clay materials. Technical Report TR-06-30, SKB, 2006.

[26] Christidis, G. E. and Huff, W. D. Geological Aspects and Genesis of Bentonites. *Elements*, 5(2):93–98, 2009.

[27] Inoue, A. *Formation of Clay Minerals in Hydrothermal Environments*, ch. 7, pp. 268–329. Springer, 1995.

[28] U.S. Geological Survey. Mineral commodity summaries 2023: U.S. Geological Survey, 210 p., 2023.

[29] Eisenhour, D. D. and Brown, R. K. Bentonite and Its Impact on Modern Life. *Elements*, 5(2):83–88, 2009.

[30] Hedin, A. Spent nuclear fuel – how dangerous is it? A report from the project "Description of risk". Technical Report 97-13, SKB, 1997.

[31] Bruno, J. and Ewing, R. C. Spent Nuclear Fuel. *Elements*, 2(6):343–349, 2006.

[32] Sellin, P. and Leupin, O. X. The use of clay as an engineered barrier in radioactive-waste management – a review. *Clays and Clay Minerals*, 61(6):477–498, 2013.

[33] Posiva Oy. Safety Case for the Disposal of Spent Nuclear Fuel at Olkiluoto – Models and Data for the Repository System 2012. Technical Report 2013-01, Posiva Oy, 2013.

[34] Posiva Oy. Posiva Oy image gallery. https://www.posiva.fi/en/index/media/material.html. Accessed on 2023-04-28.

[35] Hillier, S. *Clay mineralogy*, pp. 223–228. Springer, Berlin, Heidelberg, 1978.

[36] Al-Ani, T. and Sarapää, O. Clay and clay mineralogy. Technical report, GTK, 2008.

[37] Ploehn, H. J. and Liu, C. Quantitative Analysis of Montmorillonite Platelet Size by Atomic Force Microscopy. *Industrial & Engineering Chemistry Research*, 45(21):7025–7034, 2006.

[38] Matusewicz, M. and Olin, M. Comparison of microstructural features of three compacted and water-saturated swelling clays: MX-80 bentonite and Na-and Ca-purified bentonite. *Clay Minerals*, 54(1):75–81, 2019.

[39] Segad, M., Hanski, S., Olsson, U., Ruokolainen, J., Åkesson, T., and Jönsson, B. Microstructural and Swelling Properties of Ca and Na Montmorillonite: (In Situ) Observations with Cryo-TEM and SAXS. *The Journal of Physical*

Chemistry C, 116(13):7596–7601, 2012.

[40] Delage, P., Marcial, D., Cui, Y. J., and Ruiz, X. Ageing effects in a compacted bentonite: a microstructure approach. *Géotechnique*, 56(5):291–304, 2006.

[41] Lloret, A. and Villar, M. V. Advances on the knowledge of the thermo-hydro-mechanical behaviour of heavily compacted "FEBEX" bentonite. *Physics and Chemistry of the Earth, Parts A/B/C*, 32(8-14):701–715, 2007.

[42] Neretnieks, I., Longcheng, L., and Moreno, L. Mechanisms and models for bentonite erosion. Technical Report TR-09-35, SKB, 2009.

[43] Appelo, C. A. J. A Review of Porosity and Diffusion in Bentonite. Technical Report 2013-29, Posiva Oy, 2013.

[44] O'Kelly, B. C. Oven-Drying Characteristics of Soils of Different Origins. *Drying Technology*, 23(5):1141–1149, 2005.

[45] Vieillard, P., Tajeddine, L., Gailhanou, H., Blanc, P., Lassin, A., and Gaboreau, S. Thermo-Analytical Techniques on MX-80 Montmorillonite: A Way to Know the Behavior of Water and its Thermodynamic Properties during Hydration – Dehydration Processes. *Pharmaceutica Analytica Acta*, 7(2), 2016.

[46] Lang, L. Z., Xiang, W., Huang, W., Cui, D. S., and Schanz, T. An experimental study on oven-drying methods for laboratory determination of water content of a calcium-rich bentonite. *Applied Clay Science*, 150:153–162, 2017.

[47] Suuronen, J.-P., Matusewicz, M., Olin, M., and Serimaa, R. X-ray studies on the nano-and microscale anisotropy in compacted clays: Comparison of bentonite and purified calcium montmorillonite. *Applied Clay Science*, 101:401–408, 2014.

[48] Villar, M. V. MX-80 Bentonite. Thermo-Hydro-Mechanical Characterisation Performed at CIEMAT in the Context of the Prototype Project. Technical Report 1053, CIEMAT, 2005.

[49] Savage, D. Prospects for coupled modelling. Technical Report STUK-TR 13, STUK, 2012.

[50] Kolditz, O., Görke, U.-J., Shao, H., and Wang, W. *Thermo-Hydro-Mechanical-Chemical Processes in Fractured Porous Media – Benchmarks and Examples*. Springer, 2012.

[51] Pulkkanen, V.-M. *A large deformation model for chemoelastic porous media: Bentonite clay in spent nuclear fuel disposal*. Ph.D. thesis, Aalto University, 2019.

[52] Zha, Y., Yang, J., Zeng, J., Tso, C.-H. M., Zeng, W., and Shi, L. Review of numerical solution of Richardson–Richards equation for variably saturated flow in soils. *Wiley Interdisciplinary Reviews: Water*, 6(5):e1364, 2019.

[53] van Genuchten, M. T. A Closed-form Equation for Predicting the Hydraulic Conductivity of Unsaturated Soils. *Soil Science Society of America Journal*, 44(5):892–898, 1980.

[54] Baker, R. and Frydman, S. Unsaturated soil mechanics: Critical review of physical foundations. *Engineering Geology*, 106(1-2):26–39, 2009.

[55] Kröhn, K.-P. Modelling the re-saturation of bentonite in final repositories in crystalline rock. Technical Report GRS - 199, GRS, 2004.

[56] Kröhn, K.-P. Code VIPER: Theory and Current Status. Technical Report GRS - 269, GRS, 2011.

[57] Campbell, F. C. *Structural Composite Materials*. ASM International, 2010.

[58] Chawla, K. K. *Composite Materials: Science and Engineering*. Springer, 3rd edition, 2012.

[59] Mohanty, A. K., Misra, M., and Drzal, L. T. Sustainable Bio-Composites from Renewable Resources: Opportunities and Challenges in the Green Materials World. *Journal of Polymers and the Environment*, 10(1–2):19–26, 2002.

[60] Nanda, S., Patra, B. R., Patel, R., Bakos, J., and Dalai, A. K. Innovations in applications and prospects of bioplastics and biopolymers: a review. *Environmental Chemistry Letters*, 20(1):379–395, 2022.

[61] Mohanty, A. K., Misra, M., , and Hinrichsen, G. Biofibres, biodegradable polymers and biocomposites: An overview. *Macromolecular Materials and Engineering*, 276–277(1):1–24, 2000.

[62] Russo, P. *Handbook of X-ray Imaging: Physics and Technology*. CRC Press, 1st edition, 2017.

[63] Berger, M. J., Hubbell, J. H., Seltzer, S. M., Chang, J., Coursey, J. S., Sukumar, R., Zucker, D. S., and Olsen, K. XCOM: Photon Cross Section Database (version 1.5), 2010.

[64] Hemberg, O., Otendal, M., and Hertz, H. M. Liquid-metal-jet anode x-ray tube. *Optical Engineering*, 43(7):1682–1688, 2004.

[65] Bushberg, J. T., Seibert, J. A., Leidholdt Jr., E. M., and M. Boone, J. *The Essential Physics of Medical Imaging*. Lippincott Williams & Wilkins, 2nd edition, 2002.

[66] Uesugi, K., Hoshino, M., and Yagi, N. Comparison of lens-and fiber-coupled CCD detectors for X-ray computed tomography. *Journal of Synchrotron Radiation*, 18(2):217–223, 2011.

[67] Ballabriga, R., Alozy, J., Bandi, F. N., Campbell, M., Egidos, N., Fernandez-Tenllado, J. M., Heijne, E. H. M., Kremastiotis, I., Llopart, X., Madsen, B. J.,

Pennicard, D., and Tlustos, L. Photon Counting Detectors for X-Ray Imaging With Emphasis on CT. *IEEE Transactions on Radiation and Plasma Medical Sciences*, 5(4):422–440, 2021.

[68] Kak, A. C. and Slaney, M. *Principles of Computerized Tomographic Imaging*. IEEE Press, 1988.

[69] Peyrin, F. and Engelke, K. CT Imaging: Basics and New Trends. In *Handbook of Particle Detection and Imaging*, pp. 883–915. Springer, 2012.

[70] Hsieh, J., Nett, B., Yu, Z., Sauer, K., Thibault, J.-B., and Bouman, C. A. Recent Advances in CT Image Reconstruction. *Current Radiology Reports*, 1(1):39–51, 2013.

[71] Feldkamp, L. A., Davis, L. C., and Kress, J. W. Practical cone-beam algorithm. *Journal of the Optical Society of America A*, 1(6):612–619, 1984.

[72] Tuy, H. K. An Inversion Formula for Cone-Beam Reconstruction. *SIAM Journal on Applied Mathematics*, 43(3):546–552, 1983.

[73] Geyer, L. L., Schoepf, U. J., Meinel, F. G., Nance Jr, J. W., Bastarrika, G., Leipsic, J. A., Paul, N. S., Rengo, M., Laghi, A., and De Cecco, C. N. State of the Art: Iterative CT Reconstruction Techniques. *Radiology*, 276(2):339–357, 2015.

[74] Shuman, W. P., Green, D. E., Busey, J. M., Kolokythas, O., Mitsumori, L. M., Koprowicz, K. M., Thibault, J.-B., Hsieh, J., Alessio, A. M., Choi, E., and Kinahan, P. E. Model-Based Iterative Reconstruction Versus Adaptive Statistical Iterative Reconstruction and Filtered Back Projection in Liver 64-MDCT: Focal Lesion Detection, Lesion Conspicuity, and Image Noise. *American Journal of Roentgenology*, 200(5):1071–1076, 2013.

[75] Qiu, D. and Seeram, E. Does Iterative Reconstruction Improve Image Quality and Reduce Dose in Computed Tomography? *Radiology – Open Journal*, 1(2):42–54, 2016.

[76] Osborne, N. L., Høibø, Ø. A., and Maguire, D. A. Estimating the density of coast Douglas-fir wood samples at different moisture contents using medical X-ray computed tomography. *Computers and Electronics in Agriculture*, 127:50–55, 2016.

[77] Balázs, G. L., Czoboly, O., Lublóy, É., Kapitány, K., and Barsi, Á. Observation of steel fibres in concrete with Computed Tomography. *Construction and Building Materials*, 140:534–541, 2017.

[78] Stock, S. R. *MicroComputed Tomography: Methodology and Applications*. CRC press, 2009.

[79] Barrett, J. F. and Keat, N. Artifacts in CT: Recognition and Avoidance. *RadioGraphics*, 24(6):1679–1691, 2004.

[80] Zou, W., Hunter, N., and Swain, M. V. Application of Polychromatic μCT for Mineral Density Determination. *Journal of Dental Research*, 90(1):18–30, 2011.

[81] Johns, H. E. and Cunningham, J. R. *The Physics of Radiology*. Charles C Thomas Publisher, 4th edition, 1983.

[82] Nikl, M. Scintillation detectors for x-rays. *Measurement Science and Technology*, 17(4):R37–R54, 2006.

[83] Moretti, F., Patton, G., Belsky, A., Petrosyan, A. G., and Dujardin, C. Deep traps can reduce memory effects of shallower ones in scintillators. *Physical Chemistry Chemical Physics*, 18(2):1178–1184, 2016.

[84] Zhu, R.-y. Radiation damage in scintillating crystals. *Nuclear Instruments and Methods in Physics Research Section A: Accelerators, Spectrometers, Detectors and Associated Equipment*, 413(2-3):297–311, 1998.

[85] Celestre, R., Rosenberger, M., and Notni, G. A novel algorithm for bad pixel detection and correction to improve quality and stability of geometric measurements. *Journal of Physics: Conference Series*, 772:012002, 2016.

[86] López-Portilla, B. M., Valenzuela, W., Zarkesh-Ha, P., and Figueroa, M. A CMOS Image Readout Circuit with On-Chip Defective Pixel Detection and Correction. *Sensors*, 23(2):934, 2023.

[87] Lifton, J. and Liu, T. Ring artefact reduction via multi-point piecewise linear flat field correction for X-ray computed tomography. *Optics Express*, 27(3):3217–3228, 2019.

[88] Ketcham, R. A. New algorithms for ring artifact removal. *Developments in X-ray tomography V*, 6318:216–222, 2006.

[89] Katsura, M., Sato, J., Akahane, M., Kunimatsu, A., and Abe, O. Current and Novel Techniques for Metal Artifact Reduction at CT: Practical Guide for Radiologists. *RadioGraphics*, 38(2):450–461, 2018.

[90] García-Moreno, F., Kamm, P. H., Neu, T. R., Bülk, F., Mokso, R., Schlepütz, C. M., Stampanoni, M., and Banhart, J. Using X-ray tomoscopy to explore the dynamics of foaming metal. *Nature Communications*, 10(1):1–9, 2019.

[91] Gonzalez, R. C. and Woods, R. E. *Digital Image Processing*. Prentice Hall, 2nd edition, 2002.

[92] Smith, S. W. *The Scientist and Engineer's Guide to Digital Signal Processing*. California Technical Publishing, 1997.

[93] Hickstein, D. D., Gibson, S. T., Yurchak, R., Das, D. D., and Ryazanov, M. A direct comparison of high-speed methods for the numerical Abel transform. *Review of Scientific Instruments*, 90(6):065115, 2019.

[94] Hisham, M. B., Yaakob, S. N., Raof, R. A. A., Nazren, A. B. A., and Wafi, N. M. Template Matching Using Sum of Squared Difference and Normalized Cross Correlation. *2015 IEEE Student Conference on Research and Development (SCOReD)*, pp. 100–104, 2015.

[95] Foroosh, H., Zerubia, J. B., and Berthod, M. Extension of Phase Correlation to Subpixel Registration. *IEEE Transactions on Image Processing*, 11(3):188–200, 2002.

[96] Feng, S., Deng, L., Shu, G., Wang, F., Deng, H., and Ji, K. A Subpixel Registration Algorithm for Low PSNR Images. *2012 IEEE Fifth International Conference on Advanced Computational Intelligence (ICACI)*, pp. 626–630, 2012.

[97] Wang, H., Qian, H., Gao, Y., and Li, Y. Classification and physical characteristics of bound water in loess and its main clay minerals. *Engineering Geology*, 265:105394, 2020.

[98] Lämsä, J. *Veden kulkeutumisen ja muodonmuutosten mittaaminen MX-80-tyyppisessä bentoniitissa röntgenmikrotomografisin menetelmin*. M.Sc. thesis, University of Jyväskylä, 2015.

[99] Abed, A. A., Laitinen, M., Lämsä, J., Harjupatana, T., Sołowski, W. T., and Kataja, M. Hydro-mechanical modelling of MX-80 bentonite: one dimensional study. *E3S Web of Conferences*, 9:18005, 2016.

[100] Chen, L., Chu, H.-W., and Fan, X. A Convection–Diffusion Porous Media Model for Moisture Transport in Polymer Composites: Model Development and Validation. *Journal of Polymer Science Part B: Polymer Physics*, 53(20):1440–1449, 2015.

[101] Liu, J. and Neretnieks, I. Physical and chemical stability of the bentonite buffer. Technical Report R-06-103, SKB, 2007.

ORIGINAL PUBLICATIONS

P1

X-RAY TOMOGRAPHIC METHOD FOR MEASURING THREE-DIMENSIONAL DEFORMATION AND WATER CONTENT DISTRIBUTION IN SWELLING CLAYS

by

Harjupatana T., Alaraudanjoki J., and Kataja M. 2015

Applied Clay Science 114 (2015) 386–394

https://doi.org/10.1016/j.clay.2015.06.016

Applied Clay Science 114 (2015) 386–394

Contents lists available at ScienceDirect

Applied Clay Science

journal homepage: www.elsevier.com/locate/clay

Research paper

X-ray tomographic method for measuring three-dimensional deformation and water content distribution in swelling clays

Tero Harjupatana *, Jarno Alaraudanjoki, Markku Kataja

Department of Physics, University of Jyväskylä, P.O. Box 35 (YFL), FI-40014, Finland

ARTICLE INFO

Article history:
Received 13 January 2015
Received in revised form 2 June 2015
Accepted 4 June 2015
Available online 2 July 2015

Keywords:
X-ray tomography
Water content
Water transport
Deformation
Bentonite
Swelling

ABSTRACT

A non-invasive method for simultaneous measurement of the 3D displacement field and the water content distribution of a wetted solid material is developed. The method is based on comparison of X-ray tomographic images of a material sample in the reference state and in the wetted and deformed state. The deformation and water content analyses were successfully compared with numerical results for a cylindrical rubber test sample under axial compression, and with gravimetric results from axially wetted and sliced cylindrical bentonite samples, respectively. The methods were applied in a 4D study (three spatial dimensions and time) of wetting and deformation of purified swelling bentonite doped with glass tracer particles, and wetted with synthetic groundwater. The results obtained for bentonite samples are repeatable and appear qualitatively correct and plausible. They are useful e.g. in validating models involving transport of water and the resulting swelling deformation of bentonite. The method is potentially applicable also in other processes involving liquid transport and deformation such as wetting/swelling and drying/shrinking of heterogeneous materials. A prerequisite for the applicability of the method is that the material contains sufficient amount of local inhomogeneities visible and identifiable in successive tomographic images to facilitate deformation analysis, and that change in water content affects the total density enough to be observable in X-ray images.

1. Introduction

Transport of liquids in partially saturated solid materials and the possible deformation of the material induced by local changes in liquid content are of great interest in many areas of materials science and technology. A number of complex physical and chemical mechanisms contribute to such transport and deformation in processes involving wetting or drying of e.g. soils, building materials, foods and various biological materials (Carmeliet and Roels, 2001; Moldrup et al., 2001; Meinzer, 2002; Saguy et al., 2005). Theoretical approaches based on first principles towards modeling these processes tend to become complicated, and phenomenological input is often required. Measuring the total liquid content and global deformation of a wetting/drying material sample is rather straightforward by conventional gravimetric and morphological methods (Gardner et al., 2000; Orteu, 2009). In their early work, Anderson et al. used medical X-ray tomographic device for rapid non-destructive measurement of bulk density and water content of soil samples (Anderson et al., 1988). At least rough local information can be obtained by destructive segmenting of the sample. Non-invasive techniques based e.g. on nuclear magnetic resonance, electric properties of material, and various modalities of tomography have also been used for measuring the local three-dimensional liquid content distribution (Herrmann et al., 2002; Huisman et al., 2003; Mukhlisin et al., 2012; Aregawi et al., 2013) or the local deformation of material samples in various mechanical conditions (Bart-Smith et al., 1998; Peth et al., 2010). Very few efforts appears to have been made towards simultaneous non-destructive measurement of the evolution of both the liquid content and the local deformation field of a material sample during wetting or drying process. Availability of such a measurement method would be potentially very useful for experimental research of processes involving liquid transport and the resulting deformation, and for development and validation of theoretical models of such processes. In this work, we introduce a method based on X-ray microtomography for non-destructive simultaneous measurement of three-dimensional distribution of local water content and displacement field of a wetted material. The method is applied in monitoring the swelling behavior of a wetting bentonite sample.

With X-ray tomography, the spatial distribution of the linear X-ray attenuation coefficient in the sample is obtained (Stock, 2008). The data is conveniently represented as a three-dimensional grayscale image allowing not only visualization but also quantitative study of the internal structure of many heterogeneous materials. The different material components of a multiphase material can be directly observed provided that the typical size scale of the phase domains is larger than the imaging resolution, that the difference between the values of the attenuation coefficient of various phases is large enough, and that the

* Corresponding author.
E-mail addresses: tero.t.harjupatana@jyu.fi (T. Harjupatana), jarno.s.alaraudanjoki@jyu.fi (J. Alaraudanjoki), markku.t.kataja@jyu.fi (M. Kataja).

http://dx.doi.org/10.1016/j.clay.2015.06.016
0169-1317/

phase configuration remains stable during the time of tomographic imaging. In such a case, the relative amount and distribution of various phases can be found in a straightforward manner using 3D image analysis techniques (Wildenschild et al., 2005; Tippkötter et al., 2009; Riedel et al., 2012). Sammartino et al. have used such an approach together with a relatively fast medical X-ray tomographic scanner in order to characterize flow in macropores of soil samples (Sammartino et al., 2012).

However, although we consider here a solid material partially saturated with a water, i.e. a three-phase system of solid, water and gas, we cannot assume phase separation in the size scale given by the resolution of the X-ray tomographic technique available (~1 μm). Instead, each material volume of the size scale given by the imaging resolution, i.e. the image voxel, can contain all three phases that contribute to the total value of the attenuation constant and thus of the grayscale value of the voxel. A single tomographic image of a material sample can thus not provide direct information on the relative abundances of different phases. Such a case was also considered (Sammartino et al., 2012) in evaluating the amount of water contained in soil matrix regions with small-scale porosity in the vicinity of macropores.

In what follows, we neglect the effect of gas phase, and confine ourselves to cases where the attenuation coefficients of the bulk solid and water are the same order of magnitude such that the changes of water content in the solid material are observable with X-ray tomography. We also expect, that the water transport in the material is slow enough such that the phase configuration can be considered approximately stationary during tomographic imaging. (Depending on the technique used, the typical time required for a single X-ray tomographic scan can vary from a few minutes to several days.) Furthermore, we assume that an experimental correlation formula for the dependence of X-ray attenuation coefficient on solid and water contents can be found using some independent calibration method such as gravimetric measurement. In the case that the solid phase content is known, the water content distribution in the partially saturated state may then be found in a straightforward manner by utilizing the X-ray tomographic image. In many practical cases however, change in water content induces considerable solid phase deformation. Then, the local solid content in the sample is not known making it impossible to utilize the calibration data and find the water content based on the measured total attenuation coefficient only. Solution to the problem can be sought provided that an X-ray tomographic image of the same physical sample is taken in a reference state of known solid density. Using image correlation techniques on the images of the reference state and the partially saturated state of interest, called the 'current state' in what follows, the three-dimensional displacement field of the solid phase may be found. Given the reference state solid density, this deformation information can be used to calculate the local solid density distribution in the current state. Together with the total attenuation coefficient data (the X-ray tomographic image), the calibration correlation thus yields the water density distribution in the current state. A prerequisite for successful analysis of the displacement field is that the material contains local structures visible in tomographic images of both the reference state and the current state. In some cases, this may be achieved by doping the material with suitable marker particles.

The primary motivation for the present work has been the need for developing efficient experimental methods for studying groundwater transport and swelling mechanisms of bentonite. This type of clay can absorb large amount of water, swell multiple times of its original volume, and produce large swelling pressure if wetted confined in a closed space. Fully saturated compacted bentonite is considered as effective barrier for transport of water and various chemicals. Due to its unique properties, bentonite is widely used in many applications of soil mechanics as a buffer and sealing material. It is also planned to be used as buffer material in some repository concepts for used nuclear fuel. The long-term purpose of this work is to utilize the X-ray tomographic techniques in a '4D imaging' sense, i.e. monitoring the evolution of water content and deformation of wetting and swelling bentonite samples in three dimensions and as a function of time, thereby producing detailed experimental data for supporting development and validation of hydromechanical models of bentonite.

2. Methods

2.1. X-ray tomography

X-ray imaging is based on attenuation of X-rays in a material. The intensity I of a narrow monochromatic X-ray beam is attenuated in a material according to the Beer–Lambert law (Hubbell and Seltzer, 1996)

$$I = I_0 \cdot \mathrm{e}^{-\int \mu(x) dx}, \tag{1}$$

where μ is the linear attenuation coefficient (LAC) which can depend on position x along the beam path. The detector of a typical X-ray tomographic device consists of a phosphorescent screen that converts X-rays to visible light, and a digital camera. A single X-ray projection image of a sample represents the intensity ratio (I/I_0) detected on such a two-dimensional detector. In a typical X-ray tomographic imaging procedure, of the order of one thousand X-ray projection images of the sample are taken from different directions by rotating the sample in the X-ray beam. The three-dimensional distribution of LAC is then reconstructed from the projection images by a computer. The reconstructed data is represented as a three-dimensional image (stack of two-dimensional cross-sectional images) of the sample. The grayscale 'voxel' values in such an image are linearly correlated with the actual LAC value in the sample.

It can be shown that for a given substance the LAC is proportional to its bulk density (Hubbell and Seltzer, 1996). The mass attenuation coefficient, defined as $\mu_m = (\mu/\rho)$, is thus independent of density but depends on X-ray energy and the atomic number of the substance. For compound material of several substances the LAC is given by

$$\mu = \sum_i \left(\mu_{m,i} \cdot \rho_i\right), \tag{2}$$

where $\mu_{m,i}$ and ρ_i are the mass attenuation coefficient and the partial density of substance i, respectively (Hubbell and Seltzer, 1996). The partial density is defined as $\rho_i = \phi_i \tilde{\rho}_i$, where ϕ_i and $\tilde{\rho}_i$ are the volume fraction and the intrinsic material density of the substance, respectively (Soo, 1990).

The radiation source used in current laboratory scale tomographic devices is X-ray tube which produces a polychromatic X-ray beam. Since the attenuation constant depends on energy, the simple Beer–Lambert law, Eq. (1), does not exactly hold. However, in simple reconstruction algorithms, the effects of the wide X-ray energy spectrum are neglected leading to imaging artifacts such as beam hardening (Stock, 2008). Since the attenuation coefficient typically decreases with increasing energy, beam hardening appears in tomographic images as edges of the sample showing virtually more absorbing (denser) than the interior even for a homogeneous sample. For the present technique, beam hardening poses a challenge since it weakens the linear correlation between the grayscale value and the actual attenuation coefficient on which the method is heavily based on. The effects of beam hardening can be reduced by using metallic filters to cut the low energy part of the spectrum. A potential disadvantage of the filtering technique is that the overall intensity of the beam is decreased leading to longer imaging times. The remaining effects of the beam hardening effect can be corrected for in the reconstruction stage (Zou et al., 2011), whereby the approximate linear dependence of the total absorption coefficient and thus of the grayscale value on the partial densities can be retained. Another imaging defects typical to X-ray tomographic techniques include the ring artifact, which can be caused e.g. by a single

faulty pixel of the detector camera, and the cone beam artifact related to approximations used in reconstruction algorithms for conical X-ray beam geometries (Valton et al., 2006; Hsieh et al., 2013). The effects of these artifacts can be reduced, if not removed, by specific correction algorithms included in the standard reconstruction software or by post-processing of reconstructed images (Barrett and Keat, 2004; Stock, 2008).

The X-ray microtomographic device used in the present work was SkyScan 1172 desktop scanner which has a microfocus X-ray tube with maximum operating voltage of 100 kV and maximum power of 10 W. The full image size of the CCD camera is 4000 × 2096 pixels and the minimum pixel size is 0.7 μm. The best resolution (detail detectability) is approximately 5 μm. The maximum field-of-view size is 34 mm × 18 mm, achieved with 8.5 μm pixel size setting. For the purposes of the present study the device was used in a reduced resolution mode with image size 1000 × 524 pixels of size 24 μm. These settings allow 24 mm × 12.6 mm field of view, and a relatively short imaging time.

2.2. Experimental set-up and samples

The samples used in the experiments were made of a commercial purified bentonite supplied in a powder form (MP Biomedicals Bentonite). The initial water content of the bentonite powder was measured gravimetrically using oven drying at 105 °C and typical water content was around 7% by weight (this depends on storage conditions). In order to facilitate deformation measurement, hollow glass microspheres of diameter ~100 μm were mixed with the bentonite powder to act as inert tracer particles in the otherwise quite homogeneous material. Cylindrical samples of diameter 17 mm and height 10 mm were then made by compacting a weighed amount of bentonite powder in a mould into a predetermined mean solid phase partial density ('dry density') ρ_{s0} of 1.2 or 1.5 g/cm^3. The compacted bentonite sample was then carefully placed and confined in the sample holder (see Fig. 1), slightly pre-compressed to achieve firm contact with the inner surfaces of the sample casing.

During the experiment, the sample was held in approximately constant volume in a plastic (PEEK) tube and between cylindrical end-pieces. The end-pieces include wetting and venting channels, and glass sintered plates that allow water flow in the sample through the lower end surface, and escape of air through the upper surface. The wetting channel includes the necessary miniature valves and an air bleeding channel to allow for controlling the inflow of water in the sample and for removal of air from the channel and the lower sintered plate. Two versions of sample holder with sintered plate diameters 6 mm and 15 mm were used in the experiments. The sample holder equipped with the smaller sintered plate size was designed to produce a three-dimensional cylindrically symmetric set-up, while the sample holder with the larger sintered plate gives approximately one-dimensional axial wetting and swelling behavior. In practice, these symmetries may be violated to some extent due to inhomogeneities present in the samples. The sample holders also include force sensors for measuring swelling pressure at the top surface of the sample. The water used in wetting the bentonite sample was synthetic groundwater with total salt content of 0.26 g/l (Allard pH 7 water (Huitti et al., 1998)).

The experiment was started by taking a reference state tomographic image of the non-wetted sample. After that, the wetting channels and the lower sintered plate were carefully filled with water and the whole sample holder was immediately weighed with hoses and wires disconnected. The sample holder was then connected to water supply and the wetting of the sample was initiated. The wetting was periodically interrupted and the sample holder with the partially saturated sample weighed, scanned in the tomographic device, weighed again and reconnected to water supply to resume wetting. The scanning time was about 45 min, and the total time required for each scanning–weighing interval was about an hour. The procedure was repeated typically 10 times until the sample was completely saturated in about 1–2 weeks total time. The total water mass data obtained by weighings was used in calibrating the method for water content measurement, see Section 2.4. Examples of the X-ray projection image and the tomographic image of a bentonite sample used in this study are shown in Fig. 2.

2.3. Deformation analysis

The local displacement of the solid phase caused by swelling can, in principle, be found by comparing the tomographic images of the reference state and each of the partially wetted states of the sample, provided that both images contain enough tractable details. To facilitate such analysis with the present quite homogeneous purified bentonite material, the samples were doped with small amount of tracer particles, as discussed above. In addition to displacement due to swelling, intake of water in the sample causes changes in the local X-ray attenuation coefficient and thus in grayscale values in the tomographic image of wetted states. While this phenomenon allows estimation of water content (see below) it has an unwanted side effect of hampering the analysis of local displacements by image correlation techniques. Further improvement can be achieved by normalizing each tomographic image prior to displacement analysis by dividing it, voxel by voxel, by a

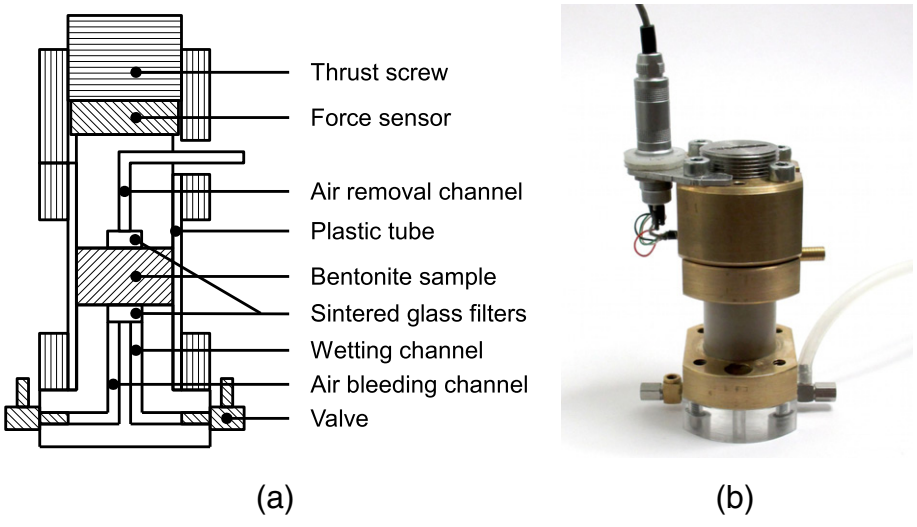

Fig. 1. Schematic illustration (a) and a photographic image (b) of the sample holder.

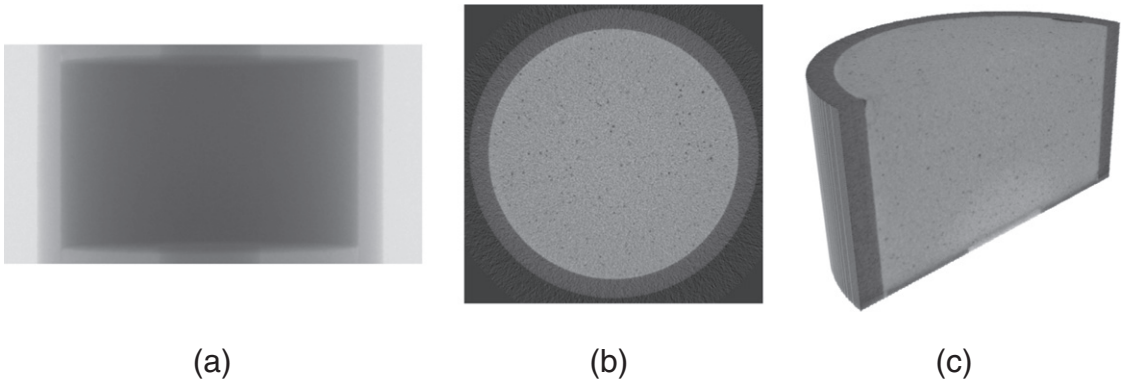

Fig. 2. Single X-ray projection image (a), reconstructed horizontal slice (b) and three-dimensional volume image (half a sample) (c) of a cylindrical bentonite sample. The reconstructed images also show a section of the plastic sample holder tube.

suitably 3D mean filtered version of the same original image. The effect of this procedure to image quality is illustrated in Fig. 3.

The displacement vectors are determined in a three-dimensional grid defined in the reference state image. At every point of that grid, a control subimage, extracted from the normalized reference state image, is shifted voxel by voxel in the vicinity of the grid point and subtracted from its counterpart subimage in a normalized wetted state image. For each shift, the value of a penalty function defined as the sum of squares of the difference is calculated. The shift corresponding to the absolute minimum of the penalty function gives the first estimate for the displacement vector with a precision of one grid unit (voxel). A refined estimate for the displacement is then determined by fitting a second order polynomial function to the values of the penalty function at the location of penalty function minimum and its 26 nearest neighbors. The final displacement vector is then defined as the difference between position of the absolute minimum of this polynomial function and the original grid point. This refined block matching algorithm appears efficient and adequate for the present case where the deformation is relatively small and the added tracer particles facilitate image correlation. Application to other materials and deformation states may require using more advanced 3D image correlation algorithms for displacement analysis.

Given the measured displacement vector field $\vec{u}_s = \vec{u}_s(\vec{r})$, the experimental relative partial density change of the solid phase material point between the reference state and the deformed state with finite deformations is given by

$$\Delta\rho_s\left(\vec{r}\right) = -\rho_{s0}\left(\vec{r}\right)\frac{\delta\left(\vec{r}\right)}{1+\delta\left(\vec{r}\right)}, \tag{3}$$

where ρ_{s0} is the solid phase partial density in the reference state, $\delta = \nabla\cdot\vec{u}_s$ is the relative volume change and $\vec{r}$ is the location of the material point in the reference state.

In order to test the deformation analysis algorithm, a cylindrical sample was made of two-component liquid rubber material doped with glass tracer particles similarly to the bentonite samples. Also, the shape and size of the rubber test sample were the same as the actual bentonite samples used in experiments. The rubber sample was placed in a material testing stage that allows tomographic imaging of the material under compression or tension, and is equipped with displacement and load sensors (Fig. 4). The cylindrical rubber sample was attached between the piston and the bottom plate of the testing stage so as to prevent lateral spread of the end surfaces. Otherwise, the test condition was unconfined. A reference tomographic image of the sample was taken at zero load. The sample was then compressed axially to total linear strain $\varepsilon \approx -0.035$ thereby inducing deformation into a barrel-like shape, and imaged again in this configuration. The refined block matching algorithm was used to calculate the displacement field between the unloaded reference state and the deformed state. The results, averaged over the azimuthal angle, were compared with a cylindrically symmetric numerical solution for the same set-up obtained by COMSOL software and treating rubber as a linearly elastic material. (A semi-analytical scaling solution for this problem also exists (Watanabe, 1996), but is rather complicated and still involves numerical solution of a differential equation.) It turns out that the only material parameter affecting the shape of the sample in this set-up is Poisson's ratio. Rubber materials are usually considered nearly incompressible with Poisson's ratio close to $\nu \approx 0.5$. Here, the value $\nu = 0.49$ was used for computational reasons. The experimental and numerical displacement fields of the rubber test sample are shown in Fig. 5 indicating very close qualitative and quantitative agreement.

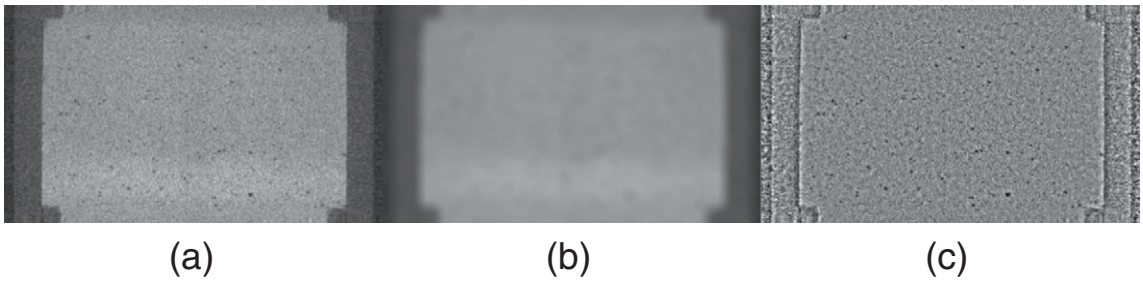

Fig. 3. Normalization of a tomographic image for displacement analysis. The original image (a), the same image blurred by 3D mean filtering (b) and the normalized image, i.e. the original image divided by the filtered image (c).

Fig. 4. Sample holder (SkyScan μCT Material Testing Stage) loaded with a rubber test sample used in validating the displacement analysis algorithm.

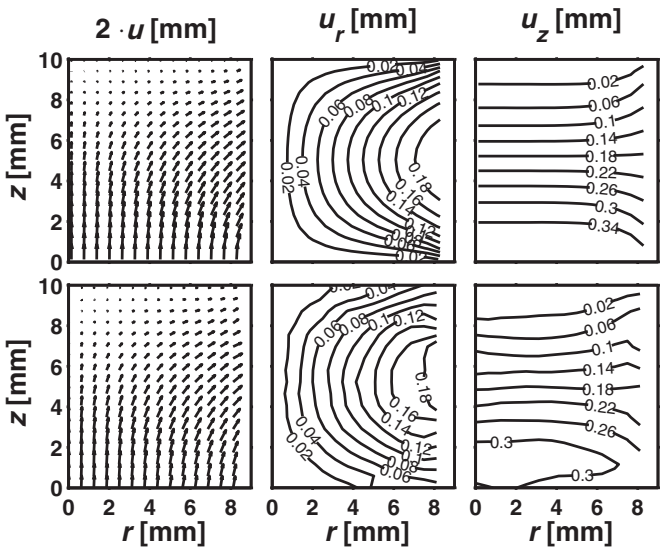

Fig. 5. Numerical solution (COMSOL) for cylindrically symmetric displacement vector field and its radial and axial components of the axially compressed rubber test sample (upper images). The azimuthally averaged experimental result obtained by the refined block matching algorithm from tomographic images of the sample (lower images).

2.4. Water content distribution

As discussed above, an X-ray tomographic image of a heterogeneous material represents the three-dimensional spatial distribution of the linear attenuation coefficient μ in a sample such that the grayscale value $G(\vec{r})$ of a voxel in a given location $\vec{r}$ of the image depends approximately linearly on the LAC value $\mu(\vec{r})$. According to Eq. (2) the grayscale value of each voxel of a tomographic image of partially saturated bentonite sample is thus linearly correlated with the partial densities of solid, water and air in the corresponding location of the sample. In the present case, the effect of presence of air on total attenuation constant can be considered small, and will be neglected. We thus adopt a linear relation between the grayscale value G and the partial densities ρ_s and ρ_w of solid and water phases, respectively, i.e.

$$G = C + \alpha_s \cdot \rho_s + \alpha_w \cdot \rho_w, \tag{4}$$

where C, α_s and α_w are coefficients that may depend on energy spectrum, material composition and various imaging, reconstruction and image post-processing parameters.

The unknown coefficients in Eq. (4) were estimated by gravimetric measurement for an extensive set of calibration samples at varying solid and water content. Of the order of 100 calibration data points were thus collected, a subset of which is shown in Fig. 6. The measured relationship between the partial densities and the grayscale value indeed appears approximately linear in the density range relevant for the present experiment. The fitted values and error limits for coefficients appearing in Eq. (4) are

$$\begin{aligned} C &= 18.9 \pm 3.8 \\ \alpha_s &= 78.5 \pm 2.7\ \mathrm{cm}^3/\mathrm{g} \\ \alpha_w &= 42.8 \pm 2.4\ \mathrm{cm}^3/\mathrm{g}. \end{aligned} \tag{5}$$

Notice that these values are valid only for the tomographic imaging and reconstruction parameter values used in calibration, and the same parameters must be used in actual measurements. Also shown in Fig. 6 are the grayscale values obtained for pure air and for the plastic sample holder tube material (PEEK) found in each tomographic image. This is to monitor and verify stability of the tomographic device during the long imaging period.

Given the three-dimensional tomographic images G and G_0 of the current state and the reference state, respectively, the difference image between the two states is given by

$$\Delta G = G_P - G_0 = \alpha_s \cdot \Delta\rho_s + \alpha_w \cdot \Delta\rho_w. \tag{6}$$

Here, G_P is the pulled-back image of current state created by interpolating image G such that $G_P(\vec{r}) = G(\vec{r} + \vec{u}_s(\vec{r}))$, where $\vec{u}_s(\vec{r})$ is the displacement of a material point located at $\vec{r}$ in the reference state (see Section 2.3). The change of partial density of the water is thus given by

$$\Delta\rho_w = \frac{\Delta G - \alpha_s \cdot \Delta\rho_s}{\alpha_w}, \tag{7}$$

where the change of the solid phase density $\Delta\rho_s$ is given by Eq. (3) for the measured current state displacement field. Finally, the water content in the current state is obtained as

$$\eta = \frac{\rho_w}{\rho_s} = \frac{\rho_{w0} + \Delta\rho_w}{\rho_{s0} + \Delta\rho_s}, \tag{8}$$

where the reference state density of solid and water phases is given by

$$\rho_{s0} = \frac{G_0 - C}{\alpha_s + \eta_0 \alpha_w} \tag{9}$$

$$\rho_{w0} = \eta_0 \rho_{s0}. \tag{10}$$

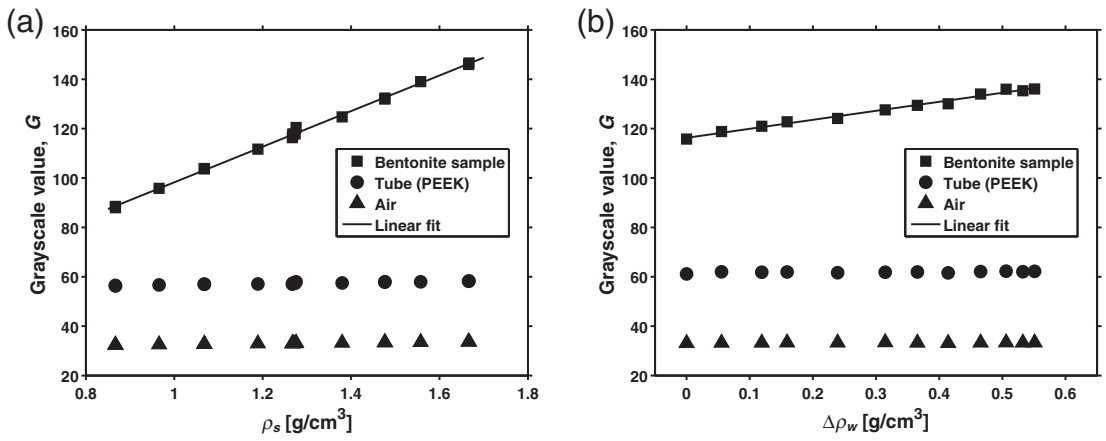

Fig. 6. (a) Average grayscale value of a bentonite sample as a function of average dry density of the solid phase. Each data point corresponds to a different sample made of bentonite powder (with constant initial water content) by compacting it to a desired average solid phase density. (b) Average grayscale value of the sample as a function of average partial density change of water. This data is from a single sample during wetting from initial to fully saturated state. The constant values of the grayscale values of air and PEEK plastic, included in the figures for reference, are indicative of the tomographic device stability between scans.

Here, η_0 is the reference state water content, assumed to be constant.

The tomographic water content analysis method discussed above was compared with results from a straightforward gravimetric analysis of subsamples obtained by slicing a partially wetted test sample. To this end, a dry bentonite sample was first placed in a sample holder with 15 mm sintered plates (see Section 2.2), weighed and imaged to obtain reference state data. The sample was then wetted for 22 h so as to develop an axial water content distribution. After the wetting phase, the sample was again weighed and scanned according to the procedures discussed above. Immediately after the latter scan, the sample was carefully cut horizontally into 10 slices of thickness about 1 mm. The water content of each slice was determined gravimetrically using oven drying at 105 °C. The results obtained from the gravimetric measurement and from the tomographic imaging method are shown in Fig. 7 indicating reasonably good correspondence between the two results in regions well inside the sample. The deviation between the results near the lower and upper end of the test sample most likely arises due to the cone beam reconstruction artifact which tends to mix LAC values between the sample and its surroundings in the vicinity of the horizontal end surfaces of the sample (Valton et al., 2006; Hsieh et al., 2013). Also shown in Fig. 7 is the tomographic analysis result obtained by neglecting the effects of deformation (i.e. assuming $\vec{u}_s = 0$). This result clearly shows the importance of the simultaneous deformation analysis in estimating the water distribution for the present strongly swelling clay material.

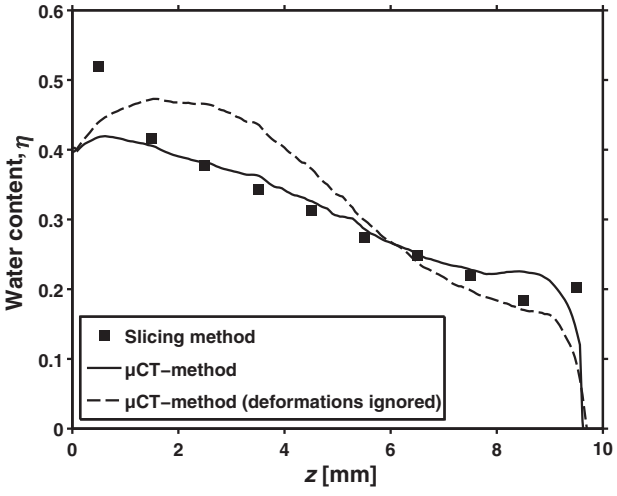

Fig. 7. A comparison of 1D water content distribution measured gravimetrically from sliced bentonite sample and by the tomographic difference image method (Eq. (8)). The latter result is shown including and ignoring the effects of local deformations due to swelling.

3. Results

The X-ray tomographic imaging and image analysis methods described above yield three-dimensional displacement field and water content distributions in the material sample at selected times during the slow wetting process. Typical examples of such results for a bentonite sample wetted in the sample holder chamber with 6 mm sintered plate are visualized in Fig. 8. Fig. 9 shows similar results, but averaged over the azimuthal angle for two experiments with sample holders with 6 mm and 15 mm sintered plates, corresponding to three-dimensional cylindrically symmetric and approximately one-dimensional axial set-up, respectively. Displacement and water content profiles averaged further over the radial direction for the set-up with 15 mm sintered plate are shown in Fig. 10. Finally, the swelling stress measured at the non-wetted end of the samples is shown in Fig. 11. In all results presented here, the average dry density of the samples was 1.2 g/cm^3.

Altogether, the results on displacement distributions obtained by the X-ray tomographic analysis appear consistent and repeatable in the entire sample region. The most important source of error in the deformation analysis is the spurious displacement vector values that occasionally appear as a result of false local minima found by the image correlation algorithm. Such values may contribute to fluctuations visible in the three-dimensional displacement vector field in Fig. 8, but do not seem to have significant contribution to azimuthally averaged results shown in Fig. 9. Notice however, that part of the fluctuation visible in the three-dimensional case may be due to actual inhomogeneity of the solid phase density and water content in the sample. The measured water content distributions and their evolution during the wetting time also appear highly plausible, in general. Near the sample boundaries the results appear impaired, to some extent, e.g. due to reconstruction artifacts arising from conical X-ray beam geometry and from the presence of surfaces with large density gradient (see also Fig. 7). At the beginning of the experiment, the water transport is relatively fast and this may produce some blurring to the images due to the relatively long imaging time characteristic of the used tomographic scanner. Although not necessarily significant from the point of view of the quality of individual images, these effects can decrease the accuracy of the water content analysis based on small differences in the grayscale value of the reference and current images.

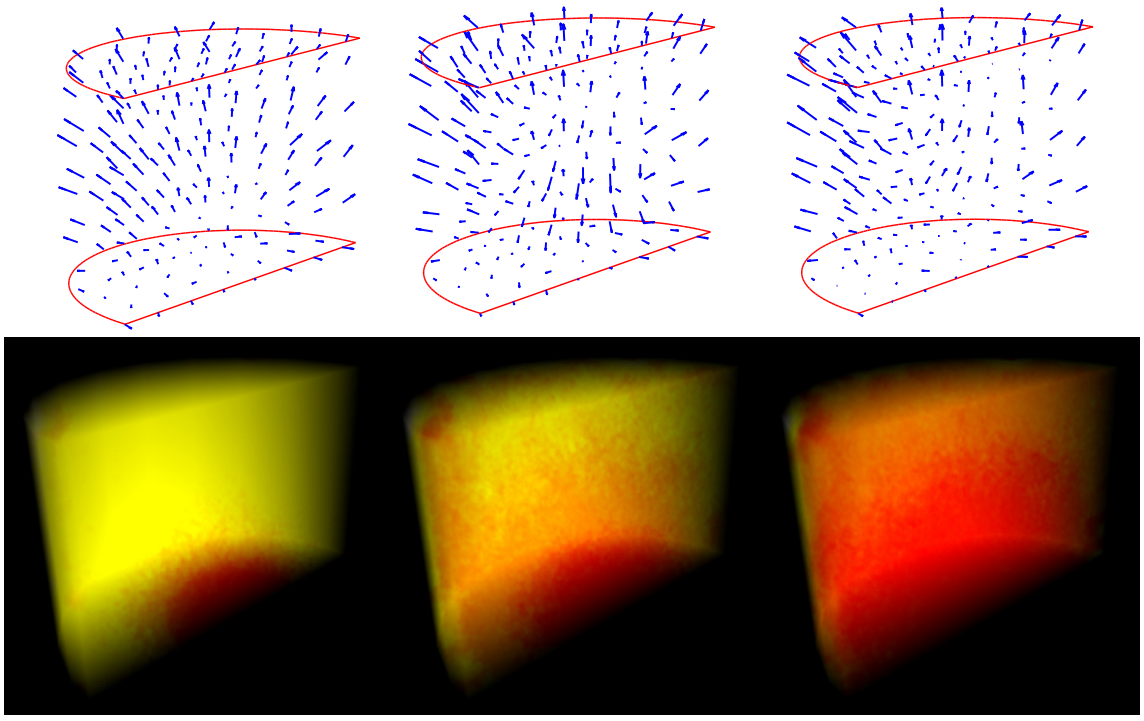

Fig. 8. Three-dimensional visualization of displacement field (upper images) and water content distributions (lower images) at wetting times of 7 h, 25 h and 71 h, for half a sample (see Fig. 2(c)) in a sample holder with 6 mm sintered plate. The displacement vectors are shown scaled by a factor of 10. The color code for water content is qualitatively same as in Fig. 9.

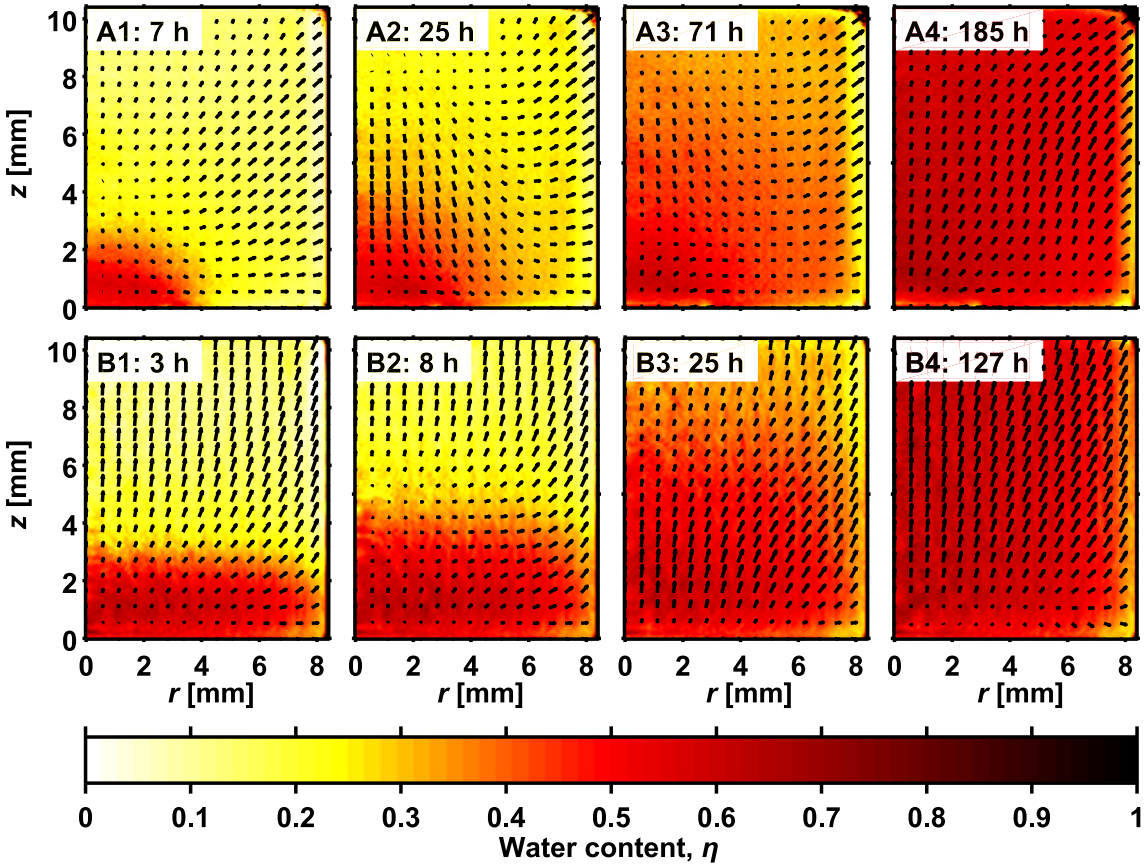

Fig. 9. Water content and displacement vector fields averaged azimuthally for two different wetting geometries with 6 mm and 15 mm diameter sintered plates, labeled as A and B, respectively. The displacement vectors are drawn scaled by a factor of 5. The wetting times are indicated in the image labels.

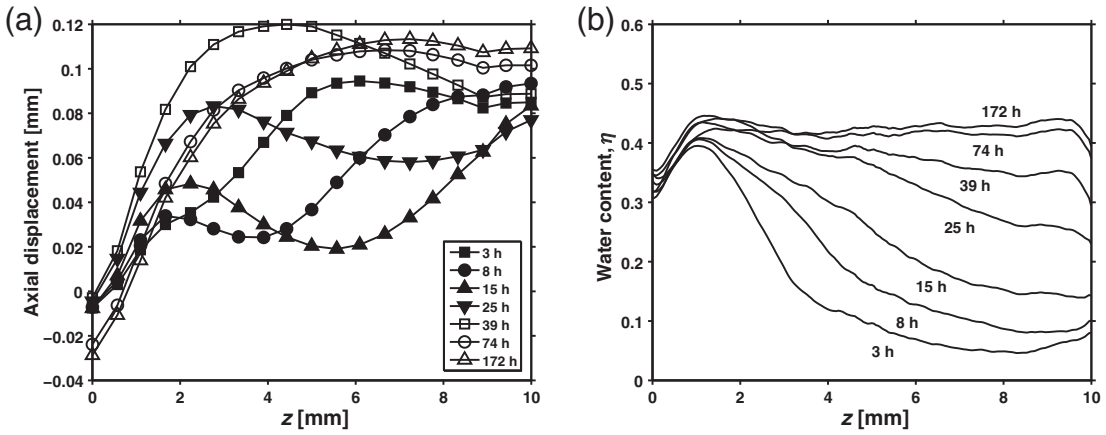

Fig. 10. Evolution of the averaged axial displacement (a) and water content profiles (b) for a bentonite sample wetted in the sample holder with 15 mm sintered plate.

Another experimental issue affecting the accuracy of water content measurement is the incomplete stability of the X-ray source and detector. For accurate results, very good stability is required during each individual scan and between the scans during the experiment, lasting typically up to 2 weeks in the present case. The effects of the intensity variations observed in practice were partially corrected by the standard flat field corrections performed separately for each scan. However, the minor temporal instability inherent in the device does contribute to the error in the measured water content. Although, lacking an applicable reference method, quantitative assessment of absolute errors of both the local displacement and the local water content analyses is not feasible, the overall confidence level of the results is reflected by the deformation and wetting test cases, the results of which are shown in Figs. 5 and 7.

In order to minimize total attenuation of the X-ray beam, plastic materials were used in the sample holder. Furthermore, the thickness of the sample holder tube was relatively low. The high swelling stress generated by the sample was thereby able to induce small elastic strain in the sample holder both in radial and axial directions. Consequently, the volume and the shape of the sample do not remain exactly constant during the experiments, as indicated by the measured displacement vectors near the sample surfaces. This, however, is not detrimental for the intended use of the data in validating models for water transport and solid phase deformation, as the location of the sample boundaries at each instant of time can also be estimated from the tomographic images.

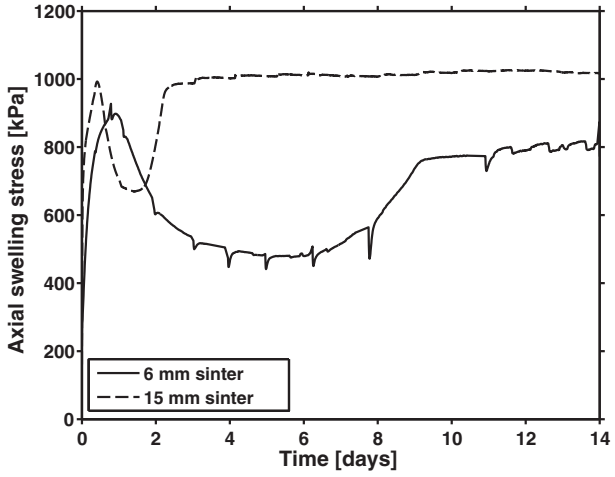

Fig. 11. Axial swelling stress measured from non-wetted end of the sample holder as a function of wetting time for two bentonite samples wetted through 6 mm and 15 mm sintered plates. The notches visible especially in the curve corresponding to the 6 mm sintered plate arise due to repeated short interruptions of wetting for X-ray tomographic imaging.

Some qualitative observations concerning the inherently quite complicated process of wetting and swelling of bentonite in a confined conditions can already be made based on the measured data visualized in Figs. 8 through 11. Firstly, in the present set-up where no external water pressure was used, wetting does not seem to take place as a well defined wetting front that would be characteristic to e.g. simple capillary action. Instead, the observed water transport mechanism resembles diffusion which, however, may not be of a simple linear type. Secondly, in the initial phase of wetting, the material is first pushed away from the wetted zone, apparently due to rapid swelling near the water entrance region. At intermediate times however, the direction of displacements can be inverted in parts of the sample volume such that the total movement can be towards the water entrance region. As the material approaches its final saturated state, the displacement field again becomes more homogeneous and unidirectional. A plausible explanation for this rather complicated behavior is provided by collapse (leading to decrease of porosity) of the material at intermediate values of water content. This phenomenon is also indicated by the axial swelling stress measured at the non-wetting end of the sample (see Fig. 11), showing a typical behavior of stress build-up with a temporary decrease of stress after initial rapid increase followed by final increase towards saturation value (Nishimura et al., 2012). However, in view of the X-ray tomographic results shown in Fig. 9, it is obvious that interpretation of the measured evolution of the axial stress in terms of material swelling properties is not quite straightforward. The mean axial stress measured at one end of the sample is affected by combined effects of inhomogeneous local wetting and stress–strain history, and most likely also by frictional stress between the sample and the sample holder surfaces. More thorough analysis of the results obtained by the experimental methods developed here will be presented elsewhere.

4. Conclusions

A method for simultaneous non-intrusive analysis of three-dimensional deformation and water transport in solid, wetting material, based on X-ray tomographic imaging has been introduced. The material is assumed to consist of three components: solid, water and gas that are homogeneously distributed in the scale of imaging resolution. The attenuation of X-rays in the gas phase is neglected. The analysis is based on comparing the tomographic images of the reference state and of a wetted and deformed state. The displacement field is obtained by a straightforward image correlation method. This requires that a sufficient amount of local details, identifiable in the two images, are found in both states, and that the imaging resolution is sufficient for revealing

the deformations. The deformation analysis was successfully compared with numerical solution for a rubber test sample under axial compression. The analysis of water content is based on the local grayscale value differences between the reference state and the wetted state. It utilizes the measured deformation field to compute changes of the solid phase partial density from the reference state. The method requires calibration with samples with known solid and water content. The water content analysis was compared with gravimetric results from axially wetted and sliced cylindrical bentonite samples. The results showed relatively good accuracy in the interior parts of the sample, but considerable error near both end boundaries of the sample. A plausible source of this error is the conical X-ray beam geometry and the rather simple standard algorithm used for tomographic image reconstruction.

The methods were applied here in a 4D study (three spatial dimensions and time) of wetting and swelling deformation of a purified sodium bentonite doped with small glass tracer particles, and wetted with a synthetic groundwater of salinity 0.26 g/l. The results appear qualitatively correct and plausible, and provide valuable information for e.g. validation of models involving transport of water and the resulting swelling deformation of bentonite. Further analysis of the experimental results and comparison with model predictions are left for a future work.

While the primary motivation and field of application in this work have been the study of the hydromechanical properties and swelling of bentonite, the developed method is potentially applicable in also other materials and processes involving liquid transport and deformation. This may include wetting/swelling and drying/shrinking of various materials provided that they contain sufficient amount of local inhomogeneities to allow for displacement analysis, and that the presence of water in the material is observable by X-ray imaging technique.

Acknowledgments

This work was funded by the Finnish Research Programme on Nuclear Waste Management KYT2014 through the project “Assessment of bentonite characteristics (BOA)”. The authors appreciate the contribution by Pirkko Hölttä (University of Helsinki, Laboratory of Radiochemistry) who provided the synthetic groundwater used in the wetting experiments.

References

Anderson, S.H., Gantzer, C.J., Boone, J.M., Tully, R.J., 1988. Rapid nondestructive bulk density and soil-water content determination by computed tomography. Soil Sci. Soc. Am. J. 52, 35–40.

Aregawi, W., Defraeye, T., Saneinejad, S., Vontobel, P., Lehmann, E., Carmeliet, J., Derome, D., Verboven, P., Nicolai, B., 2013. Dehydration of apple tissue: intercomparison of neutron tomography with numerical modelling. Int. J. Heat Mass Transf. 67, 173–182.

Barrett, J.F., Keat, N., 2004. Artifacts in CT: recognition and avoidance. Radiographics 24, 1679–1691.

Bart-Smith, H., Bastawros, A.F., Mumm, D.R., Evans, A.G., Sypeck, D.J., Wadley, H.N.G., 1998. Compressive deformation and yielding mechanisms in cellular Al alloys determined using X-ray tomography and surface strain mapping. Acta Mater. 46, 3583–3592.

Carmeliet, J., Roels, S., 2001. Determination of the isothermal moisture transport properties of porous building materials. J. Build. Phys. 24, 183–210.

Gardner, C.M.K., Robinson, D., Blyth, K., Cooper, J.D., 2000. Soil water content. Soil and Environmental Analysis: Physical Methods. CRC Press, pp. 1–64.

Herrmann, K.H., Pohlmeier, A., Gembris, D., Vereecken, H., 2002. Three-dimensional imaging of pore water diffusion and motion in porous media by nuclear magnetic resonance imaging. J. Hydrol. 267, 244–257.

Hsieh, J., Nett, B., Yu, Z., Sauer, K., Thibault, J.B., Bouman, C.A., 2013. Recent advances in CT image reconstruction. Curr. Radiol. Rep. 1, 39–51.

Hubbell, J.H., Seltzer, S.M., 1996. Tables of X-ray Mass Attenuation Coefficients and Mass Energy-Absorption Coefficients. National Institute of Standards and Technology.

Huisman, J.A., Hubbard, S.S., Redman, J.D., Annan, A.P., 2003. Measuring soil water content with ground penetrating radar. Vadose Zone J. 2, 476–491.

Huitti, T., Hakanen, M., Lindberg, A., 1998. Sorption of Cesium on Olkiluoto Mica Gneiss, Granodiorite and Granite. Posiva Oy.

Meinzer, F.C., 2002. Co-ordination of vapour and liquid phase water transport properties in plants. Plant Cell Environ. 25, 265–274.

Moldrup, P., Olesen, T., Komatsu, T., Schjønning, P., Rolston, D.E., 2001. Tortuosity, diffusivity, and permeability in the soil liquid and gaseous phases. Soil Sci. Soc. Am. J. 65, 613–623.

Mukhlisin, M., Saputra, A., El-Shafie, A., Taha, M.R., 2012. Measurement of dynamic soil water content based on electrochemical capacitance tomography. Int. J. Electrochem. Sci. 7.

Nishimura, T., Koseki, J., Matsumoto, M., 2012. Measurement of swelling pressure for bentonite under relative humidity control. Unsaturated Soils: Research and Applications. Springer, pp. 235–240.

Orteu, J.J., 2009. 3-D computer vision in experimental mechanics. Opt. Lasers Eng. 47, 282–291.

Peth, S., Nellesen, J., Fischer, G., Horn, R., 2010. Non-invasive 3D analysis of local soil deformation under mechanical and hydraulic stresses by CT and digital image correlation. Soil Tillage Res. 111, 3–18.

Riedel, I., Andò, E., Salager, S., Bésuelle, P., Viggiani, G., 2012. Water retention behaviour explored by X-ray CT analysis. Unsaturated Soils: Research and Applications. Springer, pp. 81–88.

Saguy, I.S., Marabi, A., Wallach, R., 2005. New approach to model rehydration of dry food particulates utilizing principles of liquid transport in porous media. Trends Food Sci. Technol. 16, 495–506.

Sammartino, S., Michel, E., Capowiez, Y., 2012. A novel method to visualize and characterize preferential flow in undisturbed soil cores by using multislice helical CT. Vadose Zone J. 11.

Soo, S.L., 1990. Multiphase Fluid Dynamics. Science Press, Beijing, China.

Stock, S.R., 2008. Microcomputed Tomography: Methodology and Applications. CRC press.

Tippkötter, R., Eickhorst, T., Taubner, H., Gredner, B., Rademaker, G., 2009. Detection of soil water in macropores of undisturbed soil using microfocus X-ray tube computerized tomography (μCT). Soil Tillage Res. 105, 12–20.

Valton, S., Peyrin, F., Sappey-Marinier, D., 2006. Analysis of cone-beam artifacts in off-centered circular CT for four reconstruction methods. Int. J. Biomed. Imaging 2006.

Watanabe, S., 1996. Elastic analysis of axi-symmetric finite cylinder constrained radial displacement on the loading end. Struct. Eng. Earthq. Eng. 13, 175–186.

Wildenschild, D., Hopmans, J.W., Rivers, M.L., Kent, A.J.R., 2005. Quantitative analysis of flow processes in a sand using synchrotron-based X-ray microtomography. Vadose Zone J. 4, 112–126.

Zou, W., Hunter, N., Swain, M.V., 2011. Application of polychromatic μCT for mineral density determination. J. Dent. Res. 90, 18–30.

P2

TIME-RESOLVED X-RAY MICROTOMOGRAPHIC MEASUREMENT OF WATER TRANSPORT IN WOOD-FIBRE REINFORCED COMPOSITE MATERIAL

by

Miettinen A, Harjupatana T, Kataja M., Fortino S., and Immonen K. 2016

IOP Conf. Series: Materials Science and Engineering 139 (2016) 012037

https://doi.org/10.1088/1757-899X/139/1/012037

IOP Conf. Series: Materials Science and Engineering **139** (2016) 012037 doi:10.1088/1757-899X/139/1/012037

Time-resolved X-ray microtomographic measurement of water transport in wood-fibre reinforced composite material

Arttu Miettinen[1], Tero Harjupatana[1], Markku Kataja[1], Stefania Fortino[2], Kirsi Immonen[2]

[1] University of Jyväskylä, Department of Physics, P.O. Box 35 (YFL) FI-40014 Jyväskylä, Finland
[2] VTT Technical Research Centre of Finland, P.O. Box 1000, FI-02044 VTT, Finland

E-mail: arttu.miettinen@phys.jyu.fi

Abstract. Natural fibre composites are prone to absorb moisture from the environment which may lead to dimensional changes, mold growth, degradation of mechanical properties or other adverse effects. In this work we develop a method for direct non-intrusive measurement of local moisture content inside a material sample. The method is based on X-ray microtomography, digital image correlation and image analysis. As a first application of the method we study axial transport of water in a cylindrical polylactic acid/birch pulp composite material sample with one end exposed to water. Based on the results, the method seems to give plausible estimates of water content profiles inside the cylindrical sample. The results may be used, *e.g.*, in developing and validating models of moisture transport in biocomposites.

1. Introduction

Natural fibre composites appear as a promising and environmentally friendlier alternative for, *e.g.*, engineering plastics and glass fibre reinforced composites [1]. A main challenge with many natural-fibre reinforced thermoplastic composites is their inherent tendency to absorb water. This may lead to fungal decay, mold growth, mechanical degradation and dimensional instability, and thereby to, *e.g.*, decreased service life [1, 2]. A key topic in development of improved natural fibre composites is thus understanding the influence of moisture on the properties of the material, in particular if the material is to be used in variable environmental conditions.

Measuring time-dependent three-dimensional moisture content field inside material is a non-trivial task, especially for heterogeneous materials that contain multiple phases. In this work we present a method for measuring one-dimensional time-dependent water content profile based on three-dimensional X-ray microtomographic images. The method is based on first using 3D digital image correlation for measuring the displacement field of the wetted and possibly swollen sample. The local water content is then found by measuring the change in the values of the effective X-ray attenuation coefficient for each material point (3D image voxel) between the dry state and the wetted and deformed state.

Previously, several authors have used various methods based on X-ray tomography to determine local moisture content in different kinds of materials like stone, clothing and wood [3–6]. In many of those works the effects of swelling deformation of the material has not been

considered, or is included by making a specific assumption on the deformation characteristics of the material. Other possible methods for measuring local water concentration, based on sensing local amount of hydrogen nuclei in the material, are neutron radiography [7, 8] and magnetic resonance imaging [9].

A method similar to the one introduced in this paper was recently published and used for measuring water content in an approximately 2 cm wide bentonite clay sample [10]. Application of the method to smaller and less-absorbing composite material samples poses several problems in sample preparation, imaging and image analysis. Here, we demonstrate its practical application on a cylindrical polylactic acid/birch pulp composite material sample of diameter 2 mm. The experimental set-up was designed to yield one-dimensional axial wetting. Finally, the feasibility of the method is assessed based on the results from this first trial experiment.

2. Method for analysing moisture content distribution using X-ray tomography

We start by considering a composite material sample at known low water content, called the 'dry state' of the sample, in what follows. An X-ray tomographic image of the dry sample, denoted by $\mu^0_{\text{eff}}(\vec{x})$, $\vec{x} \in C \subset \mathbb{R}^3$, represents a three-dimensional map of the effective X-ray attenuation coefficient indicating the original reference configuration of the sample. Subjecting the sample to a moist environment initiates absorption of water and deformation due to swelling. Assuming that the absorption process is slow enough so that the state of the sample can be assumed approximately stationary within the tomographic scanning time used, we can take another X-ray tomographic image of the partially wetted sample during the wetting process. This image, denoted by $\mu_{\text{eff}}(\vec{x})$ now represents the wetted and deformed configuration of the sample. The task is now to find the distribution of water content of the wet state and express it in the reference frame defined by the dry sample.

To this end, we first estimate the displacement field $\vec{u}(\vec{x}) = (u_1(\vec{x}), u_2(\vec{x}), u_3(\vec{x}))$ between the dry state and the wet/deformed state using the images μ^0_{eff} and μ_{eff} representing these two states. Assuming that the swelling strain is small enables using a simple block-matching algorithm to find the displacement field. The algorithm is based on comparing displaced subregions of the wet state image to non-displaced subregion of the dry state image and minimizing the squared difference with respect to displacement, *i.e.*

$$\vec{u}(\vec{x}) = \text{argmin}_{\vec{u}' \in S} \sum_{\vec{y} \in W} (\mu_{\text{eff}}(\vec{y} + \vec{u}') - \mu^0_{\text{eff}}(\vec{y}))^2, \tag{1}$$

where S is a neighbourhood of origin and W is a neighbourhood of $\vec{x}$. The set S determines the possible values of the displacement and the set W gives the size of the subregion where the two images are compared.

For given displacement field $\vec{u}(\vec{x})$, a back-projected image of the wet state image is defined by

$$\mu^P_{\text{eff}}(\vec{x}) = \mu_{\text{eff}}(\vec{x} + \vec{u}(\vec{x})). \tag{2}$$

The image $\mu^P_{\text{eff}}(\vec{x})$ thus contains the values of attenuation coefficient of wet state material points associated with the original dry state positions of the same material points.

In addition to local change of partial density[1] of water ρ_w, wetting generally induces deformation and can therefore lead to local change of composite material (solid phase) partial density ρ_c, too. As the presence of both water and solid material contribute to local X-ray attenuation, the change in the water content can not be deduced based on the measured change of the local value of the X-ray attenuation coefficient alone. The necessary additional information

[1] Partial density of component α of a mixture is defined as $\rho_\alpha = m_\alpha / V$, where m_α is the mass of component α contained in volume V of the mixture.

can, however, be obtained utilizing the displacement field $\vec{u}(\vec{x})$ and using conservation of mass of the composite material. The change of ρ_c between the dry state and the wet state is thereby found to be

$$\Delta\rho_c(\vec{x}) = -\rho_c^0(\vec{x})\frac{\delta(\vec{x})}{1+\delta(\vec{x})}, \tag{3}$$

where $\rho_c^0(\vec{x})$ is the density of the composite material in the dry state, and

$$\delta(\vec{x}) = \nabla \cdot \vec{u}. \tag{4}$$

The local value of attenuation coefficient of X-rays can be assumed to depend linearly on local densities ρ_c and ρ_w in the wet composite material [11]. We thus write

$$\mu_{\text{eff}} = \alpha_c\rho_c + \alpha_w\rho_w, \tag{5}$$

where α_c and α_w are X-ray mass attenuation coefficients of the composite material and water, respectively (for the composite material, α_c is the mass averaged attenuation coefficient of its component materials). The coefficients α_c and α_w are unknown a priori and must be found by calibration measurements. The difference of the effective X-ray attenuation coefficient between the back-projected wet state and the dry state is given in the dry state reference frame by

$$\begin{aligned}\Delta\mu_{\text{eff}}(\vec{x}) &= \mu_{\text{eff}}^P(\vec{x}) - \mu_{\text{eff}}^0(\vec{x}) &(6)\\ &= \alpha_c(\rho_c^P(\vec{x}) - \rho_c^0(\vec{x})) + \alpha_w(\rho_w^P(\vec{x}) - \rho_w^0(\vec{x})) &(7)\\ &= \alpha_c\Delta\rho_c(\vec{x}) + \alpha_w\Delta\rho_w(\vec{x}), &(8)\end{aligned}$$

where $\Delta\rho_w(\vec{x})$ is the change of the partial density of water between the reference and the wet states (local change of water content of a composite material point located originally at $\vec{x}$). Solving for $\Delta\rho_w(\vec{x})$ gives

$$\Delta\rho_w(\vec{x}) = \frac{\Delta\mu_{\text{eff}}(\vec{x}) - \alpha_c\Delta\rho_c(\vec{x})}{\alpha_w}. \tag{9}$$

Finally, assuming that the amount of residual water present in the dry state can be neglected, the partial densities of composite material and water in the wet state are given (again, in the dry state reference frame) by

$$\begin{aligned}\rho_c(\vec{x}) &= \rho_c^0(\vec{x}) + \Delta\rho_c(\vec{x}) = \frac{\mu_{\text{eff}}^0(\vec{x})}{\alpha_c} + \Delta\rho_c &(10)\\ \rho_w(\vec{x}) &= \Delta\rho_w(\vec{x}). &(11)\end{aligned}$$

3. Test case – polylactic acid/birch pulp composite material

The method discussed above was tested with polylactic acid/birch pulp composite material. The polylactic acid was Natureworks Ingeo 3001D polymer with MFI 22 and the birch pulp was provided by Metsä Fibre. The fibres and the matrix were compounded with a twin screw compounder and injection moulded to a dog bone shaped tensile test specimen containing 40 % fibre by mass. A cylindrical sample of 1.9 mm diameter was cut from the central part of the tensile test specimen using a high-precision milling machine. Care was taken not to damage the intact surface of the sample through which the water infiltration was to take place. The sample was glued on the top of a sample holder made of 1.9 mm diameter carbon fibre rod (see figure 1).

To construct a water chamber, the sample was placed and sealed in a long thin-walled polyethylene terephthalate (PET) tube with wall thickness ∼6.35 µm and inner diameter 1.98 mm (Vention Medical, United States). The gap between the sample and the tube inner wall was filled with cyanoacrylate glue that was drawn into the gap by capillary action. The

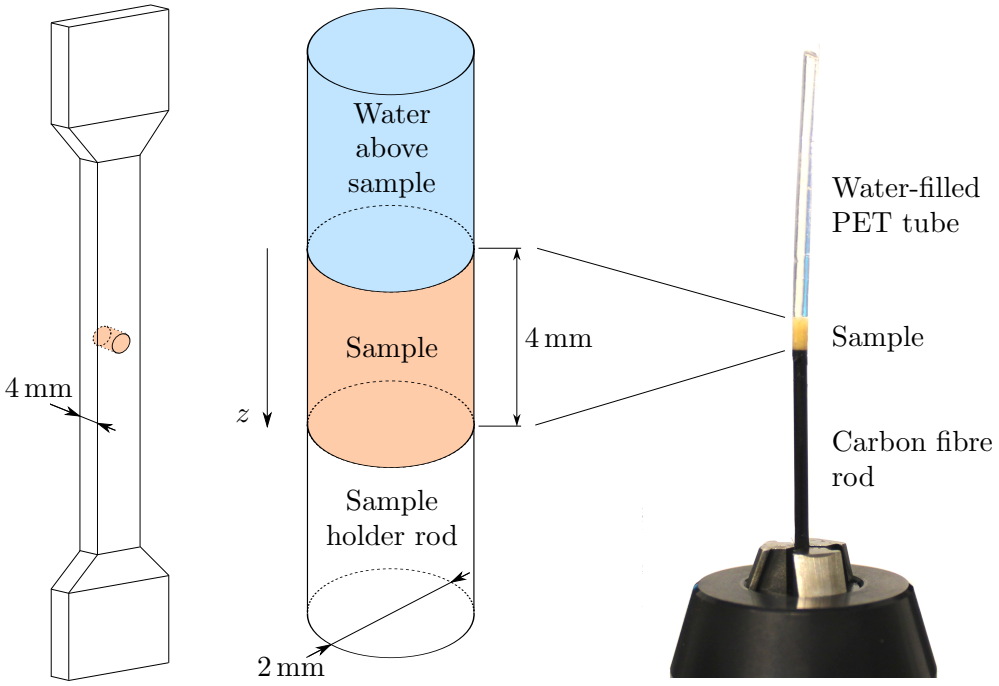

Figure 1. Schematic representation of sample location and orientation with respect to a tensile test specimen (left). The shaded part is the sample. The structure of the sample assembly (middle). Photograph of the realization of the sample assembly (right). The various diagrams are not drawn to scale.

diameter of the final sample, including the PET tube, is approximately 2 mm and its height is approximately 4 mm. The geometry and materials of the sample assembly, shown in figure 1, were selected to allow one-dimensional axial infiltration of water and as free swelling of the sample as possible during the wetting phase of the experiment.

After oven drying in 50°C for 24 h, the sample was imaged using Xradia microCT-400 device with 4.74 µm pixel size, 30 kV acceleration voltage and 3 W electron beam power. Total of 1129 projection images were acquired with 5 s exposure time, totalling in 3.5 h scan time. With the given settings the field-of-view of the tomographic image spans a cylinder of 2.2 mm diameter and height. The entire sample assembly can thus be kept within the field-of-view of the scanner in the radial direction, which is one of the basic requirements for faithful reconstruction of the sample. In the axial direction (z-direction in figure 1) three overlapping sub-scan tomograms had to be acquired to fit the whole 4 mm long sample into the combined field-of-view of the three images. For calibration purposes (see below) the combined image area was selected such that a part of the sample holder rod and a part of the water chamber were visible below and above the sample, respectively. The procedure thus yielded the dry state image $\mu^0_{\mathrm{eff}}(\vec{x})$ for each sub-scan region, see figure 2.

Wetting of the sample was initiated by adding water into the water chamber using a syringe and a needle mounted on a special stage that ensured controlled injection. Immediately after that, acquisition of the three sub-scan images sequentially with predetermined intervals was commenced. The intervals varied from 12 h in the beginning to one week at the end of the wetting process. The total duration of the process was 135 days.

After reconstruction and beam-hardening correction done using the standard utility software of the tomographic scanner, the images were found to contain relatively weak ring artefacts that are typically caused by spatial variation of the X-ray detector properties over its sensitive area.

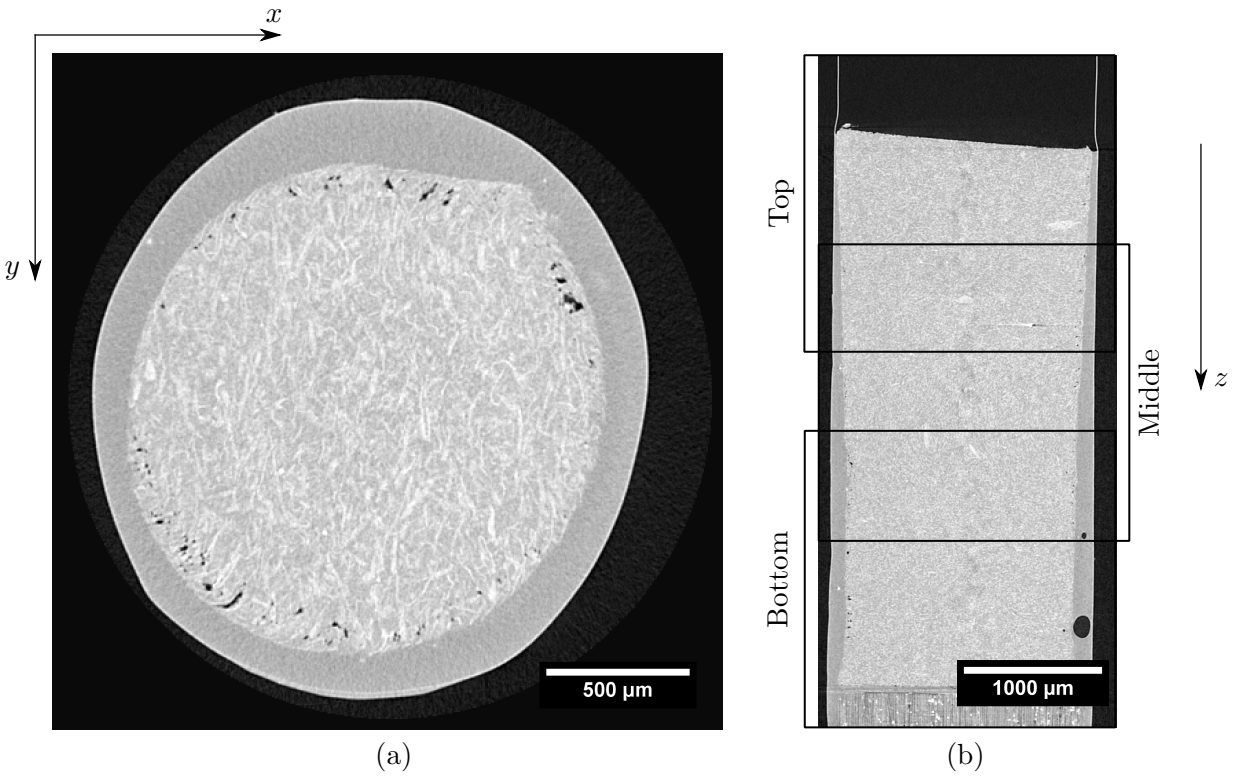

Figure 2. (a) A single horizontal slice of a tomographic image of the dry sample. The thin bright region on the edge of the sample is the PET tube, thick gray part is cyanoacrylate glue, bright small regions are parts of wood fibres and black holes near the edge of the sample are pores caused by milling. (b) A vertical slice of the dry sample showing the three overlapping sub-scan regions. The combined image includes a part of the carbon fibre sample holder rod visible in the bottom of the image and the lower part of the (empty) water chamber.

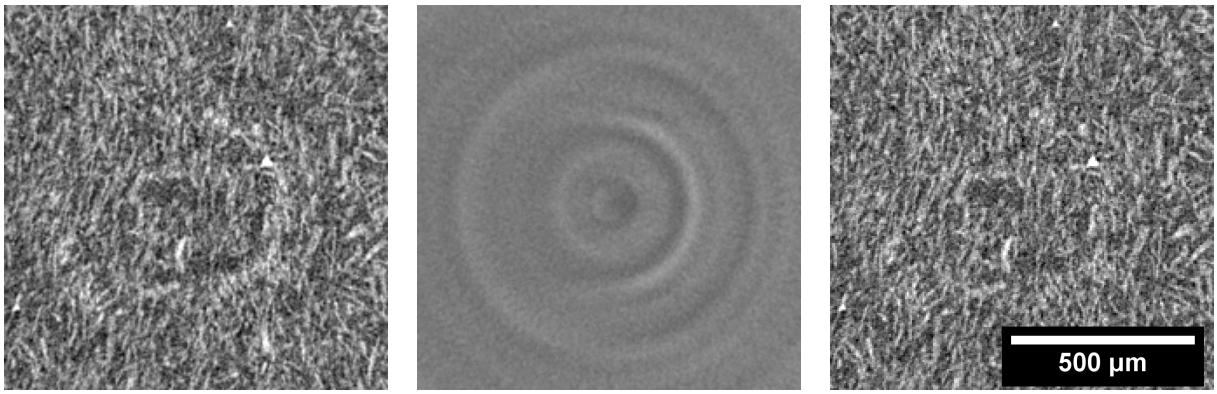

Figure 3. Removal of ring artefacts: A horizontal slice of an original image with notable ring artefact (left), of the normalization image produced as an average of 20 images of a homogeneous phantom sample (middle) and of a final corrected image (right). The scale bar applies to all the three images.

In order to alleviate the effect of ring artefacts in the final results, a phantom sample was made of highly homogeneous poly(methyl methacrylate) rod of diameter 2 mm, and imaged 20 times using the same settings as for the composite sample. The average image of these 20 images, containing virtually but the ring artefacts, was then used to normalize the original tomographic images thereby removing most of the ring artefacts (see figure 3).

We denote the sequence of final corrected images for a selected sub-scan region by $\mu_{\text{eff}}(j, \vec{x})$, where $j = 1, \ldots, N$ is the scan index such that $\mu_{\text{eff}}(1, \vec{x})$ is the image taken immediately after water injection at time $t = 0$ and $\mu_{\text{eff}}(N, \vec{x})$ is the image of the sample in its final state at time $t = 135$ days. The displacement fields $\vec{u}(j, \vec{x})$ between the dry state image $\mu^0_{\text{eff}}(\vec{x})$ and the wet state images $\mu_{\text{eff}}(j, \vec{x})$ were then found using equation (1). All the images were transformed into the reference frame of the corresponding dry state using equation (2) thus yielding images $\mu^P_{\text{eff}}(j, \vec{x})$. Spatial averages of $u_3(j, \vec{x})$ and $\mu^P_{\text{eff}}(j, \vec{x})$ over horizontal (x-y) sections of the sample were calculated for each value of the distance from the upper surface of the sample z, yielding the vertical profile of vertical displacement $u_3(j, z)$, and of attenuation coefficient $\mu^P_{\text{eff}}(j, z)$, respectively. The results from each sub-scan section were then patched together using linearly weighted interpolation within the sub-scan overlap regions, thereby forming the corresponding vertical profiles over the entire sample height.

The calibration constant α_w was obtained by

$$\alpha_w = \frac{\langle \mu_{\text{eff}}(1, z) \rangle_w}{\tilde{\rho}_w}, \tag{12}$$

where $\langle \cdot \rangle_w$ denotes average over part of the data corresponding to the region above the sample, containing solely water. The density of water was taken to be $\tilde{\rho}_w = 1000\,\text{kg/m}^3$. Similarly, the calibration constant α_c was obtained by

$$\alpha_c = \frac{\langle \mu^0_{\text{eff}}(z) \rangle_c}{\tilde{\rho}_c}, \tag{13}$$

where $\langle \cdot \rangle_c$ denotes average over the volume of the dry state sample. The density of the dry composite material was measured using a straightforward gravimetric method resulting in $\tilde{\rho}_c = (1280 \pm 20)\,\text{kg/m}^3$. The initial partial density of the composite material was set to

$$\rho^0_c(z) = \frac{\mu^0_{\text{eff}}(z)}{\langle \mu^0_{\text{eff}}(z) \rangle_c} \tilde{\rho}_c. \tag{14}$$

Finally, the partial densities of composite material and water for each j were calculated by substituting $u_3(j, z)$, $\mu^0_{\text{eff}}(z)$, $\mu^P_{\text{eff}}(j, z)$, α_c, α_w and $\rho^0_c(z)$ into Equations 3 – 11. As the final result, the measured evolution of water content in the sample is shown in figure 4.

4. Discussion and conclusions

A method for non-destructive quantitative measurement of time-dependent water content profile inside a composite material sample set in contact with water was introduced and applied to polylactic acid/birch pulp composite. The experimental set-up was designed to allow one-dimensional axial infiltration of water in a cylindrical composite material sample. As a result, measured water content profiles inside the sample were obtained at various times of wetting.

The method requires careful calibration and correction of various artefacts and sources of error inherent in X-ray tomographic techniques. In general, the measured water content profiles obtained in this preliminary study, shown in figure 4, appear qualitatively plausible and resemble those expected for a diffusive transport process, although not necessarily of simple linear form. In some of the measured profiles, anomalous structures appear indicating local deviation from

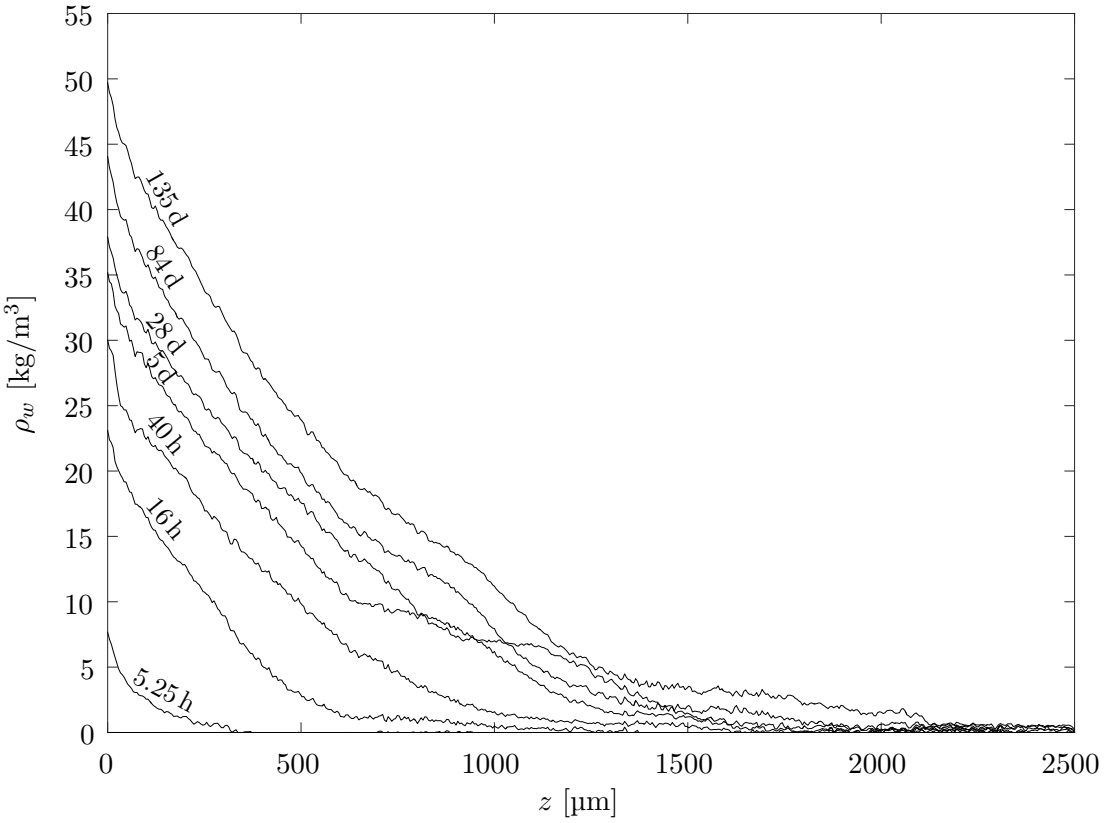

Figure 4. Measured water content profiles in the wood-fibre reinforced composite material sample for various values of wetting time, obtained using X-ray tomographic techniques. The origin of position z is at the surface of the sample exposed to water. For clarity, only a subset of all the measured profiles are shown.

the overall behaviour (see figure 4, near $z = 1000\,\mu\text{m}$). Without further investigation, it is not clear whether these anomalies are due to an error, or whether they arise for a physical reason such as presence of inhomogeneities in the sample.

In this first test of the method, a very small sample was used. This prevented valid independent verification of the results by gravimetric measurements, as done in, *e.g.*, [10]. However, based on the measured integrated water content, the total amount of water absorbed by the sample was somewhat less than expected based on independent gravimetric measurements done using larger samples. This might be due to water diffusing and evaporating through the mantle of the cylindrical sample, in spite of the thin layer of sealing glue and plastic tube. In future experiments larger samples and improved outer surface sealing should be used to facilitate quantitative validation of the method.

The detailed results obtained by the present method are useful in validating absorption models (see, *e.g.*, [12, 13]) and in quantifying the necessary material parameters related to water transport and hydromechanical behaviour of the composites. Although the method was applied here in virtually one-dimensional wetting geometry it can, in principle, be used to measure water content maps in a general three-dimensional case. Such extension of the method is left for future work.

References

[1] Campilho R 2016 *Natural Fiber Composites* (CRC Press)
[2] Joffre T, Wernersson E, Miettinen A, Luengo Hendriks C L and Gamstedt E K 2013 *Composites Science and Technology* **74** 52 – 59
[3] Cai Z 2008 *Forest products journal* **58** 41 – 45
[4] Leonard A, Blacher S, Marchot P, Pirard J P and Crine M 2005 *Canadian journal of chemical engineering* **83**(1) 127 – 131
[5] Ruiz de Argandoña V G, Rodriguez-Rey A, Celorio C, Calleja L and Suárez del Rio L M 2003 *Geological Society Special Publications* **215** 127–134
[6] Weder M, Brühwiler P A and Laib A 2006 *Textile Research Journal* **76** 18–26
[7] Lindsay J T, Matsubayashi M and Islam M N 1994 *Nuclear Instruments and Methods in Physics Research* A **353** 149 – 151
[8] Metwalli E, Hermes H E, Calzada E, Kulozik U, Egelhaaf S U and Muller-Buschbaum P 2016 *Physical Chemistry Chemical Physics* **18**(9) 6458 – 6464
[9] MacMillan M B, Schneider M H, Sharp A R and Balcom B J 2002 *Wood and fiber science* **34** 276 – 286
[10] Harjupatana T, Alaraudanjoki J and Kataja M 2015 *Applied Clay Science* **114** 386 – 394
[11] Stock S R 2009 *Microcomputed tomography* (CRC Press)
[12] Frandsen H L Selected constitutive models for simulating the hygromechanical response of wood
[13] Adhikary K B, Pang S and Staiger M P 2008 *Chemical Engineering Journal* **142** 190 – 198

P3

A METHOD FOR MEASURING WETTING AND SWELLING OF BENTONITE USING X-RAY IMAGING

by

Harjupatana T., Miettinen A., and Kataja M. 2022

Applied Clay Science 221 (2022) 106485

https://doi.org/10.1016/j.clay.2022.106485

Applied Clay Science 221 (2022) 106485

Contents lists available at ScienceDirect

Applied Clay Science

journal homepage: www.elsevier.com/locate/clay

A method for measuring wetting and swelling of bentonite using X-ray imaging

Tero Harjupatana *, Arttu Miettinen, Markku Kataja

Department of Physics, University of Jyväskylä, P.O. Box 35 (YFL), FI-40014, Finland

ARTICLE INFO

Keywords:
X-ray imaging
Water content
Water transport
Deformation
Bentonite
Swelling

ABSTRACT

A non-invasive method based on X-ray imaging for measuring deformation and water transport in wetting and swelling bentonite samples is introduced. Sequential X-ray images taken of the samples were used to calculate the attenuation coefficient and deformation. These results, together with careful calibration, allowed finding the dry density and water content distributions and their temporal evolution in the wetting and swelling samples. A specific correction technique, based on regularly taking reference X-ray images of aluminum plates of varying thickness, was developed and used to take into account X-ray beam instabilities and thus to improve the accuracy of density analysis. Large deformation, present in the experiments, was measured with an improved version of a block-matching algorithm. The X-ray imaging method was used here to measure the axial swelling of compacted MX-80 bentonite samples in a tube when in contact with saline solution (0.1 M NaCl). This setup mimics a scenario where bentonite, planned to be used as a buffer material in a nuclear waste repository placed deep in the bedrock, swells into a rock fracture filled by groundwater. The method yielded potentially valuable data on hydro-mechanical behavior of bentonite, which may be used in developing and validating material models to be used in safety assessment of nuclear waste repository concepts.

1. Introduction

Transport of liquids in porous materials is of great interest in many areas, e.g., in biology, soil sciences and construction technology. Non-destructive methods based, e.g., on electromagnetic and neutron radiation, and on nuclear magnetic resonance imaging have been used to monitor liquid transport in related applications (Zhou et al., 2014; Jung et al., 2012; Shafizadeh et al., 2015; Terskikh et al., 2005). Most methods are, however, restricted to cases where the deformation of the solid matrix can be neglected. Yet, many materials swell or shrink notably with variations of liquid content. Simultaneous monitoring of both solid and liquid content would therefore be useful, e.g., in developing and validating hydro-mechanical material models. To this end, the authors previously introduced a method based on X-ray tomography for measuring deformation and water transport in bentonite samples wetted in a constant volume (Harjupatana et al., 2015). The technique was later successfully applied to measure wetting and swelling of a wood-fibre reinforced composite material (polylactic acid and birch pulp) (Miettinen et al., 2016). In both studies, a simple block-matching algorithm was adequate to measure small deformation. The water transport and deformation were also relatively slow (experiment duration 1–20 weeks) compared to the scan duration (1–4 h), and thus the time resolution was sufficient. X-ray tube based microtomography devices, as used here, produce high-resolution 3D images but have quite long scan times (typically from several minutes to tens of hours) depending on sample type, sample size and desired image quality. Those devices are thus suitable to monitor relatively slow processes only.

Bentonite is a clay material with high montmorillonite content, and it swells strongly in the presence of water. Due to its swelling ability and low permeability for water, a bentonite layer is often used as a groundwater seal on various waste sites and ponds (Koch, 2002). Bentonite is also suggested to be used as a buffer material between the waste canisters and the bedrock in nuclear waste disposal concepts in many countries, e.g., in Finland (Juvankoski, 2013), Sweden (Börjesson et al., 2010) and Switzerland (Nagra, 2009). There, a particular risk is the possible erosion of bentonite through groundwater filled macroscopic fractures in the bedrock, which may expose the waste canisters to groundwater (Neretnieks et al., 2009; Reid et al., 2015).

The main goal of this work was to develop a method applicable for producing experimental data to support modeling the behavior of the

* Corresponding author.
E-mail address: tero.t.harjupatana@jyu.fi (T. Harjupatana).

https://doi.org/10.1016/j.clay.2022.106485
Received 8 September 2021; Received in revised form 3 March 2022; Accepted 4 March 2022
Available online 15 March 2022

Table 1
Result of sieve analysis for MX-80 bentonite. The mean and standard deviation (SD) were calculated from three repetitions.

Sieve size [mm]	Mass passed [%] (mean ± SD)
2.000	99.9 ± 0.1
1.000	98.9 ± 0.2
0.500	66.5 ± 1.5
0.250	34.4 ± 1.6
0.125	16.0 ± 1.0
0.100	11.9 ± 0.8
0.050	3.2 ± 0.2

Table 2
Mineralogical properties for MX-80 bentonite (Karnland et al., 2006; Karnland, 2010).

Mineral composition (Wt%)	Montmorillonite (81.4%), Tridymite (3.8%), Plagioclase (3.5%), Muscovite (3.4%), Quartz (3.0%), Cristobalite (0.9%), Gypsum (0.9%), Illite (0.8%), Pyrite (0.6%), Lepidocrocite (0.5%), Hematite (0.4%), Anatase (0.2%), Calcite (0.2%), Magnetite (0.2%), Goethite (0.1%), Microcline (0.1%)
Cation exchange capacity	0.75 eq/kg
Exchangeable cations	Na^+ (0.55 eq/kg), Ca^{2+} (0.13 eq/kg), Mg^{2+} (0.05 eq/kg), K^+ (0.01 eq/kg)
Structural formula for montmorillonite	$Na_{0.46}\ Ca_{0.05}\ Mg_{0.02}\ K_{0.01}\ (Si_{7.94}\ Al_{0.06})$. $(Al_{3.10}\ Ti_{0.01}\ Fe_{0.37}{}^{3+}\ Mg_{0.50})\ O_{20}\ (OH)_4$
Grain density	2.75–2.78 g/cm^3

bentonite buffer in a scenario where erosion might take place. To reproduce the wetting and swelling of the bentonite buffer emplaced in a repository tunnel, the actual fracture in a rock was simulated by a simplified tube geometry. Part of the vertical sample holder tube was filled with compacted bentonite and exposed to saline solution, leading to approximately one-dimensional axial transport of water and swelling of bentonite. Instead of X-ray tomography, the resulting fast swelling was monitored using X-ray imaging, which allows to study much faster processes, but is limited to simpler sample geometries. A substantial improvement, a correction technique that takes into account angular and temporal instabilities of the X-ray beam was developed and used to increase the accuracy of density analysis. Furthermore, the block-matching algorithm used to find the displacement field of the solid material was improved to account for large deformations. The X-ray imaging method was applied here to 16 bentonite swelling experiments, where the initial dry density and the initial water content of the samples were varied.

2. Materials

The sample material was Wyoming type bentonite under the brand name MX-80. The grain size distribution of this granular material was measured using a sieve analysis (Table 1). The largest particles were around 1 mm in diameter while the mass average diameter of grains was around 0.4 mm. Mineralogical properties of MX-80 bentonite are given in Table 2. MX-80 has a high montmorillonite content (81%), while silica minerals quartz and its polymorphs tridymite and cristobalite make up 8% of the total mass, and the rest consist of different accessory minerals. The cation exchange capacity values and the structural formula for montmorillonite show that sodium is the dominant cation. Wyoming bentonites, such as MX-80, are known as high-grade sodium bentonites having high swelling capacity.

Bentonite powder and samples were wetted with saline solution (0.1 M NaCl), which approximated the sodium concentration (0.115 M Na^+, dominant cation) in the current groundwater at the depth (465 m) of nuclear waste repository at Olkiluoto, Finland (Hellä et al., 2014), but neglected other cations and components (in particular 0.033 M Ca^{2+}).

3. Experimental setup and procedure

3.1. Sample holder and samples

The sample holder consisted of a vertical aluminum tube of inner diameter 10 mm, wall thickness 1 mm, and height 95 mm, attached to a mounting plate (Fig. 1). A proper amount of preconditioned (see below) MX-80 bentonite powder was placed in the sample holder tube and compacted to form a sample of height 20 mm. The bottom end of the sample was firmly against a porous sintered glass filter disc (pore diameter 10–16 μm), which allowed pore air to be released from the sample. Compacting the samples directly into the tube eliminated gaps between the sample and the tube, which could have acted as water

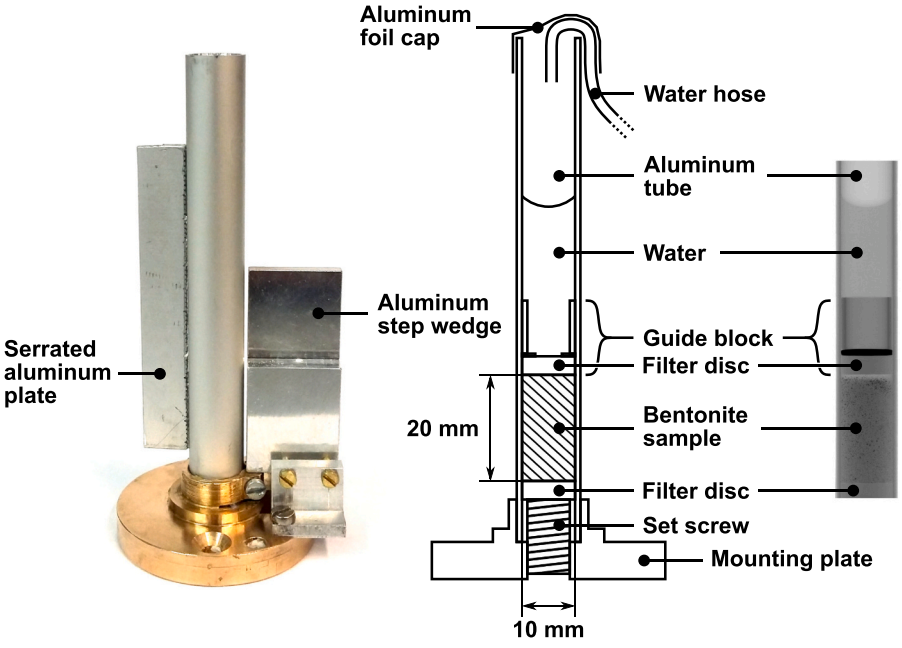

Fig. 1. Photo (left), schematic cross-sectional view (middle) and X-ray image (right) of sample holder.

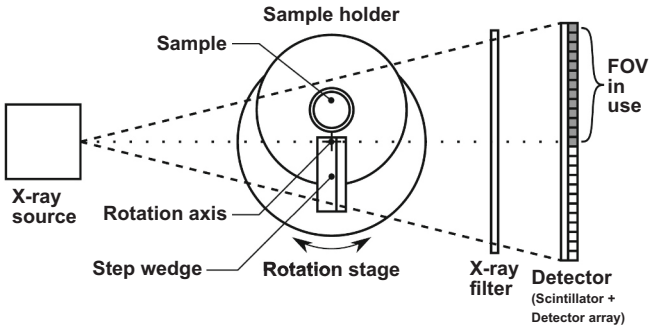

Fig. 2. Schematic top view of X-ray imaging setup (not to scale). The generated X-rays traversed through a sample and were detected with a scintillator plate and a detector array. An X-ray filter (exceptionally located on the detector side here) was used to cut the lower part of the energy spectrum. The sample holder was attached non-concentrically on the rotation stage, and a half of the FOV was in use (shaded pixel columns). This allowed to take the necessary reference images by rotating the stage by 180°.

transport channels. A freely-moving guide block ($m = 1.5$ g), consisting of a porous filter disc (similar to the bottom one), a steel washer and a short piece of aluminum tube, was placed on the top of the sample. The guide block ensured that the top surface of the sample remained flat and well defined during the swelling process. An aluminum step wedge with 3 mm and 8 mm thick steps, and a serrated aluminum plate were installed alongside the tube to facilitate beam hardening correction and image stitching procedures, respectively (see sections 4.1 and 4.2).

Eight different combinations of initial dry density values 1.40 g/cm^3, 1.65 g/cm^3 and 1.80 g/cm^3 and water content values 12%, 17% and 24% were examined with two repetitions for each possible case (1.80 g/cm^3 and 24% is unfeasible, see Eq. 19). Here, the water content is defined as $w = m_w/m_b = \rho_w/\rho_b$, where m_w and m_b are the masses of water and bentonite in volume V, and $\rho_w = m_w/V$ and $\rho_b = m_b/V$ are the partial densities of water and bentonite. The partial density of bentonite is also called 'dry density'. The initial water content of the powder was about 12% in storage conditions, measured by oven drying at 105 °C. The two higher initial water content values were achieved by spraying the bentonite powder with saline solution (0.1 M NaCl) and mixing thoroughly. A small amount of iron particles of diameter around 100 μm (1.5% by weight) were mixed with the powder to act as tracer particles in the X-ray images so that deformation could be measured. This particle density and size was tested to be suitable in this work.

3.2. X-ray imaging

In X-ray imaging, the sample is illuminated with X-rays, and the partially attenuated intensity is measured by a detector array (Fig. 2). Typically, the detector has a scintillator plate, which converts X-rays into visible light. This light is then converted into a digital X-ray image by using an image sensor array coupled to suitable optics. Ideally, the grayscale values of an X-ray image are proportional to the intensity of the X-ray beam incident to the scintillator. The attenuation of a narrow monochromatic X-ray beam is described by the Beer-Lambert law

$$\frac{I}{I_0} = exp\left[- \int_C \mu\left(x\right) dx \right], \tag{1}$$

where I is the attenuated intensity, I_0 is the unattenuated intensity, I/I_0 is the transmittance, μ is the linear attenuation coefficient and x is the position along the line (C) from the source to the detector. From here on, the quantities I and I_0 are directly used to denote X-ray images; I is the dark-field corrected X-ray image and I_0 is the dark-field corrected background image (i.e., the X-ray image taken without a sample). The dark-field correction is a simple subtraction $I = I' - I_D$, where I' is the uncorrected X-ray image and I_D is the dark image (i.e., the image taken without X-rays).

Table 3
Five-stage X-ray image acquisition process.

Stage	Number of images	Time interval between images	Total time	Description
0	1	–	–	Initial state, unwetted sample
1	29	20 s	10 min	Fast initial swelling
2	30	4 min	2 h	Transitional swelling
3	279	20 min	95 h	Slow late stage swelling
4	1	–	–	Final state, frozen sample

For compounds and mixtures, the linear attenuation coefficient is given by the mixture rule

$$\mu = \sum_i c_i \cdot \rho_i, \tag{2}$$

where $c_i = (\mu/\rho)_i$ and ρ_i are the mass attenuation coefficient and the partial density of each constituent, respectively (Hubbell and Seltzer, 1995). The mass attenuation coefficient depends on the elemental composition of the material and on the X-ray energy, but is expected to be independent of density.

The X-ray imaging was performed using a SkyScan 1172 microtomography scanner in X-ray imaging mode with 1000 (H) × 524 (V) pixels and 32 μm pixel size. This pixel size was sufficient to capture the 100 μm iron particles, and resulted in the field of view (FOV) 32 (H) mm × 17 (V) mm. As there was no option to move the rotation stage sideways (normal to source-detector line), the sample holder was attached non-concentrically on the rotation stage of the scanner (Fig. 2). This conveniently allowed to take reference X-ray images of the background (I_0) and of the two aluminum plates in the step wedge (I_{r1} and I_{r2}) by rotating the stage by 180°. The rotation angle was set to 0° when the sample was imaged and to 180° when the reference images were taken. This procedure halved the usable FOV of a single image to 16 (H) mm × 17 (V) mm. The FOV was, however, extended in the vertical direction to 16 (H) mm × 65 (V) mm by stitching five images taken from different vertical positions with 12 mm spacing. Here, the rotation stage was moved in the vertical direction while the X-ray source and the detector were in fixed positions. The X-ray tube was operated with an acceleration voltage of 100 kV and a current of 80 μA. The low energy part of the X-ray spectrum was attenuated using a built-in filter plate with 0.5 mm aluminum and 0.04 mm copper layers. The exposure time for a single X-ray image was 1106 ms, but the average of 10 images was used to improve the signal-to-noise ratio. The total image acquisition time, including the time needed for the reference images and sample movements, was approximately 4 min for the extended FOV. Each X-ray image taken was automatically dark-field corrected by the scanner. The pixel values of the dark images were very small ($\langle I_D/I_0 \rangle \approx 0.2\%$) and stable during the experiments. A new dark image was taken before each experiment.

3.3. Measurement procedure

After sample preparation, the sample holder was attached to the rotation stage of the scanner, and a water hose, pulled into the scanner through a cable lead-in, was put into the sample holder tube (Fig. 1). The open top end of the tube was sealed with aluminum foil to prevent the evaporation of water. The X-ray source was turned on and let to stabilize about 1 h. Thereafter, a five-stage X-ray image acquisition process was started (Table 3). The first X-ray image was taken of the unwetted sample (stage 0). The wetting was then initiated by injecting water into the upper part of the sample holder tube. The wetting and swelling

process was monitored for about four days using three different imaging procedures (stages 1–3), where the time interval between the images was increased at each stage as the swelling slowed down. In stage 1, the fast initial swelling was captured by using the single image FOV at only one vertical position covering the upper end of the sample. Also omitting the reference images reduced the time interval between X-ray images to 20 s in this stage. The X-ray images from the other positions, assumed not to be affected by the wetting, were copied from stage 0 and used to construct the extended FOV image of the entire sample. The reference images for stage 1 were interpolated from those taken in stages 0 and 2. At the end of the experiment, the sample holder was detached and dipped into liquid nitrogen, thereby freezing the sample thoroughly. The sample holder was reattached into the scanner and an X-ray image of the frozen sample was taken (stage 4). The sample holder was again detached and the tube and the sample were cut into 4–6 slices of thickness 6.8 mm (the number of slices depended on the final height of the sample). The freezing ensured that the sample, especially the soft upper part, was solid and thus it could be properly handled and sliced. The masses of bentonite and water in the slices were determined gravimetrically by oven drying at 105 °C at least 14 h. As the dimensions of the slices were also measured, the average partial densities of bentonite and water in the slices could be calculated. These data were used to validate the method and estimate the overall error of the results (see section 5).

4. Image processing and data analysis

4.1. Local beam hardening correction

Beam hardening is an artifact related to the use of a polychromatic X-ray source such as an X-ray tube. When X-rays traverse through a material, the average energy of the beam increases as the lower energy X-ray photons are attenuated more efficiently than the higher energy ones. In this case, the effective linear attenuation coefficient depends on material thickness and the Beer-Lambert law (Eq. 1) is not accurate. Correcting for beam hardening is usually not necessary in conventional X-ray imaging, e.g., when density differences are inspected qualitatively. However, in X-ray tomography the beam hardening correction (BHC) is a standard procedure. A widely used phenomenologically justified method is to use a quadratic correction of the form (Herman, 1979; Hsieh et al., 2000; Zou et al., 2011)

$$ln\left(\frac{I}{I_0}\right)_c = A_1 \cdot ln\left(\frac{I}{I_0}\right)_m + A_2 \cdot ln^2\left(\frac{I}{I_0}\right)_m, \quad (3)$$

where the subscripts c and m denote the corrected and measured transmittances, respectively. Typically, the value of the coefficient A_1 is set to 1, and the operator visually finds a value for the coefficient A_2 such that the effect of the beam hardening (the cupping artifact) appears minimized in the reconstructed images.

The energy spectrum of the conical X-ray beam produced by an X-ray tube may include small spatial and temporal variations caused, e.g., by the anode heel effect (Bushberg et al., 2002) and by instabilities in the X-ray focal spot (Zhou et al., 2016). Some variations may also be caused by the detector. In the standard BHC these small variations are neglected and the same value of coefficient A_2 is used to correct all the pixels in a set of X-ray images that may be acquired over a prolonged time. The present method is sensitive to these variations as it utilizes X-ray images to measure small density differences in swelling and wetting bentonite samples. Thus, a specific correction procedure, called here a local beam hardening correction (LBHC), was developed to simultaneously correct the effect of beam hardening and its variations. A similar method was recently introduced also by Gustschin et al. (2019) to improve image quality in X-ray tomography. The LBHC is based on selecting a suitable homogeneous reference material for which the Beer-Lambert law (Eq. 1) can be written in a form

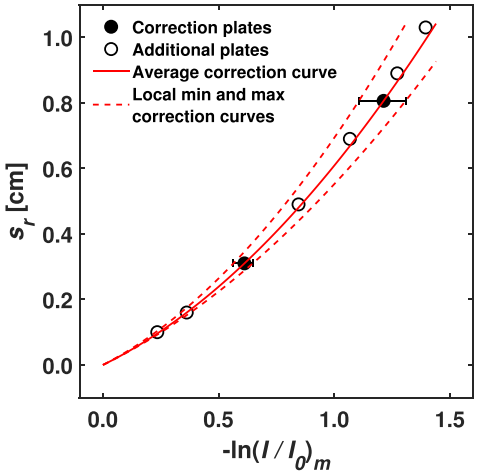

Fig. 3. Local beam hardening correction. The solid line is the correction curve (Eq. 5) for the averaged data from the aluminum correction plates in the step wedge (solid circles). The horizontal error bars and the dashed lines illustrate the local variation across the FOV. The open circles show the averaged data from additional aluminum plates used only here to validate the correction method.

$$ln\left(\frac{I}{I_0}\right)_c = -\mu_r s_r, \quad (4)$$

where μ_r is the linear attenuation coefficient and s_r is the thickness of the reference material. Combining Eq. 3 and 4 yields

$$s_r = A_1' \cdot ln\left(\frac{I}{I_0}\right)_m + A_2' \cdot ln^2\left(\frac{I}{I_0}\right)_m, \quad (5)$$

where $A_i' = -A_i/\mu_r$. This form (Eq. 5) transforms the measured transmittance into the equivalent thickness of the reference material.

The effect of beam hardening is best corrected when the mass attenuation coefficients of the sample and reference materials have similar energy dependence. This is the case for materials having comparable values of effective atomic number Z_{eff}, which can be calculated for compounds using the approximate formula (Johns and Cunningham, 1983)

$$Z_{eff}^{3.5} = \sum_i f_i \cdot Z_i^{3.5}, \quad (6)$$

where f_i and Z_i are the fraction of electrons and the atomic number of atom i in the compound, respectively. By using an empirically determined composition of MX-80 bentonite (Table 2) and the chemical formula for water, Eq. 6 gives $Z_{eff,b}$=12.8 and $Z_{eff,w}$=7.5. Here, an appropriate reference material was thus found to be aluminum (Z_{Al}=13). With this choice the method can be expected to be sufficiently accurate for bentonite, but may lead to slight overcorrection for pure water.

The coefficients A_i' were solved locally by forming two simultaneous equations from Eq. 5 using the measured transmittances (I_{r1}/I_0 and I_{r2}/I_0) and the thicknesses of the two aluminum correction plates (s_{r1} = 3 mm and s_{r2} = 8 mm) present in the step wedge (see Figs. 1 and 2). The coefficients were first solved for subregions of size 10 × 10 pixels, and then interpolated to individual pixels. This accuracy was found sufficient to resolve the inhomogeneities of the X-ray source and, on the other hand, to provide sufficient averaging to reduce noise. Exemplar data and correction curves are shown in Fig. 3. The correction is in good agreement with the data from additional aluminum plates measured separately, and not used in solving the coefficients A_i'. The error bars and the minimum and maximum local correction curves show the spatial

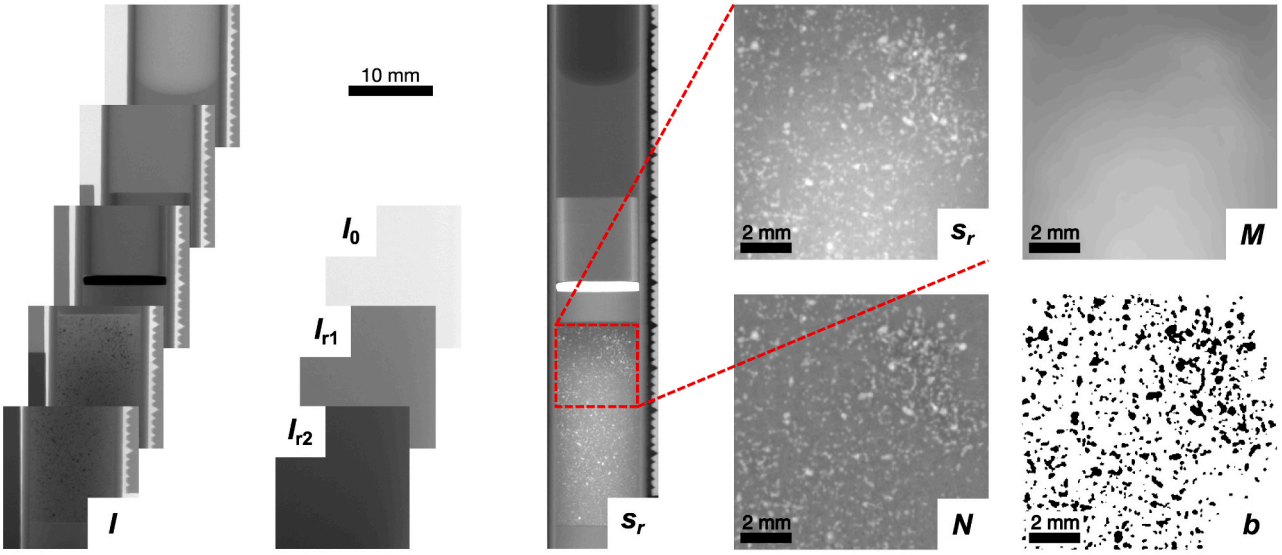

Fig. 4. Image processing procedure. The partly overlapping X-ray images (I), taken at various vertical positions of the sample holder tube, were first converted to aluminum equivalent thickness images using the reference images (I_0, I_{r1} and I_{r2}) and then stitched to form a combined aluminum equivalent thickness image of the sample and the tube (s_r). A normalized image (N) was formed by subtracting the median filtered image (M) from the stitched image (s_r). The normalized image was further thresholded to form a binary mask image (b). The visibility of the serrated plate in the stitched image (s_r) has been enhanced in this figure.

variation of the correction across the FOV.

4.2. Stitching, normalization and thresholding

The image processing procedure is illustrated in Fig. 4. After applying the LBHC to the X-ray images taken (I), the FOV was extended by stitching the aluminum equivalent thickness images (s_r). This was done by appropriately cropping the images, and joining the cropped images vertically together to achieve a continuous image of the entire sample tube. The serrated aluminum plate was used to visually verify the accuracy of the stitching process. The stitched images were 2D median filtered with a radius large enough so that the tracer particles disappear leaving approximate background visible ($M = \text{Median}\{s_r\}$). Normalized images were then formed by subtracting this background from the stitched images ($N = s_r - M$). The deformation of the samples was measured using the normalized images (see section 4.3). The normalized images were further thresholded to form binary mask images $b = H(N_{th} - N)$, where H is the Heaviside step function and N_{th} is the threshold value that sets the pixels containing tracer particles to 0 and the other pixels to 1. The binary mask images were used to exclude the tracer particles from the stitched images (s_r), which were used to calculate the attenuation coefficient (see section 4.4).

4.3. Deformation

The displacement u_z at position z in the sample was calculated using a two-dimensional block-matching algorithm, applied to the normalized images (N). As the swelling of bentonite in the present tube geometry was approximately one-dimensional, the displacements were measured only in the axial direction (z). A rectangular reference block $B_{\text{ref}}(z)$, a subimage of m (H) × n (V) pixels centered at z, was first extracted from the initial state image. Blocks of similar size $B(z + u_z)$ were then extracted from the deformed state image at different pixel positions (u_z=0, ± 1 px, ± 2 px, …). The minimum of the mean squared difference

$$\text{MSD}(u_z, z) = \frac{1}{mn}\sum_{i=1}^{n}\sum_{j=1}^{m}\left[B_{ij}(z+u_z) - B_{\text{ref},ij}(z)\right]^2 \quad (7)$$

yielded the displacement u_z at location z. Subpixel accuracy was achieved by fitting a quadratic polynomial to the MSD values near its minimum, and using the location of the minimum of the polynomial as the final value of displacement.

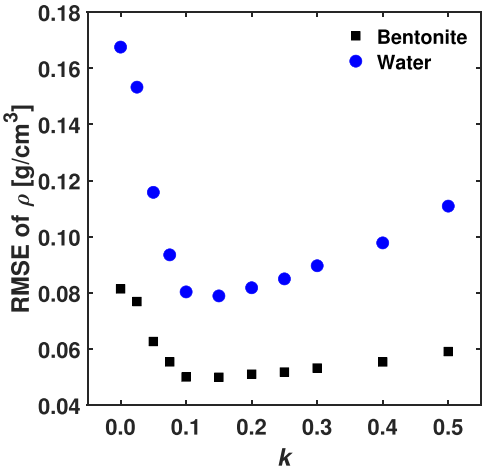

Fig. 5. Root-mean-square error (RMSE) of partial densities of bentonite and water between results and validation data as a function of block update parameter k (Eq. 9). Each point of the graph represents the RMSE value of 160 data points (16 samples × 10 layers).

In general, such a block-matching algorithm leads to satisfactory results in cases where no significant local deformation of the material between the compared blocks takes place, i.e., the displacement corresponds to pure translation. However, here the bentonite swelled locally many times of its original volume and resulted in low correlation between the blocks extracted from the initial state image and from the images taken some time later. This, in turn, led to reduced accuracy in finding the value of displacement corresponding to the minimum of MSD(u_z, z). Updating the entire reference image to the current image after each time step did not help to avoid such a problem, but resulted in significant cumulative error of displacement at later times. To minimize the total error, an optimized method was used such that the reference block was locally updated only whenever the correlation between the block from the current deformed state image and the reference block

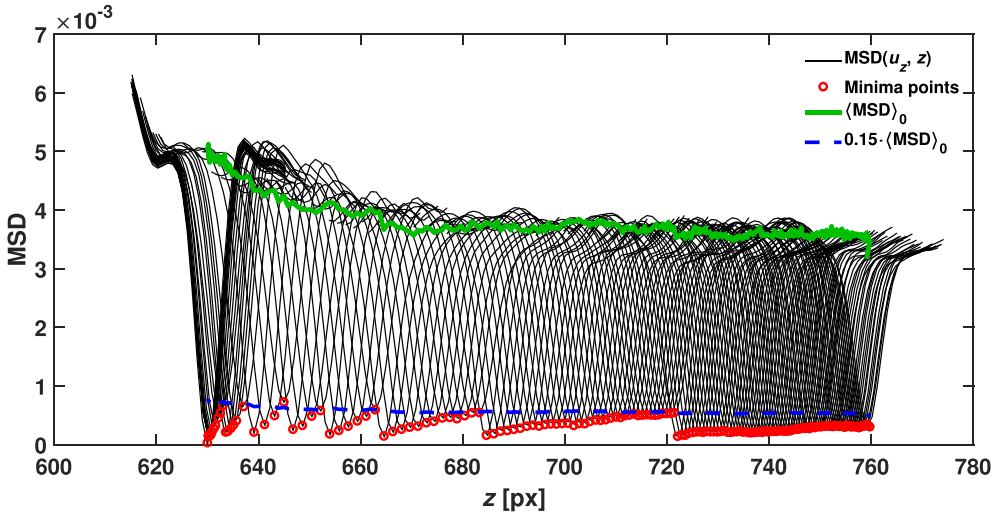

Fig. 6. Calculation of displacement at a grid point. The minima points of the MSD curves gave the new positions of the material initially at the grid point ($z = 630$ px). The minimum value of the MSD increased with decreasing correlation as the bentonite deformed. The reference block was repeatedly updated according to the criterion given by Eq. 9 leading to sudden decrease of the minimum value at corresponding locations. Here, only every second MSD curve is shown for clarity.

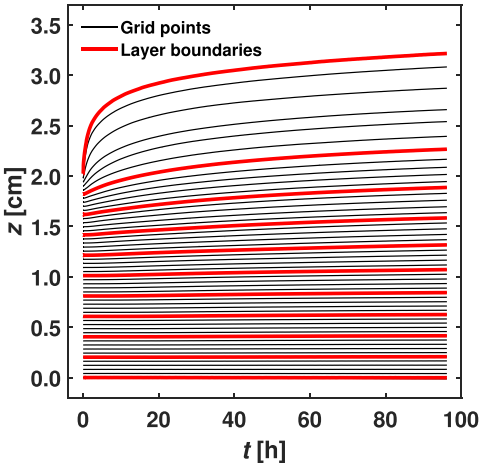

Fig. 7. Measured deformation for sample 5B ($\rho_{b0} \approx 1.65\,\mathrm{g/cm^3}$, $w_0 \approx 17\%$, see section 5). The positions of the grid points and the layer boundaries are plotted as a function of time. The top and bottom boundaries were measured by tracking the positions of the filter discs. The other boundaries were averaged from the positions of the grid points, which were measured with the block-matching algorithm.

became lower than some predetermined threshold value. Here, the minimum value of the MSD was used as a measure of the degree of correlation between the blocks. For perfect correlation the value is zero and for fully uncorrelated blocks ($\langle B \cdot B_{\mathrm{ref}} \rangle = \langle B \rangle \cdot \langle B_{\mathrm{ref}} \rangle$) the expected value is given by

$$\langle \mathrm{MSD} \rangle_0 = \left\langle \left(B - B_{\mathrm{ref}} \right)^2 \right\rangle_0 = \langle B^2 \rangle - 2\langle B \rangle \cdot \langle B_{\mathrm{ref}} \rangle + \left\langle B_{\mathrm{ref}}^2 \right\rangle \tag{8}$$

The reference block was updated whenever the criterion

$$min(\mathrm{MSD}). > k \cdot \langle \mathrm{MSD} \rangle_0 \tag{9}$$

was met. An optimal value for the parameter k was found by calculating the root-mean-square error of the partial densities of bentonite and water between the final result given by the method and the gravimetric validation data as a function of k (Fig. 5). The two curves, based on both bentonite and water data, have the minima at around k=0.15, which was thereby chosen to be the low correlation threshold in the deformation measurement. Fig. 6 shows a set of MSD curves of an arbitrary grid point and illustrates how the calculation of the displacement took place at this particular point.

The block-matching algorithm was applied to the normalized images by forming 50 equally spaced grid points along the axial direction of the sample in the initial state. Reference blocks of size 315 (H) × 41 (V) pixels, covering the whole width of the sample, were formed around each grid point and the matching blocks were searched from the subsequent images as described above. To improve the signal-to-noise ratio in further analysis, the samples were divided into 10 equally spaced layers in the initial state. The position of the layer boundaries was determined by performing local quadratic fitting to the deformation data. The deformation measurement at the top end of the sample turned out to be difficult as the tracer particles became sparse in that region. Therefore, the displacement of the top end was measured more accurately by tracking the movement of the filter disc. This was done by fitting a sigmoid-type function to the axially averaged profiles of the linear attenuation coefficient in the vicinity of the upper end of the sample. Similar fit was also used for the bottom end, although the displacement there was minimal. Fig. 7 shows an example of the measured deformation, where the positions of the grid points and the layer boundaries are plotted as a function of time. Similar deformation plots for all the samples can be found in section C in the supplementary material.

The deformation analysis is based on the assumption that the tracer particles strictly follow the motion of bentonite in all parts of the sample, including especially the upper part where the water content became high. The validity of this assumption was confirmed by a separate sedimentation test discussed in section B in the supplementary material.

4.4. Relative attenuation coefficient

By assuming the linear attenuation coefficient of the tube wall (μ_t) and the sample (μ_s) to be constants along the beam direction (see Eq. 1), the aluminum equivalent thickness is given by

$$s_r = \mu_t' \cdot s_t + \mu_s' \cdot s_s, \tag{10}$$

where $\mu_t' = \mu_t/\mu_r$ and $\mu_s' = \mu_s/\mu_r$ are the relative attenuation coefficients (μ_r is the linear attenuation coefficient of the reference material), and s_t and s_s are the beam travel distances inside the tube wall and the sample, respectively. The travel distances were calculated by assuming the parallel beam geometry (Fig. A.1, supplementary material). This

assumption is justified as the source-to-sample distance (243 mm) was much larger than the tube diameter (12 mm). The relative attenuation coefficient of the tube was calculated individually for each sample from the empty tube area in the initial state image by setting $\mu_s' = 0$ in Eq. 10 and then averaging the obtained 2D relative attenuation coefficient image into a single value using the weighted average

$$\overline{\mu}_t' = \frac{\sum_i \sum_j \left(s_{t,ij} \cdot \mu_{t,ij}' \right)}{\sum_i \sum_j s_{t,ij}}, \tag{11}$$

where i and j are the indices of image pixel rows and columns, respectively. The mean and standard deviation of the relative attenuation coefficient for the 16 aluminum sample holder tubes were found to be 0.980 ± 0.014. The relative attenuation coefficient of the sample was calculated for each pixel using Eq. 10 with $\mu_t' = \overline{\mu}_t'$. The resulting 2D relative attenuation coefficient image was further averaged row by row to produce an axial distribution of the relative attenuation coefficient of the sample material as the weighted average

$$\mu_{s,i}' = \frac{\sum_j \left(b_{ij} \cdot s_{s,ij} \cdot \mu_{s,ij}' \right)}{\sum_j \left(b_{ij} \cdot s_{s,ij} \right)}, \tag{12}$$

where b_{ij} is the pixel value of the binary mask image at row i and column j (see section 4.2). The binary mask image is used here to exclude the tracer particles from the calculation.

4.5. Density calibration

By using the mixture rule (Eq. 2), the relative attenuation coefficient of the sample, consisting of bentonite and water, can be written as

$$\mu_s' = c_b' \cdot \rho_b + c_w' \cdot \rho_w, \tag{13}$$

where $c_b' = c_b/\mu_r$ and $c_w' = c_w/\mu_r$. The attenuation of air, present in the sample, was neglected due to its low density and low attenuation. The coefficients c_b' and c_w' were calculated by performing a two-point calibration individually for each sample. By using the initial state of the sample and the water layer in the subsequent images, the coefficients were solved from the equations

$$c_b' \cdot \overline{\rho}_{b0} + c_w' \cdot \overline{w}_0 \cdot \overline{\rho}_{b0} = \overline{\mu}_{s0}', \tag{14}$$

$$c_b' \cdot 0 + c_w' \cdot \overline{\rho}_{wl} = \overline{\mu}_{wl}', \tag{15}$$

where $\overline{\rho}_{b0}$, $\overline{w}_0$ and $\overline{\mu}_{s0}$ are the average dry density, water content and relative attenuation coefficient of the sample in the initial state, and $\overline{\rho}_{wl} = 1.00$ g/cm^3 and $\overline{\mu}_{wl}'$ are the average density and relative attenuation coefficient of the water layer, respectively. The mean and standard deviation of the coefficients c_b' and c_w' for the 16 samples were found to be (0.3814 ± 0.0065) cm^3/g and (0.1709 ± 0.0059) cm^3/g, respectively.

4.6. Partial density of bentonite and water

During the swelling process, the mass of bentonite is conserved within each vertical layer of the sample as the layer boundaries follow the motion of bentonite. Applying Eq. 13 on a given layer in the initial state yields the mass of bentonite in the layer as

$$m_b = \frac{\mu_{s0}' \cdot V_0}{c_b' + w_0 \cdot c_w'}, \tag{16}$$

where μ_{s0}' and V_0 are the relative attenuation coefficient and volume of the layer in the initial state, respectively. The partial density of bentonite in the same layer in a deformed state is thus given by

Table 4
Measured dry density (ρ_{b0}), water content (w_0), degree of saturation (S_0) and density gradient ($d\rho_{b0}/dz$) of samples in the initial state, and top end displacement (u_t) and occurrence of clearly visible voids in the final state. The dry density was calculated using accurate sample dimensions from X-ray images. The degree of saturation was calculated as $S_0 = w_0 \cdot \rho_{b0}/\rho_{w,\,sat}$, where $\rho_{w,\,sat}$ is the partial density of water at saturation (Eq. 19). The density gradient was determined by performing a linear fit to the initial density profile.

Sample name	Original name	ρ_{b0} [g/cm^3]	w_0 [%]	S_0 [%]	$d\rho_{b0}/dz$ [g/cm^4]	u_t [cm]	Visible voids
1A	FS20	1.40	12.0	34.1	0.110	2.21	Yes
1B	FS27	1.42	11.9	34.9	0.095	1.39	Yes
2A	FS23	1.37	17.1	46.8	0.079	1.12	Yes
2B	FS28	1.42	17.8	52.2	0.108	1.81	Yes
3A	FS25	1.45	23.9	72.8	0.107	0.66	No
3B	FS30	1.42	24.4	71.2	0.102	0.72	No
4A	FS17	1.66	12.1	50.3	0.146	1.43	Yes
4B	FS22	1.62	12.0	47.5	0.109	1.00	No
5A	FS16	1.62	17.4	68.3	0.124	1.26	Yes
5B	FS18	1.62	16.6	65.4	0.123	1.18	No
6A	FS14	1.62	24.1	94.9	−0.013	0.92	Yes
6B	FS19	1.63	24.0	96.4	0.014	0.72	Yes
7A	FS26	1.86	12.0	68.5	0.119	0.93	No
7B	FS31	1.87	11.9	69.4	0.130	1.36	Yes
8A	FS24	1.84	17.1	94.4	0.063	0.68	No
8B	FS29	1.76	17.8	86.5	0.036	1.20	Yes

$$\rho_b = \frac{m_b}{V} = \frac{\mu_{s0}' \cdot V_0/V}{c_b' + w_0 \cdot c_w'}, \tag{17}$$

where the volume ratio of the layer V_0/V is readily obtained based on the measured deformation. Finally, the partial density of water in the layer is given by Eq. 13 as

$$\rho_w = \frac{\mu_s' - c_b' \cdot \rho_b}{c_w'}. \tag{18}$$

5. Results

The complete set of results of the 16 individual experiments carried out are available at DOI: https://doi.org/10.5281/zenodo.5413932 (Harjupatana et al., 2021).

5.1. Initial values and density gradients

Table 4 shows the measured dry density, water content, degree of saturation and density gradient in the initial state for all the samples. Also is given the measured displacement of the top end and the occurrence of clear voids in the final state (discussed later). The measured initial dry densities of the samples deviated slightly from the target values (1.40 g/cm^3, 1.65 g/cm^3 and 1.80 g/cm^3), because the target height of the samples (2 cm) was difficult to achieve accurately. The samples slightly expanded right after the compaction, which was difficult to predict and compensate either by slightly overcompacting or by increasing the target mass of the sample. Most of the samples had an average initial density gradient of around 0.1 g/cm^4, and thus the top end was around 0.2 g/cm^3 denser than the bottom end. The initial density gradients were caused by wall friction during the sample compaction (Michrafy et al., 2003). In uniaxial powder compaction, with a die and a single-acting punch on the top, the wall shear stress between the powder and the die opposes the motion of the powder. As a result, the magnitude of total friction force increases downward due to increasing wall area. This causes the compressive stress and hence the density to decrease downward. This common issue in powder compaction cannot be completely eliminated, but may be reduced by using a lower aspect ratio (h/d) of the sample and lubrication (Tien et al., 2007). However, samples 6A, 6B, 8A and 8B showed much smaller density

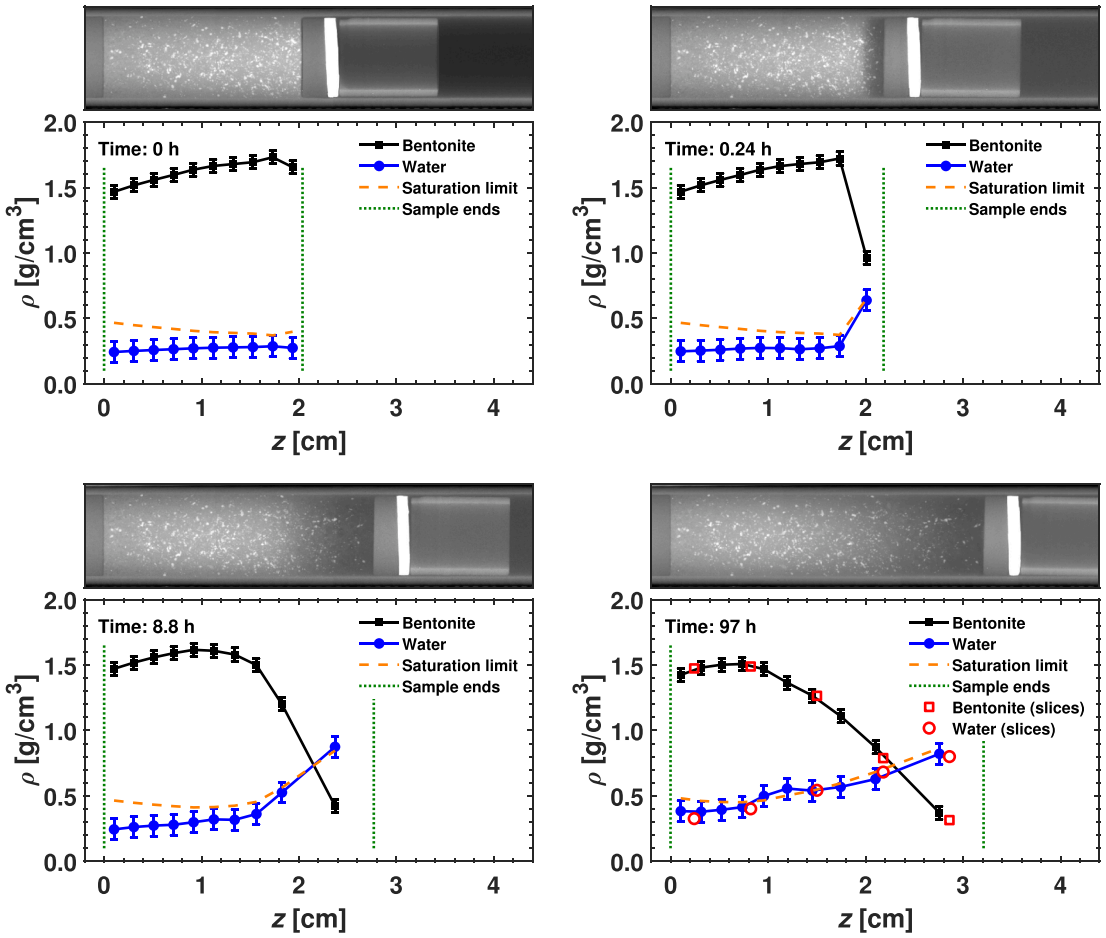

Fig. 8. Example of main results for sample 5B ($\rho_{b0} \approx 1.65\,g/cm^3$, $w_0 \approx 17\%$). The measured partial density profiles of bentonite and water, the saturation limit, and the corresponding aluminum equivalent thickness images are shown at four instants of time. Also shown are the validation data in the last subfigure.

gradients. Those samples were compacted near the saturation limit (S_0=100%), at which the sample material becomes nearly incompressible. This forces the density profile to be flat provided that no redistribution of water occurs.

5.2. Partial densities of bentonite and water

Here, only a few examples of the main results are shown to assess the feasibility of the method and to demonstrate the main qualitative features of the results. Figs. 8 and 9 show examples of the main results, i.e., the axial distributions of partial density of bentonite and water at four instants of time for samples 5B and 6A. These samples had the same initial dry density $\rho_{b0} \approx$ 1.65 g/cm^3, but different initial water content values $w_0 \approx$ 17% and $w_0 \approx$ 24%, respectively. The corresponding aluminum equivalent thickness images are shown on top of the graphs (rotated to horizontal position). The last subfigures show the final state of the samples together with the gravimetric validation data. The error bars represent the root-mean-square error of the data points (± 0.05 g/cm^3 for bentonite and ± 0.08 g/cm^3 for water, see Fig. 5). Also shown in the figures is the saturation limit estimated using the formula

$$\rho_{w,\mathrm{sat}} = \rho_w^* \left(1 - \frac{\rho_b}{\rho_b^*}\right), \tag{19}$$

where ρ_w* and ρ_b* are the material density of water and bentonite, respectively. Here, the value ρ_w*=1.00 g/cm^3, and the commonly used 'grain density' value of bentonite ρ_b*=2.75 g/cm^3 (Table 2) were used. Similar examples of main results for all the samples can be found in section D in the supplementary material.

While samples 5B and 6A differed only by their initial water content, a few qualitative differences can be observed. Firstly, as was already shown in Table 4 and discussed above about wall friction, sample 5B (Fig. 8) had a marked density gradient in the initial state, whereas sample 6A (Fig. 9) had a very flat initial density profile. Another difference between the two samples can be seen in the late stage of swelling behavior in the top part of the samples. While sample 5B (Fig. 8) remained locally rather homogeneous throughout the experiment, clear inhomogeneities occured in the final state of sample 6A (Fig. 9). Comparing the measured water content curve and the validation data with the saturation limit shows that the top end of sample 6A was unsaturated in the final state. This indicates that the observed inhomogeneities were likely voids created by gas accumulation. The gas may have originated from compressed pore air trapped during the compaction and from residual air dissolved in the water. Such visible inhomogeneities were observed in the most dilute upper parts of some of the samples in the final state (Table 4). However, the appearance of the voids does not seem to correlate with the initial dry density and water content values. In general, the overall swelling behavior was qualitatively similar and systematic between all the samples. The wetting and swelling were very fast in the beginning, but slowed down considerably over time (see deformation plots in Fig. 7 and in section C in the supplementary material). The bentonite in the upper part became fully saturated, which effectively suppressed water transport deeper into the sample due to low permeability in the saturated zone. In the final state, the upper part of the sample was saturated (apart from the gas filled

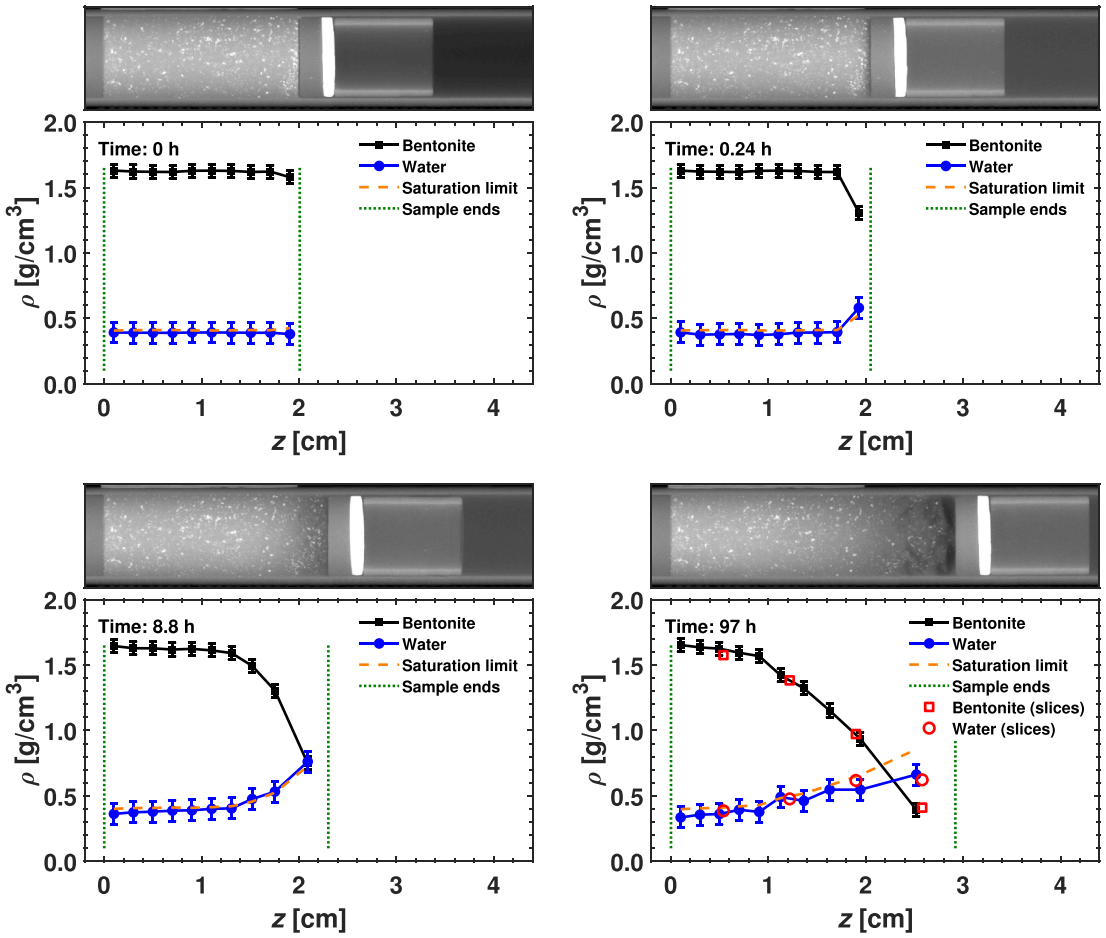

Fig. 9. Example of main results for sample 6A ($\rho_{b0} \approx 1.65\,g/cm^3$, $w_0 \approx 24\%$). The measured partial density profiles of bentonite and water, the saturation limit, and the corresponding aluminum equivalent thickness images are shown at four instants of time. Also shown are the validation data in the last subfigure.

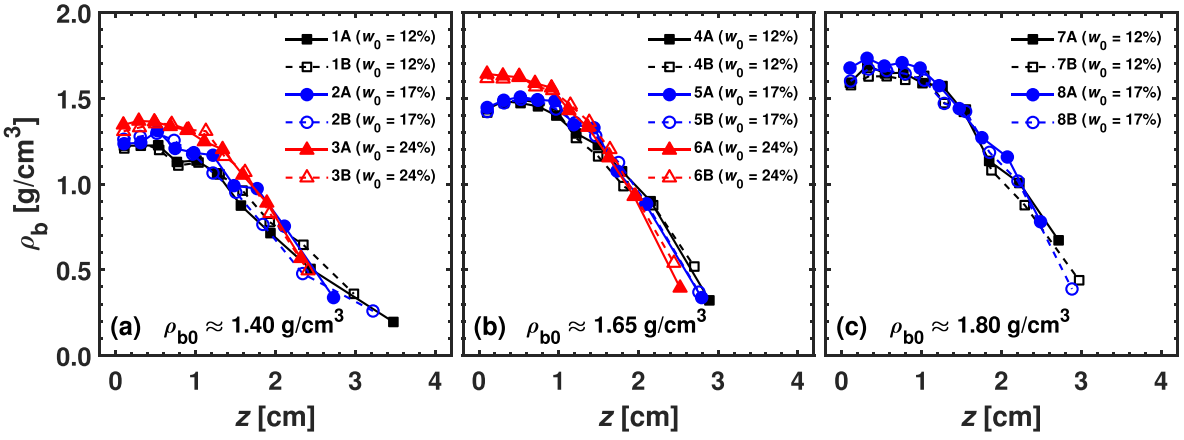

Fig. 10. Dry density profiles for low (a), middle (b) and high (c) density samples in final state.

voids), while the lower part remained unsaturated (if not initially saturated). Obviously, the duration of the experiments covered only the initial stage of the swelling process to maximum dilution, and hence no stationary state was reached during four days of wetting. The local deformation of material was large and initially rapid, and despite the optimized deformation analysis, small errors in the measured displacements occurred. These errors were caused, e.g., by deviations from the one-dimensional swelling behavior, by non-uniform distribution of tracer particles, by low concentration of tracer particles in the most swollen regions and by occasional spurious behavior of tracer particles near the tube wall and at the seams of the stitched images. These errors led to increasing scatter of the partial density profiles of bentonite and water. Ideally, the errors in the partial densities are related as $\Delta\rho_w = -c_b'/c_w' \cdot \Delta\rho_b \approx -2.2 \cdot \Delta\rho_b$ (derived from Eq. 13, assuming $\Delta\mu_s'=0$). This explains why the partial density profiles of water are generally more noisy than those of bentonite, and why the erroneous data points seem to

Table 5
Details and results of some one-dimensional bentonite swelling experiments from literature. Columns: ρ_{b0} = initial dry density, w_0 = initial water content, d = sample diameter, h_0 = initial sample height, PD = porous disc on top (Yes/No), $c(Na^+)$ = sodium concentration in water, $c(Ca^{2+})$ = calsium concentration in water, u_t = top end displacement after 4 days of swelling (approximated from graphs). Notes: CB = Commercial Na-bentonite.

Bentonite	ρ_{b0} [g/cm^3]	w_0 [%]	d [cm]	h_0 [cm]	PD	$c(Na^+)$ [M]	$c(Ca^{2+})$ [M]	u_t [cm]	Reference
MX-80	1.74	17	5.0	4.0	Yes	0.000	0.000	1.5	Sane et al. (2013)
MX-80	1.74	17	5.0	4.0	Yes	0.111	0.032	2.0	Sane et al. (2013)
MX-80	1.75	17	5.0	4.0	No?	0.000	0.000	2.7	Navarro et al. (2017)
MX-80	1.75	17	5.0	4.0	No?	0.111	0.032	2.8	Navarro et al. (2017)
CB	1.20	30	3.7	1.0	No	0.000	0.000	1.8	Li et al. (2019)
CB	1.20	30	3.7	1.0	No	0.100	0.000	1.6	Li et al. (2019)

be in the opposite directions (minus sign). Nevertheless, the results obtained agree reasonably well with the validation data.

5.3. Final state dry density profiles and total swelling

Fig. 10 shows the measured dry density profiles in the final state for all the samples. The general shape of the curves is similar despite the different initial dry density and water content values. The dry density profiles between the repeated experiments (A vs B) are very similar but differ near the top of the samples, where the largest contribution to the total swelling comes. The top end displacements (u_t) indeed show large variations both between different cases and between repeated experiments (Table 4). It seems that the samples with visible voids swelled more than those remaining locally homogeneous. Due to the scattered values, it is difficult to see correlation between the initial values and the top end displacements.

Similar one-dimensional bentonite swelling experiments have been performed, e.g., by Sane et al. (2013), Navarro et al. (2017) and Li et al. (2019). In those studies, the total swelling of compacted bentonite samples was visually monitored through transparent sample tubes. Table 5 shows details and results of some relevant experiments of their studies to compare here. In general, the top end displacements in their experiments were somewhat greater than here. This was probably due to smaller effect of wall friction as the sample diameter was larger and the samples were not directly compacted into the tubes (smaller initial normal stress against tube wall) in their experiments. The total swelling may also depend on the mass of a porous disc placed on the top of the sample as the balancing axial swelling stress of the dilute top part may be very small and sensitive to small changes. Sane et al. (2013) used porous stainless steel discs, whereas Li et al. (2019), and possibly also Navarro et al. (2017), did not use discs.

6. Conclusions

A method based on X-ray imaging for monitoring one-dimensional wetting and swelling of bentonite in a narrow tube was introduced. The method yields the deformation and the partial density distributions of bentonite and water as a function of time. The deformation of the samples was measured using tracer particles and a specific image correlation technique. The measurement of the partial densities of bentonite and water was based on careful calibration utilizing the measured effective X-ray attenuation coefficient. The developed local beam hardening correction was found to be essential for quantitative density analysis based on X-ray images.

An obvious technical drawback of the method is the limited accuracy of the displacement analysis, at least as applied in the present case where rapid and large deformations occurred. Furthermore, the measured partial densities of bentonite and water appeared to be quite sensitive to errors made in displacement analysis which in some cases led to marked scatter in the measured density profiles. In spite of that, the results obtained here are consistent and agree, in general, relatively well with the validation data obtained gravimetrically from the the samples in the final state of the experiment.

Most of the samples showed an initial density gradient caused by wall friction during sample compaction. The effect of wall friction during the compaction was pronounced here due to the high aspect ratio of the samples ($h/d = 2$). Wall friction was also likely present in the experiments and restricted the swelling process to some extend. In some of the experiments spurious inhomogeneities, most likely caused by accumulation of air to form voids, were observed especially in the upper parts of the sample at late stage of the experiment. Although such phenomena do not compromise the applicability of the present experimental method as such, they may hamper the use and interpretation of the data, e.g., in model validation purposes. Due to wall friction and void formation, the results may reflect more real conditions, swelling and wetting of bentonite in a narrow fracture, than ideal free swelling conditions. To fully utilize the results obtained, one may need a more sophisticated material model that takes into account these non-idealities.

The method proved to be useful for monitoring wetting and swelling of bentonite in the experimental setup in this study. It yielded potentially valuable data on hydro-mechanical properties of bentonite, which can be used to develop and validate material and transport models regarding the behavior of bentonite buffer. Compared to traditional methods, where total swelling is only measured, the X-ray imaging method can be used to produce much more detailed data on wetting and swelling behavior of bentonite to support modeling even better.

Finally, the method introduced here might be even more applicable in cases with more moderate rate and degree of deformation, such as wetting and swelling of bentonite in a confined volume. The method developed here is not restricted only to the materials used in this study, but may be applied for non-destructive monitoring of simultaneous liquid transport and related deformation with a variety of materials that allow X-ray imaging and contain natural or artificially added heterogeneities which are visible in X-ray images and can be used to measure the deformation. Furthermore, the local beam hardening correction can be applied more generally to facilitate more accurate image analysis and image-based measuring techniques in X-ray imaging and tomography.

CRediT authorship contribution statement

Tero Harjupatana: Methodology, Software, Formal analysis, Investigation, Writing – original draft, Visualization. **Arttu Miettinen:** Writing – review & editing. **Markku Kataja:** Conceptualization, Methodology, Software, Formal analysis, Writing – review & editing, Supervision, Project administration, Funding acquisition.

Declaration of Competing Interest

The authors declare that they have no known competing financial interests or personal relationships that could have appeared to influence the work reported in this paper.

Acknowledgments

The research leading to these results has received funding from the European Atomic Energy Community's 7th Framework Programme (FP7/2007-2011) under grant agreement no. 295487.

Appendix A. Supplementary data

Supplementary data to this article can be found online at https://doi.org/10.1016/j.clay.2022.106485.

References

Börjesson, L., Gunnarsson, D., Johannesson, L.-E., Jonsson, E., 2010. Design, Production and Initial State of the Buffer. Technical Report. SKB.

Bushberg, J.T., Seibert, J.A., Leidholdt, E.M., Boone, J.M., 2002. The Essential Physics of Medical Imaging, 2 edition. Lippincott Williams & Wilkins.

Gustschin, N., Gustschin, A., Epple, F., Allner, S., Achterhold, K., Herzen, J., Pfeiffer, F., 2019. Signal-to-thickness calibration and pixel-wise interpolation for beam-hardening artefact reduction in microCT. EPL (Europhysics Letters) 125 (3), 38003.

Harjupatana, T., Alaraudanjoki, J., Kataja, M., 2015. X-ray tomographic method for measuring three-dimensional deformation and water content distribution in swelling clays. Appl. Clay Sci. 114, 386–394.

Harjupatana, T., Miettinen, A., Kataja, M., 2021. Swelling of MX-80 bentonite in a narrow tube. Zenodo 2021. https://doi.org/10.5281/zenodo.5413932.

Hellä, P., Pitkänen, P., Löfman, J., Partamies, S., Vuorinen, U., Wersin, P., 2014. Safety Case for the Disposal of Spent Nuclear Fuel at Olkiluoto: Definition of Reference and Bounding Groundwaters, Buffer and Backfill Porewaters. Posiva. https://cris.vtt.fi/en/publications/safety-case-for-the-disposal-of-spent-nuclear-fuel-at-olkiluoto-d.

Herman, G.T., 1979. Correction for Beam Hardening in Computed Tomography. Phys. Med. Biol. 24 (1), 81–106.

Hsieh, J., Molthen, R.C., Dawson, C.A., Johnson, R.H., 2000. An iterative approach to the beam hardening correction in cone beam CT. Med. Phys. 27 (1), 23–29.

Hubbell, J.H., Seltzer, S.M., 1995. Tables of X-Ray Mass Attenuation Coefficients and Mass Energy-Absorption Coefficients 1 keV to 20 MeV for Elements Z = 1 to 92 and 48 Additional Substances of Dosimetric Interest. Technical Report. National Institute of Standards and Technology.

Johns, H.E., Cunningham, J.R., 1983. The Physics of Radiology, 4 edition. Charles C. Thomas.

Jung, S.Y., Lim, S., Lee, S.J., 2012. Investigation of water seepage through porous media using X-ray imaging technique. J. Hydrol. 452, 83–89.

Juvankoski, M., 2013. Buffer Design 2012. Technical Report, Posiva Oy.

Karnland, O., 2010. Chemical and Mineralogical Characterization of the Bentonite Buffer for the Acceptance Control Procedure in a KBS-3 Repository. Technical Report. Swedish Nuclear Fuel and Waste Management Co.

Karnland, O., Olsson, S., Nilsson, U., 2006. Mineralogy and Sealing Properties of Various Bentonites and Smectite-Rich Clay Materials. Technical Report. Swedish Nuclear Fuel and Waste Management Co.

Koch, D., 2002. Bentonites as a basic material for technical base liners and site encapsulation cut-off walls. Appl. Clay Sci. 21 (1–2), 1–11.

Li, X., Xu, Y., Li, C., 2019. Experimental study on the 1-d free swelling of compacted bentonite. Acta Geotech. 1–13.

Michrafy, A., Kadiri, M.S., Dodds, J.A., 2003. Wall friction and its effects on the density distribution in the compaction of pharmaceutical excipients. Chem. Eng. Res. Des. 81 (8), 946–952.

Miettinen, A., Harjupatana, T., Kataja, M., Fortino, S., Immonen, K., 2016. Time-Resolved X-Ray Microtomographic Measurement of Water Transport in Wood-Fibre Reinforced Composite Material. In: IOP Conference Series: Materials Science and Engineering, vol. 139. IOP Publishing, p. 012037.

Nagra, 2009. The Nagra Research, Development and Demonstration (RD&D) Plan for the Disposal of Radioactive Waste in Switzerland.

Navarro, V., Yustres, Á., Asensio, L., De la Morena, G., González-Arteaga, J., Laurila, T., Pintado, X., 2017. Modelling of compacted bentonite swelling accounting for salinity effects. Eng. Geol. 223, 48–58.

Neretnieks, I., Liu, L., Moreno, L., 2009. Mechanisms and Models for Bentonite erosion.

Reid, C., Lunn, R., El Mountassir, G., Tarantino, A., 2015. A mechanism for bentonite buffer erosion in a fracture with a naturally varying aperture. Mineral. Mag. 79 (6), 1485–1494.

Sane, P., Laurila, T., Olin, M., Koskinen, K., 2013. Current Status of Mechanical erosion Studies of Bentonite Buffer. Technical Report, Posiva Oy.

Shafizadeh, A., Gimmi, T., Van Loon, L., Kaestner, A., Lehmann, E., Maeder, U.K., Churakov, S.V., 2015. Quantification of water content across a cement-clay interface using high resolution neutron radiography. Phys. Procedia 69, 516–523.

Terskikh, V.V., Feurtado, J.A., Ren, C., Abrams, S.R., Kermode, A.R., 2005. Water uptake and oil distribution during imbibition of seeds of western white pine (Pinus monticola Dougl. Ex D. Don) monitored in vivo using magnetic resonance imaging. Planta 221 (1), 17–27.

Tien, Y.-M., Wu, P.-L., Huang, W.-H., Kuo, M.-F., Chu, C.-A., 2007. Wall friction measurement and compaction characteristics of bentonite powders. Powder Technol. 173 (2), 140–151.

Zhou, X., Zhou, J., Kinzelbach, W., Stauffer, F., 2014. Simultaneous measurement of unfrozen water content and ice content in frozen soil using gamma ray attenuation and TDR. Water Resour. Res. 50 (12), 9630–9655.

Zhou, R., Zhou, X., Li, X., Cai, Y., Liu, F., 2016. Study of the Microfocus X-ray Tube based on a Point-like Target used for Micro-Computed tomography. PLoS One 11 (6), e0156224.

Zou, W., Hunter, N., Swain, M.V., 2011. Application of Polychromatic CT for Mineral Density Determination. J. Dent. Res. 90 (1), 18–30.

Supplementary material for the article *"A method for measuring wetting and swelling of bentonite using X-ray imaging"*

Tero Harjupatana*,[a], Arttu Miettinen[a], and Markku Kataja[a]

[a]Department of Physics, University of Jyväskylä, P.O. Box 35 (YFL), FI-40014, Finland

February 9, 2022

A Supplementary figures

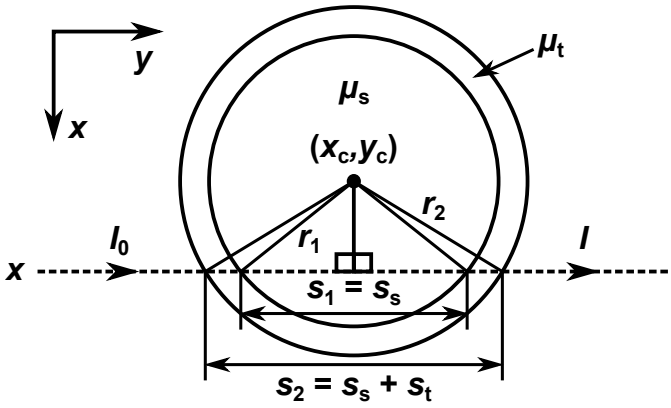

Figure A.1: Schematic cross-sectional view of tube and sample showing parallel beam geometry used to calculate travel distances through sample (s_s) and tube wall (s_t).

B Sedimentation test for tracer particles

The purpose of the sedimentation test was to determine the maximum water content of a bentonite suspension that can support the weight of tracer particles. If the water content in bentonite samples becomes too high, the tracer particles start to sink leading to failure of the deformation measurement. Before introducing the sedimentation test in section B.2, another technique for

*Corresponding author.
E-mail: tero.t.harjupatana@jyu.fi

correcting the X-ray images for blurring effects caused by the tracer particles is introduced in section B.1. Although this technique was not necessary for the main experiments in this work, it may be useful in cases where low partial densities of bentonite (or other solid materials) diluted in water must be measured, which was the case in the sedimentation test.

B.1 Image deblurring

Blurring in X-ray images can be caused by many different mechanisms such as finite size of the focal spot, X-ray and light scattering and by charge spreading in the detector array (Zscherpel et al., 2004). Blurring causes an unwanted correlation between grayscale values in X-ray images as the grayscale value of a pixel becomes dependent on its neighborhood values. The standard way to describe the image blurring process is through the equation

$$I_b = I \circledast \mathrm{PSF}, \tag{B.1}$$

where I is the virtual unblurred image, I_b is the detected blurred image, PSF is the point spread function and $\circledast$ denotes linear convolution (Gonzalez and Woods, 2002). In general, direct inversion of Eq. B.1 highly amplifies noise, whereby special deconvolution techniques are needed. One of those techniques is the Wiener filtering, which yields an estimate for the unblurred image in a form

$$\hat{I} = \mathcal{F}^{-1}\left\{\frac{\overline{\mathcal{F}\{\mathrm{PSF}\}}\mathcal{F}\{I_b\}}{\overline{\mathcal{F}\{\mathrm{PSF}\}}\mathcal{F}\{\mathrm{PSF}\} + \epsilon}\right\}, \tag{B.2}$$

where $\mathcal{F}$ and $\mathcal{F}^{-1}$ are the forward and inverse Fourier transforms, the overbars denote the complex conjugates and $\epsilon = 1/\mathrm{SNR}$. The frequency dependent signal-to-noise ratio (SNR) is not usually known, and therefore ϵ can be regarded as a small positive parameter to be tuned.

A practical way to measure the PSF is indirectly through the edge and line spread functions (ESF and LSF). These three functions are related by the equations (Smith, 1997)

$$\frac{d}{dx'}\mathrm{ESF}(x') = \mathrm{LSF}(x') = \int \mathrm{PSF}(x', y')dy', \tag{B.3}$$

where the axes of a rotated coordinate system (counterclockwise rotation through an angle θ) are x' and y'. These axes are perpendicular and parallel with respect to the ideal edge

$$\mathrm{EDGE}(x', y') = \begin{cases} 0, & \text{for } x' < 0 \\ 1, & \text{for } x' \geq 0 \end{cases}, \tag{B.4}$$

which gets blurred as

$$\mathrm{ESF} = \mathrm{EDGE} \circledast \mathrm{PSF}. \tag{B.5}$$

The ESF measurement was carried out by taking X-ray images of the straight edge of a 6 mm thick lead plate oriented at three different angles (0°, 90° and 180°). The ESF values were found by measuring the average transmittance profiles across the edge, and were found to be similar for the three orientations. The PSF was thus assumed to be rotationally symmetric and the average of the three results for ESF was used (Fig. B.1a). The LSF was obtained by differentiating the averaged ESF according to Eq. B.3 (Fig. B.1b). A sum of Gaussian functions

$$f(x) = \sum_{i=1}^{n} A_i \exp[-x^2/(2\sigma_i^2)] \tag{B.6}$$

was fitted to the LSF data by using a non-linear least squares solver with initial guesses of $A_i = \mathrm{LSF}(0)/n$ and $\sigma_i = 10^{2.7i/n}$, and with a bound of $A_i > 0$. The sum of squared residuals formed an L-shaped curve as a function of n, where the flat minimum started approximately at $n = 6$, which was thereby chosen as the number of terms used in the fit function (Eq. B.6). Using the Gaussian fit function was preferred as it smooths noisy data and allows to calculate the PSF analytically through the inverse Abel transform as

$$\mathrm{PSF}(r) = -\frac{1}{\pi}\int_r^\infty \frac{df}{dx}\frac{dx}{\sqrt{x^2 - r^2}} = \sum_{i=1}^{n} \frac{A_i}{\sigma_i\sqrt{2\pi}} \exp[-r^2/(2\sigma_i^2)]. \tag{B.7}$$

The central part of the reconstructed PSF is shown in Fig. B.1c. All the X-ray images taken in the sedimentation test were deblurred using the measured PSF and Eq. B.2 with $\epsilon = 0.05$.

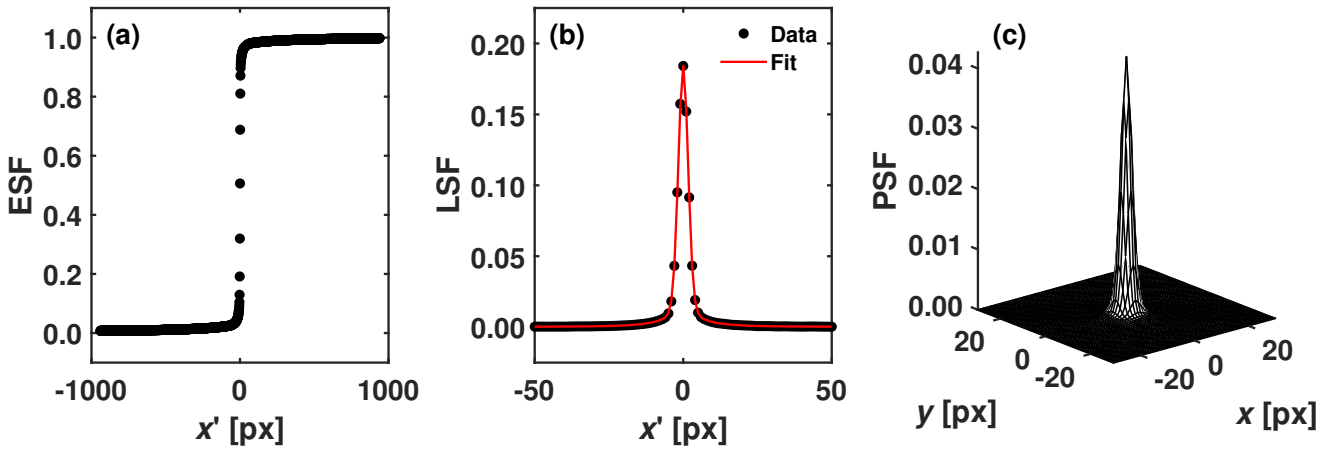

Figure B.1: Spread functions used in image deblurring. The edge spread function (a) was measured and used to calculate the line spread function (b), to which the sum of Gaussian functions was fitted and used to reconstruct the rotationally symmetric point spread function (c).

B.2 Sedimentation test and analysis

A suspension with a target average water content of $w = 20$ was made by mixing MX-80 bentonite in saline solution (0.1 M NaCl). A sample tube was filled with the suspension and let to settle for 19 hours to allow a vertical bentonite concentration profile to be developed in the tube. A small amount of tracer particles was then dropped into the tube. The suspension was X-ray imaged four times: just before adding the tracer particles, and 0.5 h, 5 h and 4 d after adding the tracer particles. In addition, X-ray images of the empty and saline solution filled sample tube were taken.

The vertical attenuation coefficient profile along the tube was measured and analyzed in a similar way to the swelling experiments in the main article. As the water content of the suspension was high (i.e., ρ_b was low), it was reasonable to assume that the suspension was fully saturated at all times such that $\rho_w = \rho_{w,\mathrm{sat}}$. This allows combining Eqs. 13 and 19 (main article) to solve the relative attenuation coefficient of the suspension in the form

$$\mu_s' = \mu_w' + C_b' \cdot \rho_b\,; \quad \text{where } C_b' = \left(c_b' - c_w' \cdot \frac{\rho_w^*}{\rho_b^*}\right). \tag{B.8}$$

The relative attenuation coefficient of water μ'_w was found from the image of the sample tube filled with saline solution. The coefficient C'_b was calculated from the equation

$$m_b = \int \rho_b dV = \frac{A}{C'_b} \int [\mu'_s(z) - \mu'_w]\, dz, \tag{B.9}$$

where m_b is the known total mass of bentonite in the tube and A is the cross-sectional area of the tube. The partial densities of bentonite and water were found using Eqs. B.8 and 19 (main article), respectively. The aluminum equivalent thickness image and the partial density profiles of bentonite and water after 5 hours of settling are shown in Fig. B.2. The measured density profiles were used to estimate the critical water content of the suspension in the vertical range of the tracer particles, i.e., the value above which the tracer particles can effectively sediment, and below which they are stopped at least considering the time scale of the present experiments ($\sim$ 100 h). According to the results given in Table B.1, the critical water content is approximately 20. The highest average water content values in the topmost layer ranged from 1.0 to 3.3 between the samples in the swelling experiments. It thus appears justified to assume that the tracer particles can indeed follow the motion of bentonite throughout the experiment. In principle, water content may still approach the critical value in a very narrow layer next to the top surface. As the displacement of the top surface was found based on observing the position of the filter disc and not of the tracer particles, even that condition is not likely to cause marked error in the results.

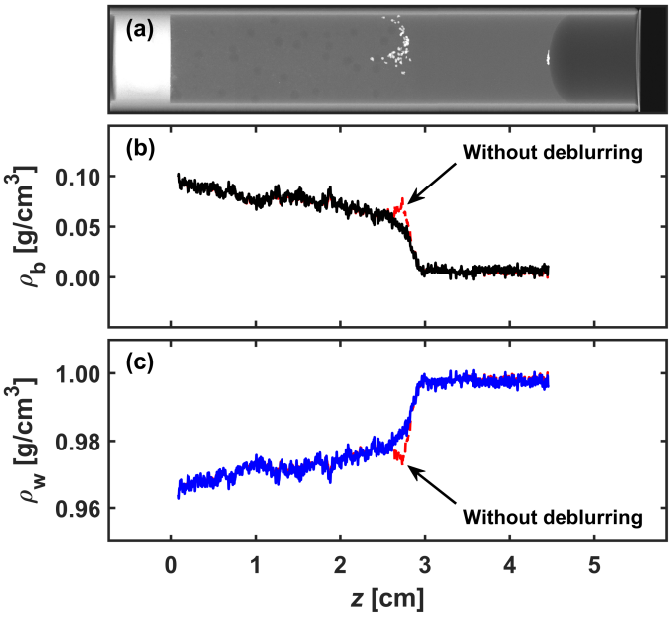

Figure B.2: Results from sedimentation test after 5 hours of settling. The tracer particles can be seen in the middle of the aluminum equivalent thickness image (a) (and a few of them trapped in the liquid surface film). The water content at the height of the particles was calculated from the measured bentonite (b) and water density profiles (c). The dashed red curves are the partial densities without deblurring applied.

Table B.1: Mean and standard deviation of critical water content after three different settling times.

Settling time	Water content
0.5 h	21.9 ± 5.3
5 h	20.0 ± 3.1
4 d	19.2 ± 2.5

Acknowledgments

The research leading to these results has received funding from the European Atomic Energy Community's 7th Framework Programme (FP7/2007-2011) under grant agreement no. 295487.

References

Gonzalez, R. C. and Woods, R. E. (2002). *Digital Image Processing*. Prentice Hall, 2 edition.

Smith, S. W. (1997). *The Scientist and Engineer's Guide to Digital Signal Processing*. California Technical Pub.

Zscherpel, U., Osterloh, K., and Ewert, U. (2004). Unsharpness characteristics of digital detectors for industrial radiographic imaging. *Journal of Nondestructive Testing*, 9(5):1–8.